Abstract

A novel Liquid Air Transpired Solar Collector (LATSC) has been proposed in this thesis for which a numerical model is developed followed by empirical testing. Sensitivity analysis has been performed on the numerical model of the LATSC for varying air thermal capacitance rate, water thermal capacitance rate, plate emissivity, wind speed, solar radiation, inlet water temperature and ambient air temperature. A numerical model of a falling film type liquid desiccant regenerator (LDR) has been developed and combined with the LATSC model to evaluate the performance of the combined system under varying air, water and desiccant flow rates. It was observed that as the total thermal capacitance rate of air and water is increased, a lower air thermal capacitance ratio is required for optimal performance. The combined LATSC and LDR model has also been optimized for typical Abu Dhabi conditions. The optimized thermal capacitance rate of air and water were found to be 10.98 W/m^2-K and 38.65 W/m^2-K respectively while the optimal desiccant mass flow rate per unit of regenerator and collector area was found to be 0.00016645 kg/s-m^2.

This research was supported by the Government of Abu Dhabi to help fulfill the vision of the late President Sheikh Zayed Bin Sultan Al Nayhan for sustainable development and empowerment of the UAE and humankind.

Acknowledgments

My first and foremost expression of gratitude is towards Allah (SWT) the all mighty who is the source of all the strength and intellect that I have put in to this project. Verily without his benevolence this project would have not been possible to complete.

Secondly I would like to thank my well wishers who have prayed for me so that I could have the strength to excel in my studies. In this, a special thanks goes to my parents who have worked hard to facilitate quality education for me throughout my life.

I would also like to thank the members of my Research Supervisory Committee for their suggestions on how to improve the quality of my research. Additionally I would like to thank Mr. John Owen from SoleUAE for providing the flat plate collector used at a very low price. Lastly, and very importantly, I thank Dr Peter Armstrong for being the one stop destination for advice on all aspects of my research. His prompt and relevant advice on issues related to the experimental setup and instrumentation have ensured that I finish my thesis on time.

Abdul Qadir,

Masdar Institute, June 25 2011

Contents

Contents

List of Tables

List of Figures

CHAPTER 1

1 Introduction

Solar water heating collectors have been used for domestic water heating for decades as they provide considerable savings in energy bills. Conventional flat-plate water heating collectors can provide high solar to thermal energy conversion efficiency and can fulfill most of the water heating demands of a building when storage of about one day's water use is provided. However the capital cost of installing water heating collectors remains an obstacle in its widespread use. These costs are associated with the absorber plate material, glazing, installation, piping and transportation of the collector. Numerous studies in the recent past have been carried out to develop low cost collectors (Burch, Christensen, Merrigan, Hewett, & Jorgensen, 2005; Burch, Salasovich, & Hillman, 2005; Koehl, 2001). These studies explore the possibility of using polymeric material absorber plates instead of the costly copper plates used in conventional collectors. Studies have also looked in to the use of unglazed collectors to reduce the weight and cost of the collector. A major obstacle faced in the use of polymer absorber plates in glazed collectors is the serious degradation of the plate at stagnation temperatures. Stagnation temperatures are reached when the pumping of water is stopped and the water is left stagnant in the collector while still irradiated by the sun.

Unglazed transpired collectors are a low-cost alternative to glazed air heating collectors. The capital cost of installing transpired collectors is almost a third of that of flat plate collectors per unit area (Pesaran & Wipke, 1992). Transpired collectors actively pull air through small perforations in the absorber plate which leads to the heating of the air. The air movement suppresses convection losses as the heat conducted to the thermal boundary layer is continuously pulled back toward the plate. A transpired solar collector can perform very efficiently at high suction velocities. However for lower suction velocities, required to achieve high air temperature desired for desiccant regeneration applications, the collector efficiency drops considerably. Thus although the collector is cheap, the efficiency penalty associated with lower suction velocities may make it a less attractive option for use in desiccant regeneration. Moreover for effective desiccant regeneration, hot water is preferred. This is due to the higher conductivity of water leading to faster heat transfer between water and the desiccant and to the mass flux boundary layer that is superimposed on the air side thermal boundary layer, than in the air desiccant scenario.

This thesis explores the possibility of combining the cost and convection suppression advantages of the transpired solar collector and the effective water heating characteristics of a flat plate collector into one collector. This will allow for the building of a low cost, unglazed collector which could potentially operate at high efficiencies where the performance of the collector under light wind would be as good if not better than that of a single glazed flat plate collector. The unglazed configuration also avoids stagnation problems as natural convection or forced convection through wind could ensure that the collector does not heat up to temperatures as high as 90-100^{o}C. The collector could then be made with low cost polymers or metal-polymer composites. The unglazed collector also offers the possibility of scaling the collector easily since the usual constraint in glazed collectors is the relatively difficult scalability of the glazing.

We will refer to the hybrid collector described above as the Liquid-Air Transpired Solar Collector (LATSC) from here on.

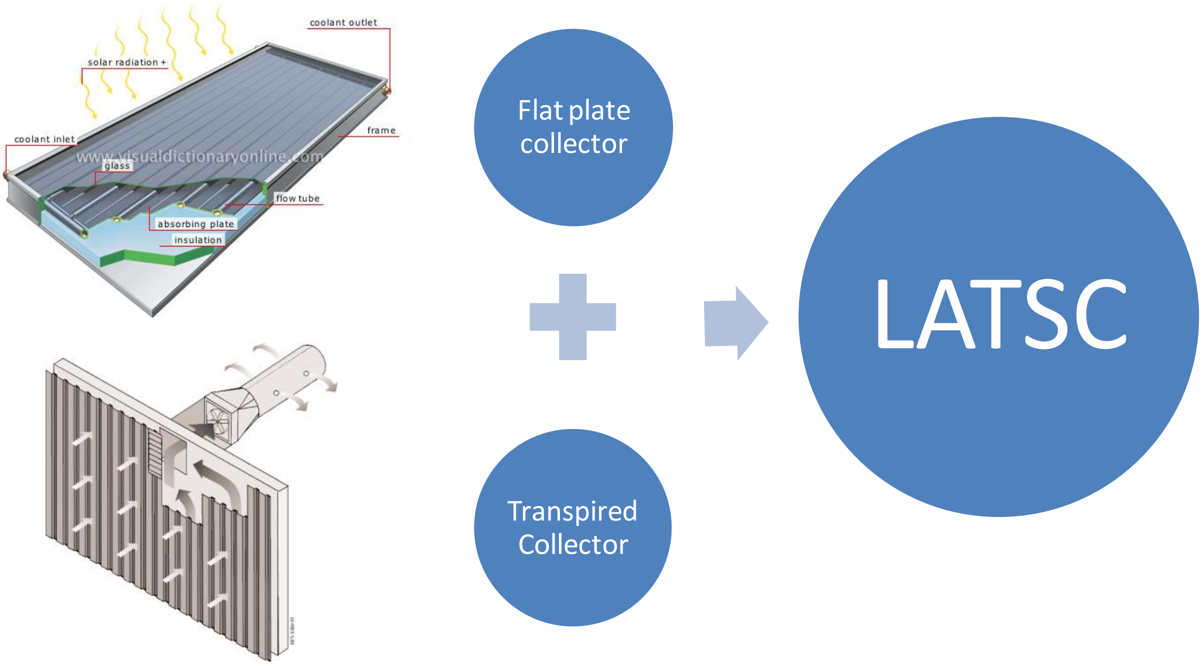

Figure 1.1: Concept of the Liquid-Air Transpired Solar Collector (illustrations on left from ("The Basics of Solar Energy Installations," 2010; Christensen, 1998)

The potential applications that have been kept in mind while developing the collector are liquid desiccant regeneration, low temperature desalination and domestic water heating. All three applications have large potential impact to reduce fossil fuel dependence in the energy mix of Abu Dhabi. Moreover liquid desiccant regeneration (LDR) and humidification-dehumidification (HDH) desalination both require hot water and air and thus can utilize all of the energy provided by the collector. Over

60% of peak electricity usage in Abu Dhabi city is attributed to cooling (M. T. Ali, Mokhtar, Armstrong, & Cheisa, 2011) which could be greatly reduced by the incorporation of liquid desiccant cooling powered through solar thermal energy. Furthermore the cost of solar collectors has been identified as the biggest hurdle in the commercial viability of solar cooling in general (Mokhtar et al., 2010) and of liquid desiccant air conditioning in particular (Dieckmann, Roth, & Brodrick, 2008). A schematic diagram of a liquid desiccant cooling system is shown in Figure 1.2. Figure 1.3 shows the schematic of a HDH desalination system.

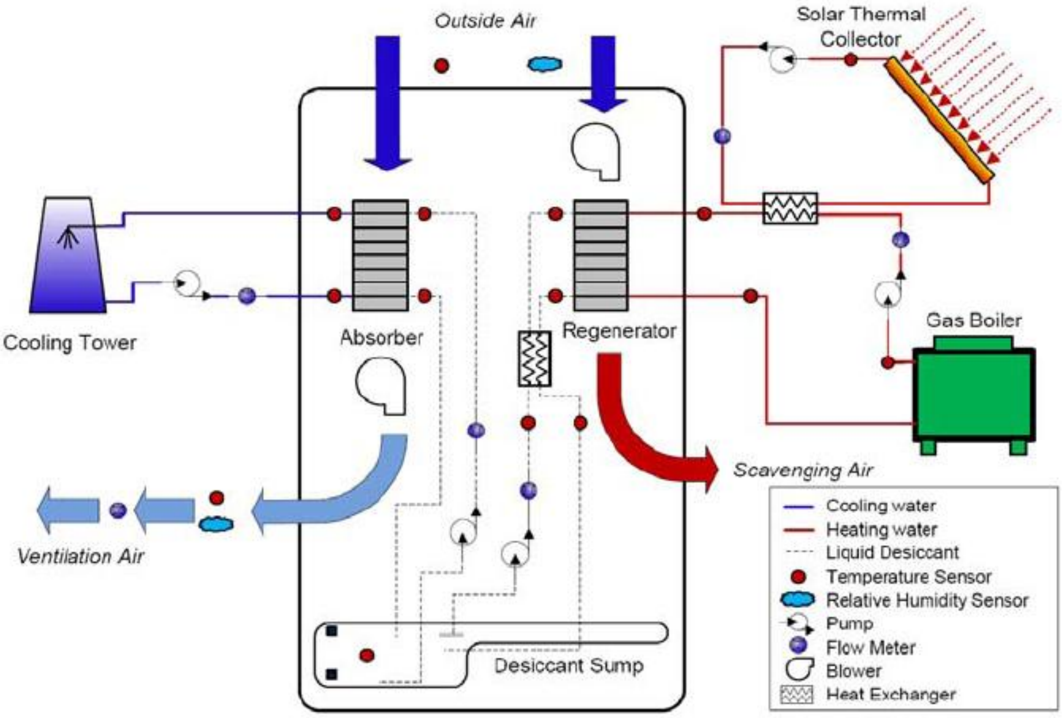

Figure 1.2: Liquid Desiccant Air Conditioning System(Jones & Harrison, 2008)

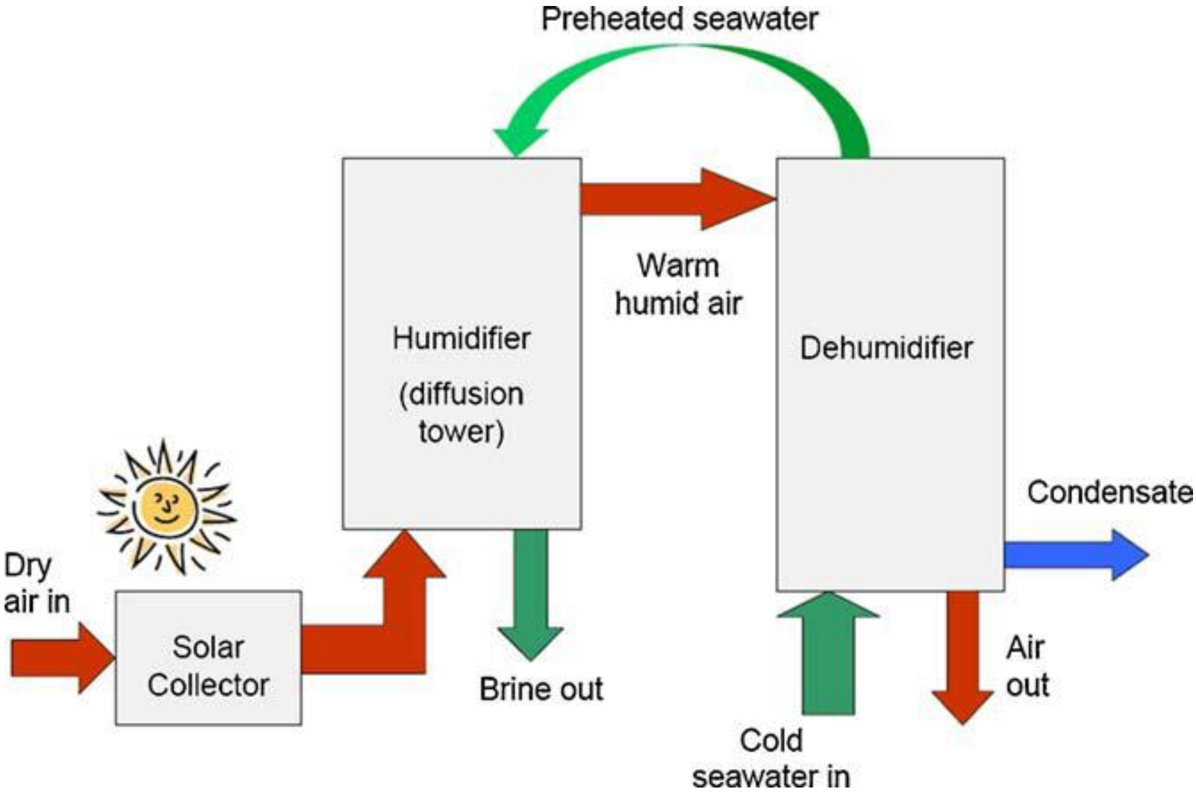

Figure 1.3: Humidification Dehumidification Desalination(Narayan et al., 2010)

1.1 Thesis Objectives

From the motivations described above, the objectives of the thesis follow logically as:

- Develop through first principles, a mathematical/numerical model of the LATSC
- Experimentally validate the LATSC model
- Build a numerical model of a liquid desiccant regenerator(LDR) and couple the model with the LATSC
- Determine optimum air flow rate, mass flow rate and desiccant flow rate to regenerate the desiccant for typical conditions in Abu Dhabi.

CHAPTER 2

2 Literature Review

The literature review is rich in many aspects related to unglazed transpired solar collectors (UTSC), flat plate collectors (FPC), liquid desiccant regeneration (LDR) systems and humidification dehumidification (HDH) desalination systems. The aspects discussed for the UTSC include heat transfer properties of the perforated plate, current uses of transpired solar collectors and documented useful modifications of transpired solar collectors in order to improve efficiency. The liquid desiccant regeneration section covers the review of different types of desiccants, advantages of using liquid desiccants for cooling and dehumidification and heat mass transfer models used in modeling liquid desiccant regeneration systems. The HDH desalination part highlights the need for both hot water and air sources as thermal energy inputs and explains the use and advantages of the HDH cycles and the parameters which impact their performance.

2.1 Flat plate collectors

The flat plate collector is a well-developed technology and there has been extensive research on the performance of the FPC with no glazing, single glazing and double glazing. Amongst the earliest of works are Hottel and Whillier (1955) and Hottel and Woertz (1942) who describe in detail the optics of the collector and develop curves for the ‘utilizability’ of the collector which aids in comparing the performance of collectors at different locations. They also develop the collector efficiency factor and the heat removal factor, for the flat plate collector, which are now in common use. Bliss (1960) develops several collector performance curves based on the collector efficiency and heat removal factor.

Hottel and Woertz (1942) and Klein (1975) have developed a top loss model for the flat plate collector taking in to account the radiation and convection losses for single, double and triple glazing collectors.

Duffie and Beckman (1980) describe in detail the heat transfer mechanisms for flat plate collectors of the fin tube type. They elegantly combine the work from Bliss(1960)(1960), Hottel and Whillier(1955)(1955) and Klien (1975) and provide the model of a flat plate collector from the very basic concepts such as energy balance and heat transfer models to advanced collector efficiency and incidence angle modifier models.

2.2 Unglazed Transpired Solar Collector

There are a number of analytical, numerical and experimental studies performed on the performance of UTSC. A mathematical model was developed by Leon and Kumar (2007) which analyzed the efficiency of a UTSC for varying plate absorptivity, emissivity, hole pitch, diameter and solar radiation. They reported that a small pitch to diameter ratio leads to a higher air temperature rise while solar absorptivity, perforation pitch and approach velocity have the strongest effect on collector heat exchange effectiveness and efficiency.

2.2.1 Numerical codes

Kutscher (1992), Kutscher (1994) and Kutscher, Christensen and Barker (1993) discuss in great detail the heat transfer for low speed air flow through low porosity perforated plates, used in UTSCs, with and without crosswind. Kutscher (1992) simulates the conditions with different plate porosities, Reynolds numbers and wind speeds using the FLUENT code. In order to visualize the heat transfer taking place at the surface of the plate, color infrared thermography is used.

Building upon Kutscher’s (1992) work, Gawlik (1995) and Gawlik and Kutscher (2002) studied the heat transfer effects in the use of low conductivity materials and corrugated sheets to make the UTSCs utilizing CFD to simulate his model. He found that UTSCs made from low conductivity materials performed similarly to those made from high conductivity materials and were subject to very low IR losses. Thus he concluded that low cost low conductivity materials such as galvanized steel or plastic may be used to make UTSCs. Gawlik also derived convective heat loss correlations for corrugated plates and concluded that under moderate wind speeds and low suction velocities, corrugated plates have much higher wind losses than flat plates.

Gunnewiek, Brundrett and Hollands (1996) analyzed the flow characteristics of the UTSC by using a 2-D code under no wind conditions. They discussed the importance of heat transfer from the back of the plate and the effects of polarity of the profile on the efficiency of the plate. They concluded that buoyancy is the major cause of flow maldistribution and to increase the efficiency of the UTC under buoyancy dominated flow, the average suction velocity should be small, the plenum relatively wide, and the plate’s hydraulic resistance relatively low.

Dymond and Kutscher (1997) have developed a computer model for an unglazed transpired solar collector which allows the user to design a model and test its flow distribution characteristics using different parameters. Moreover the pipe network method is used with minor modifications and used to predict the flow uniformity and efficiency of the model. This type of modeling has been used to design the SolarWall®.

Arulanandam, Hollands, and Brundrett (1999) uses a CFD model to analyze the heat transfer in UTSC under no wind conditions. They concluded that acceptable efficiencies could achieved with a transpired plate absorber made from materials of low conductivity such as plastics.

Summers (1995) has developed a code in the Transient System Simulation (TRNSYS) program for simulating a transpired solar collector on the south facing wall of a building which allows for the calculation of the energy savings due to solar energy gains, reduction in wall losses and the recapturing of heat escaping from the walls. He concludes that UTC's are only competitive when replacing electric water heaters and replacing of oil or natural gas fired heaters is economically unfeasible.

Maurer's (2004) work is a continuation of Summers' work in which she develops a TRNSYS code for the analysis of a transpired collector mounted on a building wall. She highlighted an error in the equation for acceleration pressure drop in Summer's work as well as discrepancies in the equations for heat conduction through the south wall.

2.2.2 Experimental

Kutscher (1992) performed three types of heat transfer experiments, namely transient temperature, energy source measurement and direct delta T measurement, to test low porosity perforated plates. It was found that the delta T measurement was most accurate for direct measurement while a combination of delta T and energy source measurement was used to determine wind losses. Based on experimental results, he derived a correlation for the heat exchange effectiveness of low porosity plates based on the suction velocity V_s, wind speed, V_w, hole diameter, D_h, and pitch of the holes.

Van-Decker, Hollands and Brunger (2001) assessed the heat exchange relations of a UTSC consisting of circular holes on a square or triangular pitch. They found that at a typical ventilation suction velocity of 0.05m/s and wind speed up to 5m/s, long wave radiative heat transfer from the plate remains as the dominating heat loss mechanism. Moreover by taking suction velocities of 0.03-0.08 m/s, efficiencies of 50%-80% have been achieved. They conclude that the effectiveness ε_{hx} decreases with increasing suction velocity V_s, hole diameter D_h, and pitch of the holes. However it increases with increasing wind speed U_w and thickness of the plate due to a larger surface area in the hole and thus greater heat transfer in the hole. Furthermore, under typical operating conditions, 62% of the ultimate temperature rise is expected to occur at the front surface, 28% in the hole and 10% at the back surface of the plate.

2.2.3 Current uses

Norton (2006) outlines the two major uses of UTSC as air heating for paint shops in USA and Canada and crop drying applications mostly in Malaysia and Indonesia. Leon and Kumar (2007) mention that most applications for UTSC have been in Europe and North America for heating ventilation air and very little information is available for its application in tropical countries. Thus the model they developed is especially for tropical climates.

A publication from the European Solar Thermal Industry Federation (*Key Issues for Renewable Heat in Europe (K4RES-H)*, 2006)) has demonstrated the use of UTSC for a desiccant cooling system that provides air conditioning for a seminar room and cafeteria in Freiburg, Germany. 100 m^2 of UTSC are used as the only heat source and the desiccant used for this system is silica gel. There is no backup or storage system in this application.

2.2.4 Useful Modifications

Belusko, Saman, and Bruno (2008) have researched the possibility of jet impingement from the back plate in an UTSC and have recorded a 21% increase in the thermal efficiency of the collector. Moreover, there were pressure losses incurred but were small compared to the gain in thermal efficiency. It was also found that increasing the hole spacing led to an increase in the thermal efficiency of the UTSC.

2.3 Liquid Desiccant Regeneration

2.3.1 Desiccants

Kabeel (2007)analyses the advantages of liquid descants over solid desiccants and mentions that liquid desiccants can be pumped around in an absorption/ regeneration cycle and thus several such units may be used to cool large buildings. Furthermore liquid desiccants have the advantage of being able to be stored so that they may be regenerated using cheap and renewable means such as solar thermal energy.

Kinsara, Elsayedt, and AI-Rabghi (1996) also lists some advantages of liquid desiccants over solid desiccants which includes ease of mobility and manipulation, low pressure drop of air flow across the desiccant material, ability to be used in filtration to remove dust and lower required regeneration temperature compared to solid desiccants.

Thoruwaa, Johnstoneb, Grantb, and Smith (2000) mentions that the silica gel and molecular sieves have a regeneration temperature of 150°C which is high compared to that of liquid desiccants such as lithium chloride, lithium bromide and calcium chloride. They have developed a solid calcium chloride/clay desiccant which can be regenerated at 50°C.

Xiong, Dai, and Wang (2009) have empirically investigated a hybrid liquid desiccant cycle using calcium chloride and lithium bromide. The motivation for such a cycle is that calcium chloride is the cheapest and most readily available desiccant; however its dehumidification performance is sensitive to ambient conditions. On the other hand lithium chloride and lithium bromide have good dehumidification effectiveness but are more expensive. Thus a dual loop cycle is developed in which calcium chloride is used in the first loop while lithium bromide is used in the second loop. The authors also mention that for higher inlet air temperatures, a higher fraction of the latent load is removed by calcium chloride. Furthermore, the regeneration temperatures mentioned for calcium chloride and lithium bromide are 55C and 75C respectively.

2.3.2 Liquid desiccant regenerators

Mei and Dai (2008) list and describe of three types of regenerator model analysis, namely finite difference model, effective NTU model and model based on fitted algebraic equations. Of these, the finite difference model provides the most accurate results.

There are three types of liquid desiccant air contacting equipment used in absorbers/regenerators (Jain & Bansal, 2007). These are spray towers, packed bed towers and falling film columns. Spray towers make use of nozzles to spray the liquid desiccant as droplets down a tower, creating large areas for contact of air and liquid desiccant. The advantages of spray cool towers are that they are low cost, compact and have low pressure drop on the air side. However, they do not provide good heat exchange effectiveness and are susceptible to carryover of liquid desiccant in to the air stream.

The packed bed towers use various types of packing material in order to provide large surface area of contact between air and the liquid desiccant. The advantages of the packed bed tower are that they are highly efficient, provide large contact area and contact time and are compact in size. However they cannot provide internal cooling/heating and thus the desiccant solution needs to be cooled/heated prior to entering the tower. Theoretical model developments have been made by Factor and Grossman (1980), Gandhidasan(2004), and Gandhidasan (2005). Experimental investigations for absorber and regenerator using packed bed towers have been performed by Yin, Zhang, and Chen (2007)

Falling film columns consist of tubes or parallel plates on which liquid desiccant is sprayed and the desiccant is allowed to flow down by gravity as thin films. The air flows in between the tubes/plates in a parallel, counter or cross flow configuration, carrying away the water vapor from the weak desiccant solution in the case of a regenerator. Falling film columns have low pressure drop, high contact are per unit volume and low initial cost. Experimental investigations on this have been conducted by (Jain, Dhara, & Kaushi, 2000)and (Lowenstein, Slayzak, & Kozubal, 2006) where the latter have developed a very low flow, zero carry over liquid desiccant air conditioning system. They have done this through internally cooling/heating the desiccant in order to allow for adequate dehumidification/regeneration at the low flow rates.

Ali, Vafai, and Khaled (2003) have developed a simple model of falling film absorber/regenerator using nano particle suspensions. They have reported that a parallel flow configuration is better in the dehumidification process for the entire range of parameters investigated in the work while counter flow configuration is better in the regeneration process where the channel height can be varied and the Reynolds number for the desiccant is low. Moreover for dehumidification, they have reported that low Reynolds number for air flow is desirable and leads to better performance while for regeneration high Reynolds numbers lead to better performance. Lastly the increase in the height of the channel increases the dehumidification and regeneration rate for both parallel and counter flow configurations.

Hueffed, Chamra, and Mago (2009) have developed a simplified model of a falling film type liquid desiccant dehumidifier/regenerator for a parallel, counter and cross flow of air through parallel plates. The simplified model was within 5% agreement with the results of a finite difference model for a parallel flow arrangement.

Yin and Zhang (2010) have compared the use of internally heated and adiabatic regenerators. They conclude that the internally heated type provides a higher regeneration rate and efficiency. Moreover the internally heated regenerator provides higher regeneration efficiency at low flow rates of desiccants and low flow rates in turn prevents carryover of the desiccant in to the air stream. They also highlight that higher air temperature leads to a higher regeneration rate but lower regeneration efficiency due to the extra heat supplied to the air.

Wurtz, Maalouf, Mora, & Allard (2005) discusses a solar desiccant cooling system installed in Chambery, France using Lithium Chloride as the desiccant. The regeneration temperature for lithium chloride is mentioned to range between 40C to 70 C and the hot water is produced by flat plate collectors in this case.

2.4 Humidification Dehumidification Desalination

Narayan et al (2010) discuss the different combinations of open loop/closed loop and water/air cycles for HDH desalination. They mention that HDH desalination has a promising prospect in small scale decentralized water production and requires almost no brine pretreatment before disposal. They suggest that the air should be heated after the humidifier in the air heating cycle in order to recover the maximum amount of heat in the dehumidifier and conclude that the multi effect closed air loop open water loop cycle is the most energy efficient.

Fath and Ghazy (2002) investigated a HDH cycle with a solar air heater input. They found that the air heater efficiency significantly affects the water production rate while the dehumidifier effectiveness has an insignificant effect on productivity. They also found water productivity to increase by increasing the solar intensity, ambient temperature and decreasing the wind speed. They conclude that increasing the air velocity to a certain limit leads to an increased productivity after which there is no significant effect.

Al-Enezi, Ettouney, and Fawzy (2006) designed and tested a low temperature water fed HDH cycle. The motivation for this low temperature device was for cost savings in the heating device investment (solar collectors, water heater etc.). They found that high water temperature, high air flow rate, low cooling water temperature and low water flow rate leads to increased production rates. A numerical model of the humidifier and dehumidifier was also developed.

The literature search yielded no work previously performed on a hybrid liquid air collector for simultaneous heating of water and air using a perforated plate fin configuration or any other design.

CHAPTER 3

---

3 LATSC Numerical Model

Figure 3.1 shows a schematic of the LATSC. A numerical model is developed based on the following assumptions for the construction and operation of the collector:

1. Uniform flow of water in the tubes
2. Uniform flow of air through perforations
3. Uniform distribution of perforations
4. Negligible starting length of boundary layer
5. Flat plate
6. No leakage

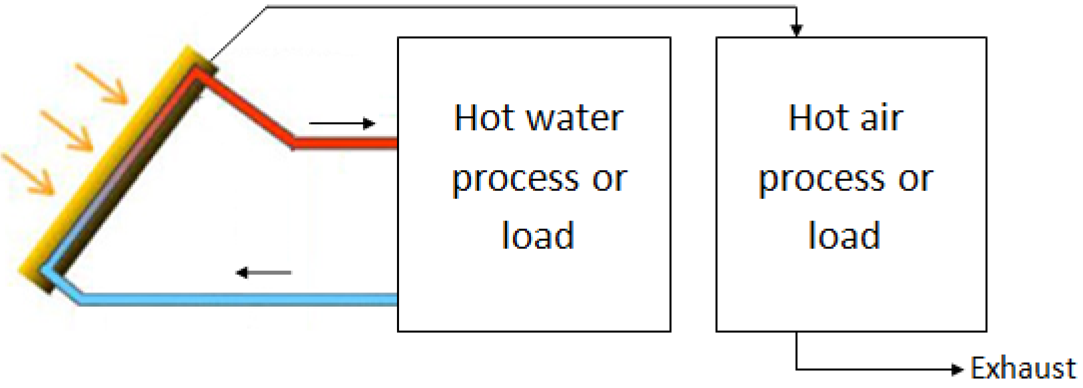

Figure 3.1: Schematic of LATSC supplying heat to two processes. Processes that require both hot air and hot water may be the most promising applications of LATSC.

The first task in the development of a numerical model of the LATSC was the identification of the heat transfer mechanisms from the absorber plate and from the back of the collector. A schematic diagram in Figure 3.2 shows the different modes of heat transfer from the plate.

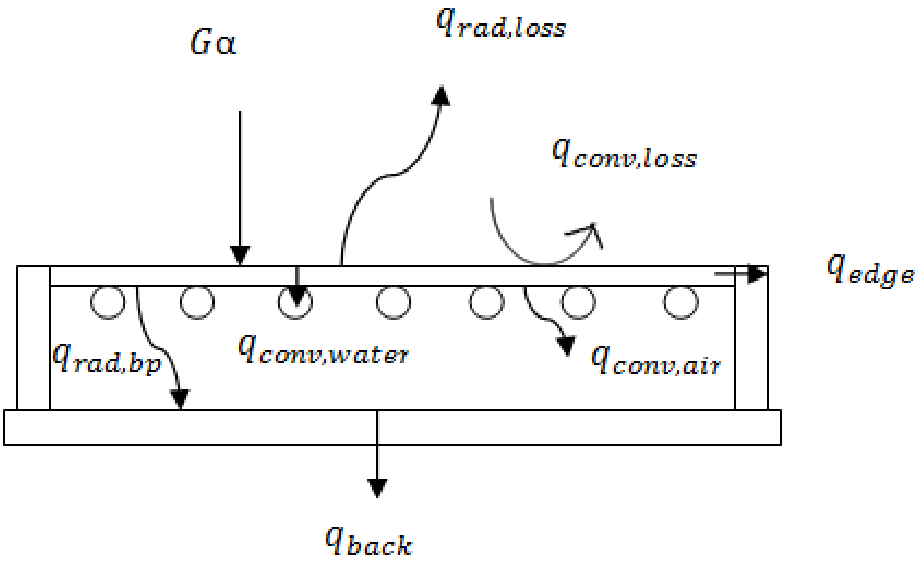

Figure 3.2: Heat loss paths from the absorber plate

Here the losses are categorized as convective and radiative front of plate losses ($q_{conv,loss}$, $q_{rad,loss}$), convective and radiative back of plate losses ($q_{conv,air}$, $q_{rad,bp}$) and back of collector losses (q_{back}) in which radiation and convection modes are combined. The useful energy transferred to the water in the tubes is ($q_{conv,water}$ or q_u). As the absorber plate of the collector is of the fin and tube type, the established heat transfer analysis through a fin can be applied as long as all other heat transfer mechanisms from the plate are correctly dealt with. Thus the heat transferred to the air sucked through the plate ($q_{conv,air}$) is a considered to be a loss from the plate in order to evaluate the heat transferred to the water and the consequent temperature rise. To perform a heat balance on the collector, an elemental area of the collector absorber plate is analyzed in Figure 3.3.

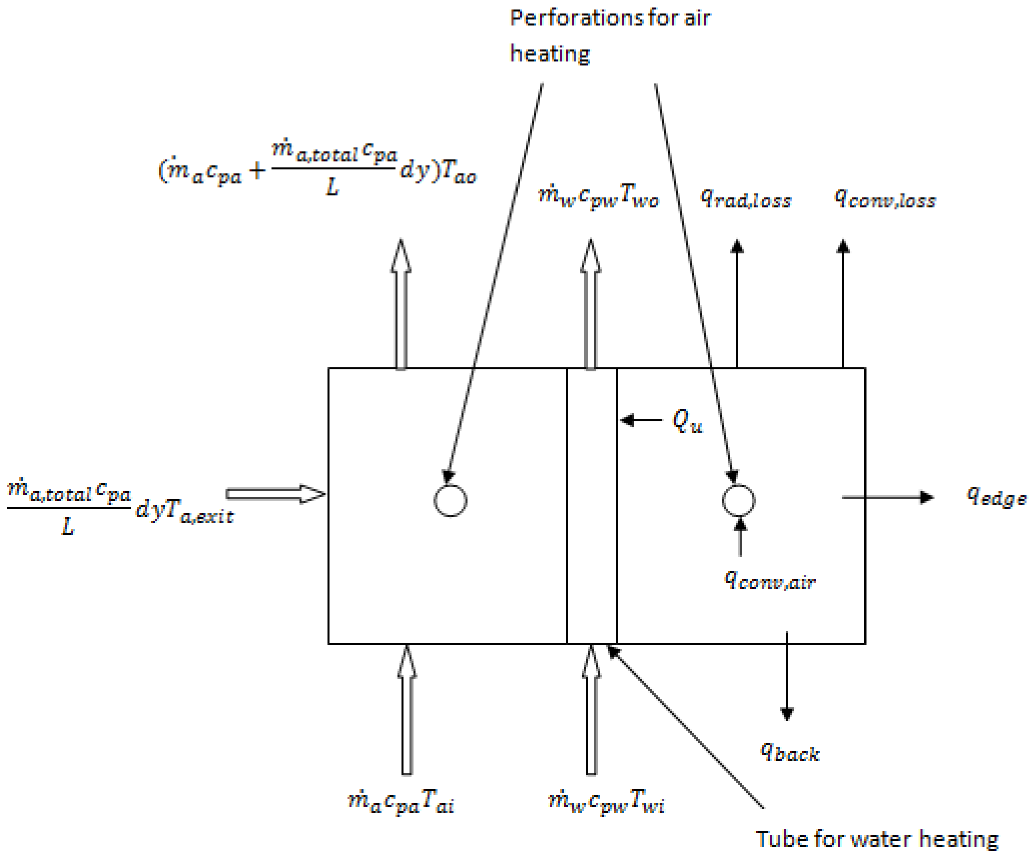

Figure 3.3: Energy balance on an elemental area of the absorber plate.

The heat transfer process shown are distributed over the plate but for clarity advection terms are shown on the left and convection and radiation on the right. Here the left hand side of Figure 3.3 deals with the enthalpy balance of air where the enthalpy of air entering from the back of the element is $\dot{m}_a cp_a T_{ai}$ while that entering through the plate is $\frac{\dot{m}_{a,total}\, Cp_a}{L} dy\, T_{a,exit}$. The outlet enthalpy of air through the element is $(\dot{m}_a + \frac{\dot{m}_{a,total}}{L} dy) cp_a\, T_{ao}$.

The right side of Figure 3.3 deals with the enthalpy balance of the water. The balance follows as:

$$q_u = (G\alpha - (q_{rad,loss} + q_{c,air} + q_{conv,loss} + q_{back} + q_{edge})) \tag{1}$$

In order to determine the useful heat transferred to the water (q_u), all the other heat transfer mechanisms need to be evaluated first.

3.1 Convective heat transfer to suction air

The first to be evaluated is the heat transferred to the air flowing through the holes, $q_{c,air}$. This is done by applying correlations of Kutscher(1993). The Nusselt number for air flow through a low porosity plate is:

$$Nu_h = 2.75\left(\left(\frac{pitch}{D_h}\right)^{-1.21} {Re_h}^{0.43} + 0.011 por * Re_h \left(\frac{V_w}{V_s}\right)^{0.48}\right) \tag{2}$$

where

$$Re_d = \frac{V_s D_h}{por * \nu_a} \tag{3}$$

And the suction velocity V_s is given by:

$$V_s = \frac{\dot{m}_a}{\rho_a A(1-\frac{D_t}{s})} \tag{4}$$

Normally for a transpired solar collector the suction velocity is simply given by:

$$V_{s,t} = \frac{\dot{m}_a}{\rho_a A_c} \tag{5}$$

However in this case there is a small patch between two patches of perforation where no holes can be drilled due to the presence of the tubes as shown in Figure 3.4. Figure 3.4 shows one tube and the two half fins to highlight the area in between the fins which cannot be perforated where W is the width of the collector, L is the length of the collector, D_t is the diameter of the tubes and s is the separation between the tubes.

Thus the perforated area is not equal to the total area of the collector. The perforated area (A_p) can be expressed as:

$$A_p = A_c(1 - \frac{Dt}{s}) \tag{6}$$

This difference in the perforated and absorber area requires the modification of equation (5) to equation (4).

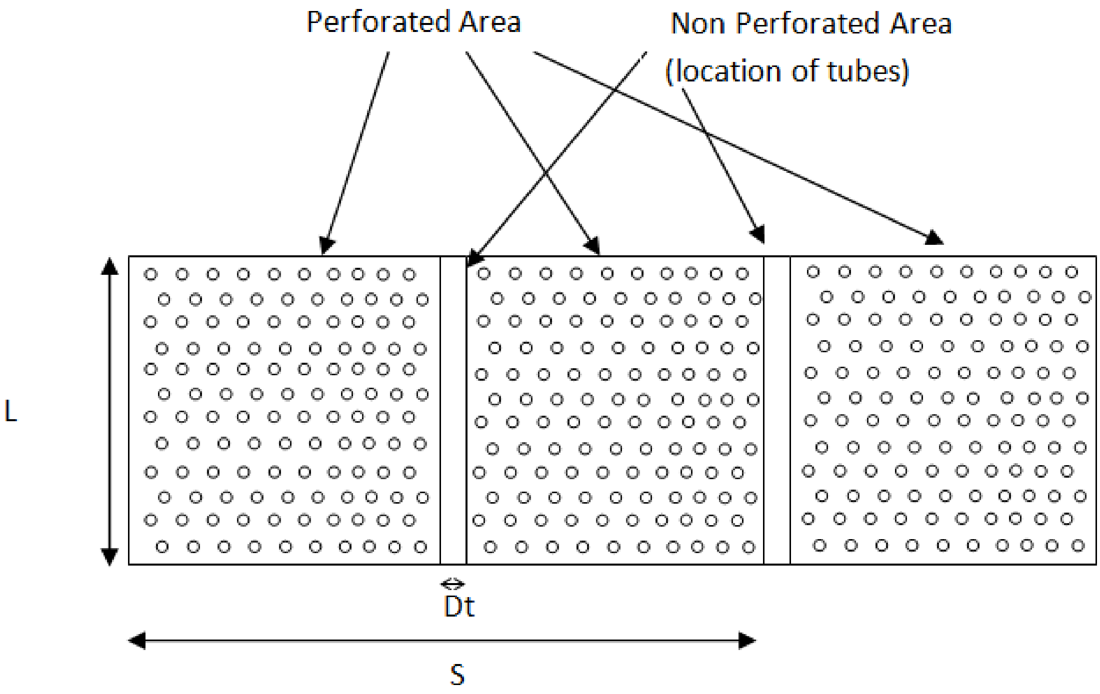

Figure 3.4: One tube and two half fins of the collector.

From the Nusselt number we obtain the heat transfer coefficient for air flowing through the holes as:

$$U_h = \frac{Nu_h k_a}{D_h} \tag{7}$$

The heat exchange effectiveness of the plate is a function of NTU which can then be obtained using the general formula (Incropera, Witt, Bergman, & Lavine, 2006):

$$NTU = \frac{U_h A}{(\dot{m}C_p)_a} = \frac{U_h A_{pl}}{\rho_a \mathrm{V_s C_{pa} A_p}} \tag{8}$$

Where the plate area, A_{pl}, is the solid plate area between the holes. The ratio of the plate area to perforated area can be expressed in terms of porosity as:

$$\frac{A_{pl}}{A_p} = 1 - por \tag{9}$$

This leads to the modified NTU equation:

$$NTU = \frac{U_h(1-por)}{\rho_a \mathrm{V_s C_{pa}}} \tag{10}$$

The heat exchange effectiveness can be finally written as:

$$\varepsilon_{hx} = 1 - \exp\left(-NTU\right) \tag{11}$$

The heat exchange effectiveness correlation developed by Kutscher(1993) is for air flow through a perforated plate assuming that the plenum behind the plate is large (200-300mm depth). For smaller plenums (50-130mm depth) as in the LATSC, a modification to the heat exchange effectiveness needs to be applied which is found in literature(Biona, Culaba, Serafica, & Mundo, 2005):

$$\varepsilon_{hx,mod} = \varepsilon_{hx}\,(0.9589 + 0.0004d_p + 0.000000032d_p^2) \tag{12}$$

Where d_p is the plenum depth and is in mm. The modified correlation above is valid for plenum depths from 50mm to 130mm.

From the heat exchange effectiveness of the plate, we can obtain the heat transferred to the holes in the plate in terms of the mean plate temperature of the differential element (T_{pl}) and the ambient temperature, T_{amb}, as:

$$q_{c,air} = \varepsilon_{hx,mod} W (T_{pl} - T_{amb}) dy \tag{13}$$

3.2 Convective Front Loss

Kutscher has also developed a correlation for the heat transfer coefficient for wind losses from the front of a perforated plate in terms of wind velocity, V_w and suction velocity, V_s:

$$U_{wf} = 0.82 \frac{V_w v_a \rho_a c_{pa}}{V_s L} \tag{14}$$

Equation(13) can be directly used to determine the total convective front losses as:

$$q_{conv,loss} = U_{wf}(T_{pl} - T_{amb}) \tag{15}$$

3.3 Radiative Front Losses

For the model it is assumed that the radiation from the front of the absorber plate is predominantly to the sky. The sky model developed by Berdahl and Martin(Duffie & Beckman, 1980) is used to determine the effective sky temperature in terms of the dry bulb temperature (T_{amb}), dew point temperature (T_{dp}) and the hour from midnight (*h*).

$$T_{sky} = T_{amb}(0.711 + 0.0056T_{dp} + 0.000073{T_{dp}}^2 + 0.013\cos(15h))^{1/4} \tag{16}$$

Since the effective sky temperature is the temperature of a black sky that would result in the same heat exchange, the radiation heat transfer to the sky can be expressed as:

$$q_{rad,loss} = \epsilon\sigma({T_{pl}}^4 - {T_{sky}}^4)Wdy \tag{17}$$

Where ϵ is the emissivity of the plate while σ is the Stephan Boltzmann constant.

3.4 Edge Losses

The edge loss coefficient for heat loss from the absorber plate can be expressed as:

$$U_e = \frac{k_e}{t_e}(\frac{A_e}{A_c}) \tag{18}$$

Thus the heat loss through the edge is:

$$q_{edge} = U_e(T_{pl} - T_{amb})Wdy \qquad (19)$$

3.5 Back Losses

The back losses of the collector result from radiation from the back of the absorber plate to the bottom of the plenum, and convection between air and bottom of plenum, followed by heat conduction through the back insulation to the collector back and convective and radiative heat loss at the back of the collector. The radiation heat transfer coefficient for heat transfer between the absorber plate and back plate is given by:

$$U_{pr} = \frac{\sigma({T_{pl}}^2+{T_{bp}}^2)+(T_{pl}+T_{bp})}{\frac{1}{\epsilon_{ab}}+\frac{1}{\epsilon_{bp}}-1} \qquad (20)$$

where T_{bp} is the back plate temperature and ϵ_{ab} and ϵ_{bp} are the back of the absorber plate and bottom of channel emissivities. For the convective heat transfer from the back plate, the air is considered to be flowing through the channel in laminar flow with the upper plate being heated with uniform flux and lower plate insulated. For this case the Nusselt number obtained from literature (Incropera, et al., 2006) is 5.39. The heat transfer coefficient can be expressed as:

$$U_p = \frac{Nu_p k_a}{D_p} \qquad (21)$$

Where D_p is the hydraulic diameter of the plenum:

$$D_p = \frac{4A_{cr}}{P} \qquad (22)$$

The total heat transfer from the front of the back plate is:

$$q_{back,loss} = U_{pr}(T_{pl} - T_{bp}) + U_p(T_{bp} - T_{ai}) \qquad (23)$$

The heat transfer coefficient for conduction through the back insulation is given by:

$$U_{bi} = \frac{k_{bi}}{t_{bi}} \tag{24}$$

The heat transferred through the back insulation is:

$$q_{back} = U_{bi} * (T_{bp} - T_{bc}) \tag{25}$$

Furthermore the convective heat transfer coefficient at the back of the collector is:

$$U_{wb} = \frac{Nu_{wb} k_a}{W} \tag{26}$$

Where:

$$Re_{wb} = \frac{V_w W}{\nu_a} \tag{27}$$

$$Nu_{wb} = 0.664\left({Re_{wb}}^{0.5} * {Pr_{wb}}^{0.33}\right) \tag{28}$$

The radiative heat transfer coefficient from the back of the collector to ground is:

$$U_{br} = \frac{\sigma\left({T_{bc}}^2 + {T_g}^2\right) + \left(T_{bc} + T_g\right)}{\frac{1}{\epsilon_{bc}} + \frac{1}{\epsilon_g} - 1} \tag{29}$$

where the ground temperature is assumed to be equal to ambient temperature.

The total heat transfer from the back of the collector is:

$$q_{back,loss} = U_{wb}(T_{bc} - T_{amb}) + U_{br}\left(T_{bc} - T_g\right) \tag{30}$$

3.6 Combined Losses

Having developed the equations for all the heat transfer pathways, it is now possible to express the combined heat transfer coefficient in terms of the combined heat loss and (T_{pl}- T_{amb}) as:

$$U_l = \frac{q_{rad,loss}+q_{c,air}+q_{conv,loss}+q_{edge}+q_{back,loss}}{(T_{pl}-T_{amb})} \tag{31}$$

Now the heat transferred to the water in the tubes can be calculated from the energy balance equation (1) and equation (31) as:

$$Q_u = W * dy * \left(G - U_l\left(T_{pl} - T_{amb}\right)\right) \tag{32}$$

As the plate temperature varies in both the x and y direction, it is useful to express Q_u in terms of the fluid inlet temperature T_{fi}:

$$Q_u = W * dy * F'\left(G - U_l\left(T_{fi} - T_{amb}\right)\right) \tag{33}$$

Where F' is the collector efficiency factor which accounts for thermal resistances between various points on the plate and the cooling water. Part of the resistance is due to the fin efficiency, F, of the collector plate. These factors are given by:

$$F' = \frac{\frac{1}{U_l}}{s\left(\frac{1}{U_l(D_t+(s-D_t)F)}+\frac{1}{C_b}+\frac{1}{\pi D_t h_{fi}}\right)} \tag{34}$$

where

$$F = \frac{tanh * m\frac{s-D_t}{2}}{m\frac{s-D_t}{2}} \tag{35}$$

and

$$m = \sqrt{\frac{U_l}{k_p \delta}} \tag{36}$$

The heat transfer coefficient for convection in the tube, h_{fi}, is given by:

$$h_{fi} = \frac{Nu_w k_w}{D_t} \tag{37}$$

where the Nusselt number correlation is for laminar, fully developed flow through a pipe with constant heat flux, given by:

$$Nu_w = 4.4 + b\left[\frac{\left(\frac{Re_w * Pr_w D_t}{L}\right)^n}{1+c\left(\frac{Re_w * Pr_w D_t}{L}\right)^o}\right] \tag{38}$$

where b, c, n and o are constants with the following values:

b= 0.00172

c= 0.00281

n= 1.66;

o= 1.29

The Prandtl number, Pr_w , velocity of water in tubes, V_{wa}, cross sectional area of tubes, A_t and Reynolds number of water flowing through the tubes, Re_w are given by:

$$Pr_w = \frac{\nu_w c_{pw} \rho_w}{k_w} \tag{39}$$

$$V_{wa} = \frac{\dot{m}_w}{\rho_w A_t} \tag{40}$$

$$A_t = \frac{\pi D_t N}{4} \tag{41}$$

$$Re_w = \frac{V_w D_t}{\nu_w} \tag{42}$$

Equating the thermal energy gain of the water via advection to the heat transferred to the tube, an ordinary differential can be obtained of the form:

$$\dot{m}_w c_{pw} \frac{dT_w}{dy} = Q_u \tag{43}$$

to solve for the water outlet temperature by integration.

Similarly the air side enthalpy balance can be cast as an ODE by using the following equation to replace $T_{a,exit}$:

$$\varepsilon_{hx,mod} = \frac{T_{a,exit} - T_{amb}}{T_{pl} - T_{amb}} \tag{44}$$

The ODE obtained to solve for the air outlet temperature is:

$$(\dot{m}_{ai} + \Delta\dot{m}_a)\frac{dT_a}{dy} = \frac{\dot{m}_{a,tot}}{L}\left[(1 - \varepsilon_{hx,mod})T_{amb} + \varepsilon_{hx,mod} T_{pl} - T_{ai}\right] + q_{bp} \tag{45}$$

where $\varepsilon_{hx,mod}$ is the heat exchange effectiveness of the perforated absorber plate.

Lastly a mass balance can be applied to solve for the air flow exiting each element.

$$\frac{d\dot{m}_a}{dy} = \frac{\dot{m}_{a,total}(y)}{L} \tag{46}$$

3.7 Uncoupled vs. Coupled heat transfer behind absorber plate

The model developed above does not take into account the heat transferred to the air as it moves up the back channel or plenum. According to Van-Decker et al. (2001) the back channel contribution is small. Nevertheless, there will be some heat transfer to the air due to the temperature gradient between the air in the plenum and the front (upper) and back (lower) plates as shown in Figure 3.5.

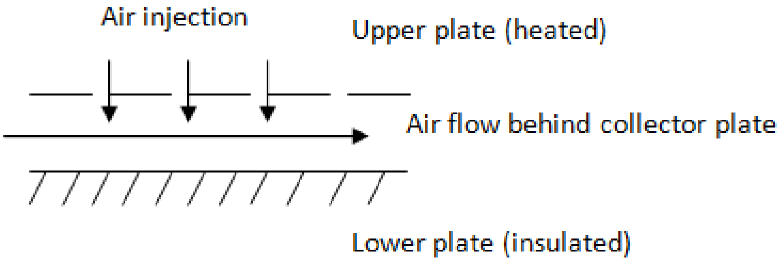

Figure 3.5: Heating of air in the back channel

To account for this heat transfer, the air is considered to be flowing through the channel in laminar flow with the upper plate being heated with uniform flux and lower plate insulated. For this case the Nusselt number obtained from standard tables (Incropera, et al., 2006) is 5.39. The heat transfer coefficient can be expressed as:

$$U_{ab} = \frac{Nu_{bp} k_a}{D_p} \tag{47}$$

where D_p is the hydraulic diameter of the plenum:

$$D_p = \frac{4A}{P} \tag{48}$$

The heat transferred to the air behind the collector is thus:

$$q_{ab} = U_p * (T_{pl} - T_{ai}) \tag{49}$$

For the coupled heat transfer model, this heat transfer term must be added to the enthalpy balance equation(1) and the right side of the ODE for air (45) to give:

$$q_u = (G\alpha - (q_{rad,loss} + q_{c,air} + q_{conv,loss} + q_{back} + q_{edge} + q_{ab})) * dy \tag{50}$$

and

$$(\dot{m}_{ai} + \Delta\dot{m}_a)\frac{dT_a}{dy} = \frac{\dot{m}_{a,tot}}{L}[(1 - \varepsilon_{hx,mod})T_{amb} + \varepsilon_{hx,mod}T_{pl} - T_{ai}] + q_{bp} + q_{ab} \tag{51}$$

3.8 Solving Procedure

The three ODEs developed were solved simultaneously using the software package Engineering Equation Solver (Klein, 2010). EES allows for the fast solving of multiple implicit non linear equations and it was particularly useful in solving for T_{pl} as T_{pl} could not be expressed explicitly. T_{pl} was then simultaneously used in the ODE solver to determine the outlet air and water temperatures for each node up till the last node. A flow chart depicting the solving procedure is shown in Figure 3.6. EES also provides an easy to use parametric table to facilitate the sensitivity analysis. Furthermore EES has an inbuilt library of air and water properties which can be called during the iterative solving procedure.

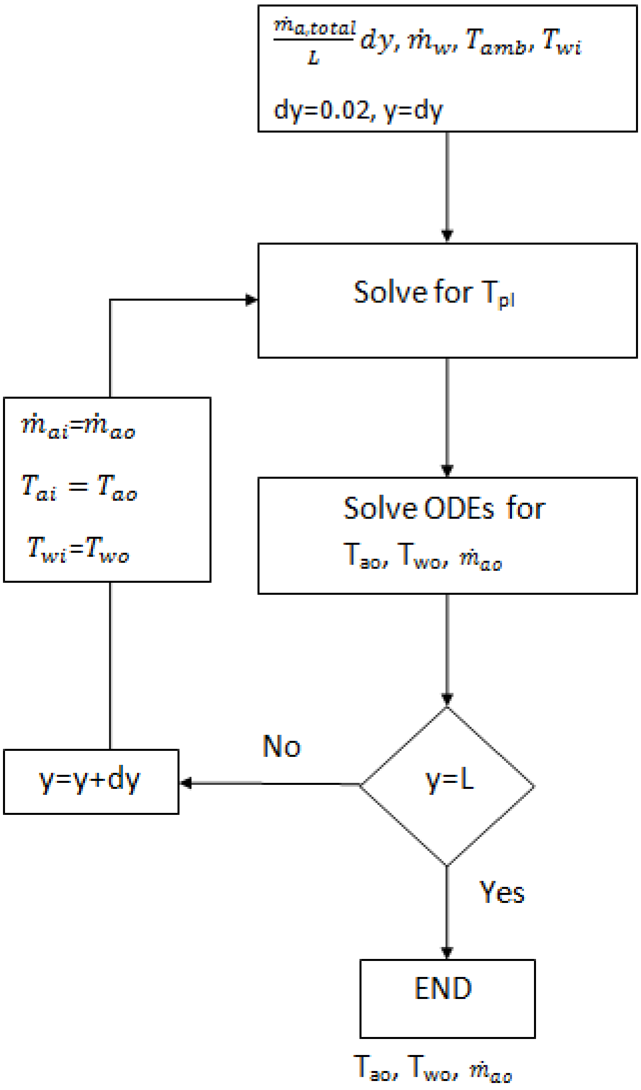

Figure 3.6: Flow chart showing solving procedure.

CHAPTER 4

4 Sensitivity Analysis

With the foregoing collector model we can observe the performance sensitivity of the collector to varying the ambient temperature (T_{amb}), inlet water temperature (T_{wi}), collector emissivity (ϵ), solar radiation (G), wind speed (V_w) and total thermal capacitance of air and water $(\dot{m}c_p)_{total}$. Moreover for each analysis, the ratio of thermal capacitance of air to total thermal capacitance ($R_{\dot{m}\mathrm{cp}}$) was varied to observe its effect on the efficiency of the collector along with the other varying parameters. The efficiency of the collector is given by:

$$\eta_c = \frac{\dot{m}_a C_{pa}(T_{ao} - T_{ai}) + \dot{m}_w C_{pw}(T_{wo} - T_{wi})}{G * A} \tag{52}$$

Two batches of sensitivity analysis have been performed. The first batch evaluates the performance of the collector to changes in $(\dot{m}c_p)_{total}$ and ($R_{\dot{m}\mathrm{cp}}$) with other physical and weather parameters held constant while the second batch aims at producing performance curves for the collector at ASHRAE 93 recommended water flow rate and its corresponding optimum air flow ratio. For both batches, three sets of analyses have been carried out. For all three analyses, the collector dimension, air properties, weather condition and solar radiation have been held constant at values specified in Table 4. 1 unless specified otherwise.

4.1 Batch 1

The first analysis was aimed at obtaining the performance of the collector with different $(\dot{m}c_p)_{total}$ entering the collector along with a range of values of $R_{\dot{m}\mathrm{cp}}$ from 0.1 to 0.9. The range of values of $(\dot{m}c_p)_{total}$ was from 5W/m^{2}K to 25W/m^{2}K at five equal intervals and the ambient temperature was maintained at =25^{o}C. The overall collector efficiency and the outlet water temperature were compared for varying $R_{\dot{m}\mathrm{cp}}$.The results obtained for these analyses are shown in Figure 4.1 and Figure 4. 3 for the model without heating of air behind the collector plate and in Figure 4. 2**Error! Reference source not found.** and Figure 4.4 when air is heated behind the collector plate.

Table 4. 1: Geometric parameters, fluid properties and baseline conditions used in the sensitivity analysis

Property	Value
Solar radiation (S)	800W/m^2
Wind speed(V_w)	3 m/s
Air temperature(T_{amb})	25 ^{o}C
Air density(ρ_a)	1.184kg/m^3
Air Viscosity (μ_a)	1.849*10^{-5} Ns/m^2
Air Cp (c_{pa})	1.007kJ/kgK
Length of collector (L)	2m
Width of collector (W)	1m
Plenum depth (D)	0.1m
Perimeter of plenum cross section	2.2m
Plate absorptivity	0.9
Plate emissivity	0.9
Hole diameter	0.00159m
Hole pitch (triangular pattern)	0.025m

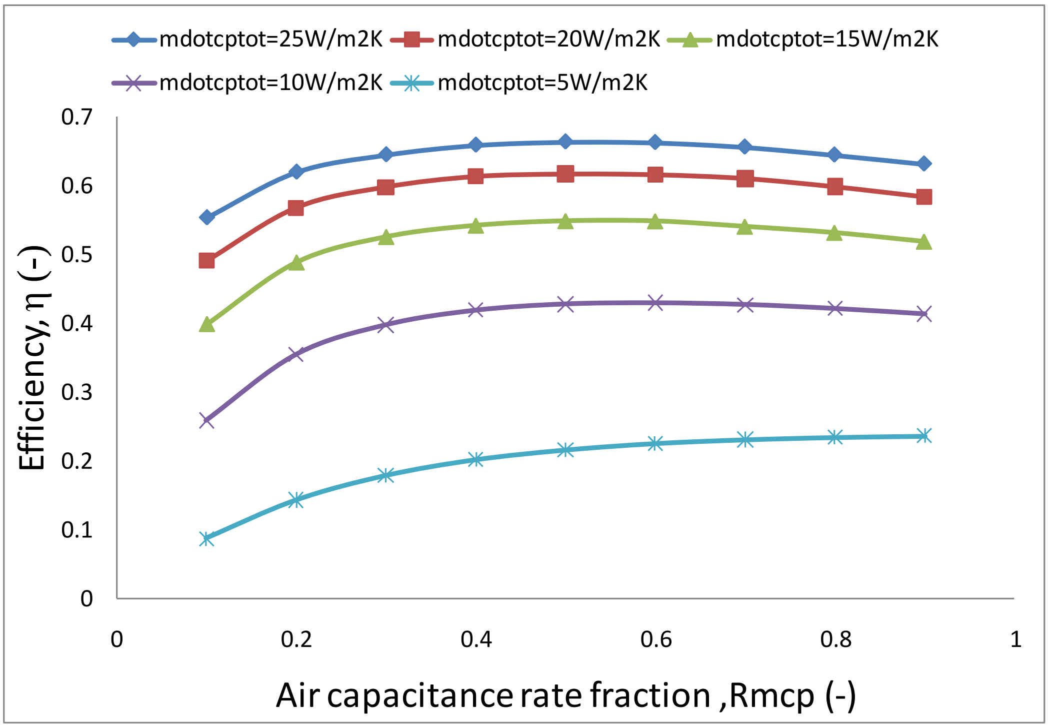

Figure 4.1: Efficiency vs. $R_{\dot{m}cp}$for range of $(\dot{m}c_p)_{total}$ with $T_{w,i} = T_{amb}$ = 25°C

uncoupled air heating.

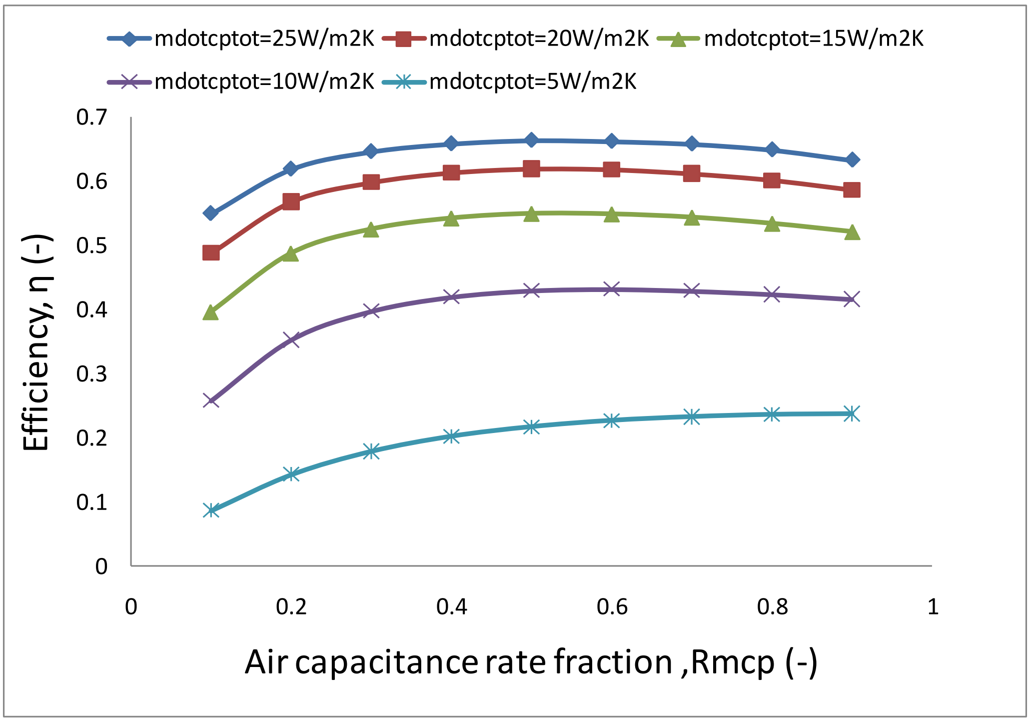

Figure 4. 2: Efficiency vs. $R_{\dot{m}cp}$ for range of $(\dot{m}c_p)_{total}$ with $T_{w,i}$ = T_{amb} = 25°C for coupled air heating.

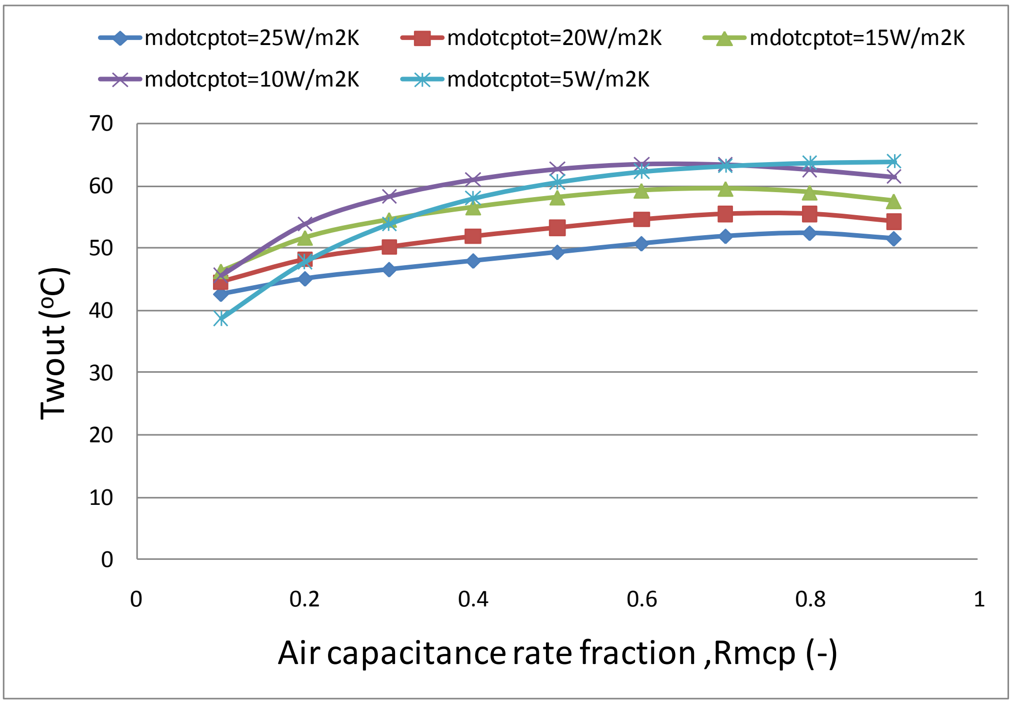

Figure 4. 3: Water outlet temperature vs. $R_{\dot{m}cp}$ for range of $(\dot{m}c_p)_{total}$ with $T_{w,i}$ = T_{amb} = 25°C for uncoupled air heating.

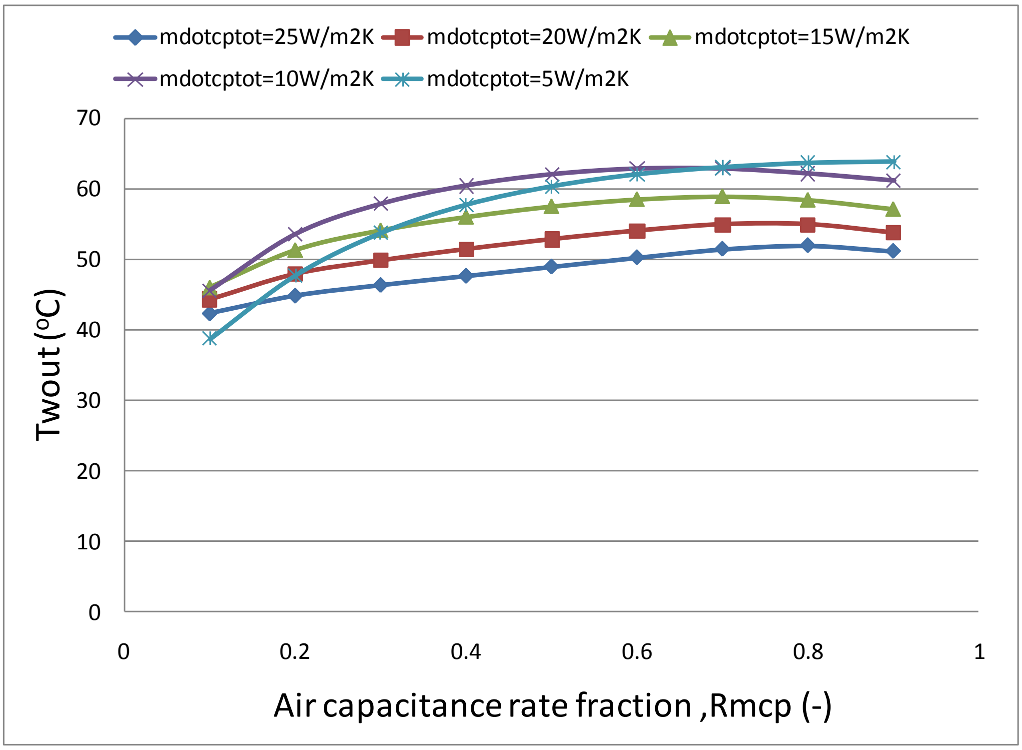

Figure 4.4: Water outlet temperature vs. $R_{\dot{m}\mathrm{cp}}$ for range of $(\dot{m}\mathrm{c_p})_{\mathrm{total}}$ with $T_{\mathrm{w,i}} = T_{\mathrm{amb}} =$ 25°C for coupled air heating.

The second set of analysis was performed by varying the inlet temperature of the water from 25°C to 115°C to obtain the efficiency of the collector. The ambient temperature for this analysis was fixed at 25°C and the $(\dot{m}c_p)_{total}$ was fixed at 15W/m^{2}K. The emissivity and $R_{\dot{m}\mathrm{cp}}$ was also varied to obtain a family of curves for emissivities and $R_{\dot{m}\mathrm{cp}}$ s of 0.1, 0.5 and 0.9. The results are shown in Figure 4.5, Figure 4.6 and Figure 4.7 respectively.

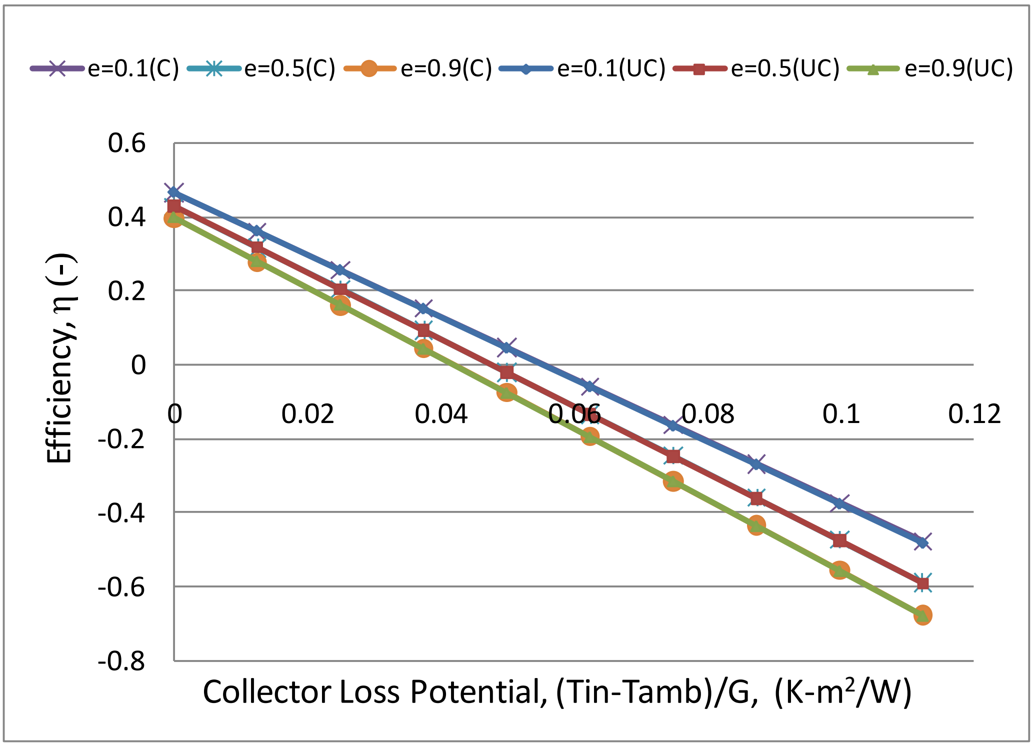

Figure 4.5: Efficiency vs. ΔT/G for $R_{\dot{m}cp}$= 0.1 and T_{amb} = 25°C for uncoupled (UC) and coupled(C) air heating behind plate.

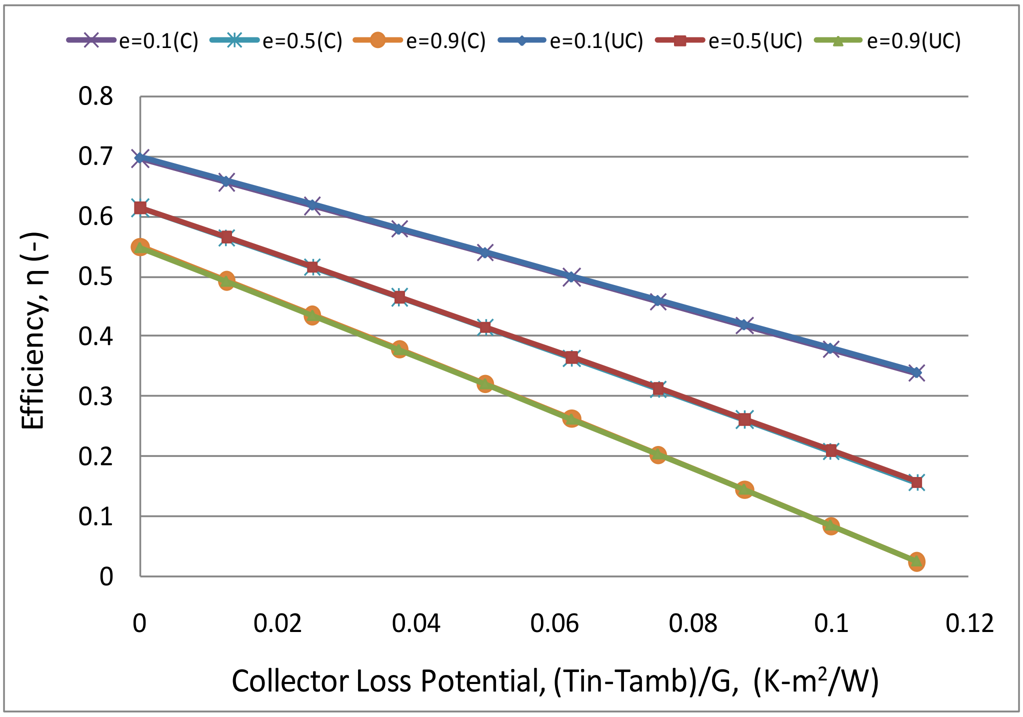

Figure 4.6: Efficiency vs. ΔT/G for $R_{\dot{m}\mathrm{cp}}$= 0.5 and T_{amb} = 25°C for uncoupled (UC) and coupled(C) air heating behind plate.

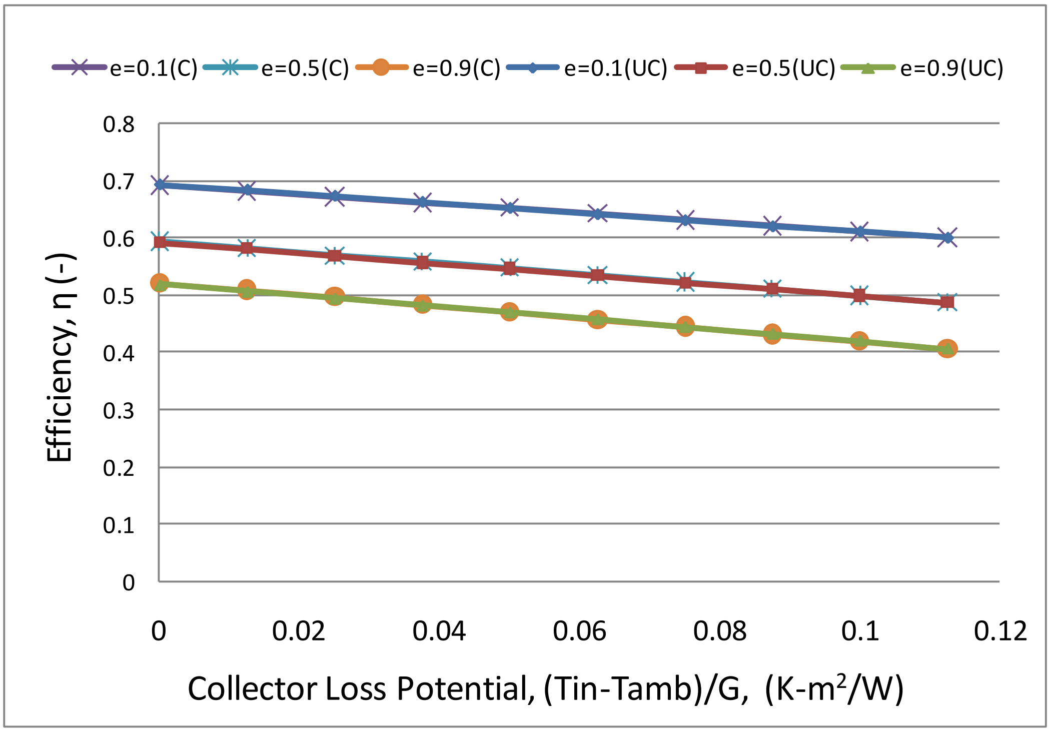

Figure 4.7: Efficiency vs. ΔT/G for $R_{\dot{m}\mathrm{cp}}$= 0.9 and T_{amb} = 25°C for uncoupled (UC) and coupled(C) air heating behind plate.

Table 4.2: Conditions used in sensitivity analyses

Parameter	Values
(1)Air temperature(T_{amb})	25,35,45(^{o}C)
(1)Water inlet temperature(T_{wi})	25-115 (^{o}C) with 10 ^{o}C intervals
(1)Air to total thermal capacity ratio($\dot{m}c_{p\ ratio}$)	0.1, 0.3, 0.5, 0.7, 0.9
(2)Solar radiation (G)	300, 500, 800 (W/m^2)
(2)Wind speed(V_w)	0, 3, 5 (m/s)

(1) G and Vw are fixed for the first two sensitivity exercises at values given in Table 4.1.
(2) G and Vw are only varied for the standard collector performance (Figures 4.8-12)

The third analysis develops standard performance curves for the collector for a wider range of varying parameters and conditions. For this analysis $(\dot{m}c_p)_{total}$ has been kept constant at 15W/m^{2}K , while $R_{\dot{m}\mathrm{cp}}$, V_w, T_{wi}, T_{amb} and G have been varied. The ranges of values for which these parameters have been varied are displayed in Table 4.2. The results from this analysis are illustrated in Figures 4.8-9 and Figures 4.10-11for uncoupled air heating and coupled air heating behind the collector plate.

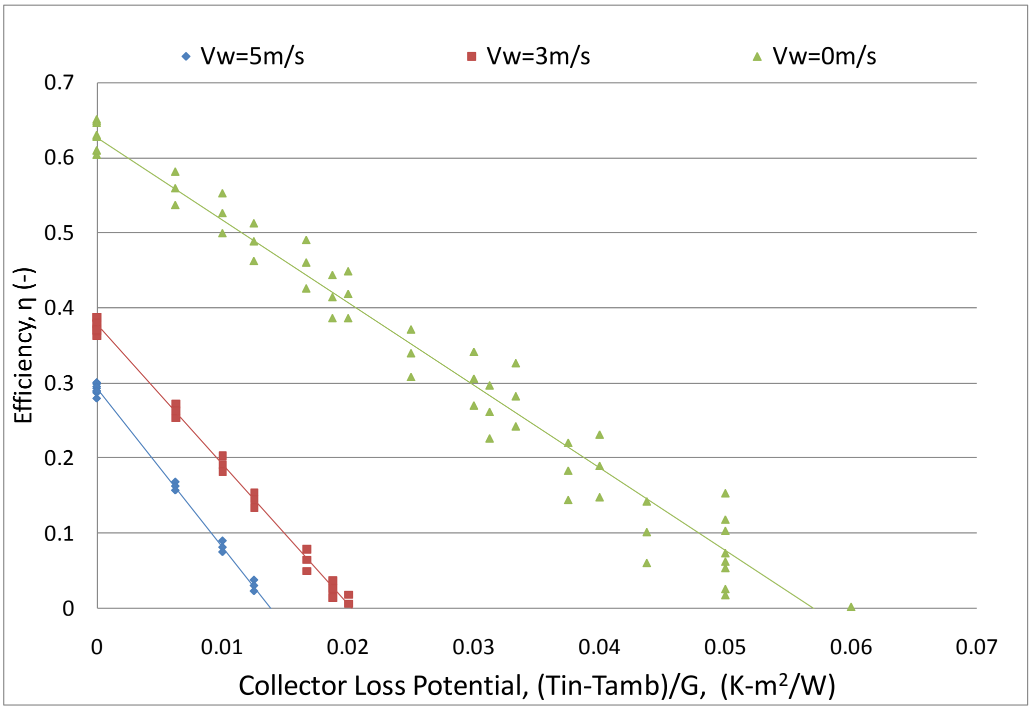

Figure 4.8: Efficiency vs. ΔT/G for $R_{\dot{m}\mathrm{cp}}$= 0.1, $(\dot{m}c_p)_{total}$=15W/m^{2}K and varying G, T$_{amb}$, T$_{win}$, and V$_w$ for uncoupled heating behind collector plate.

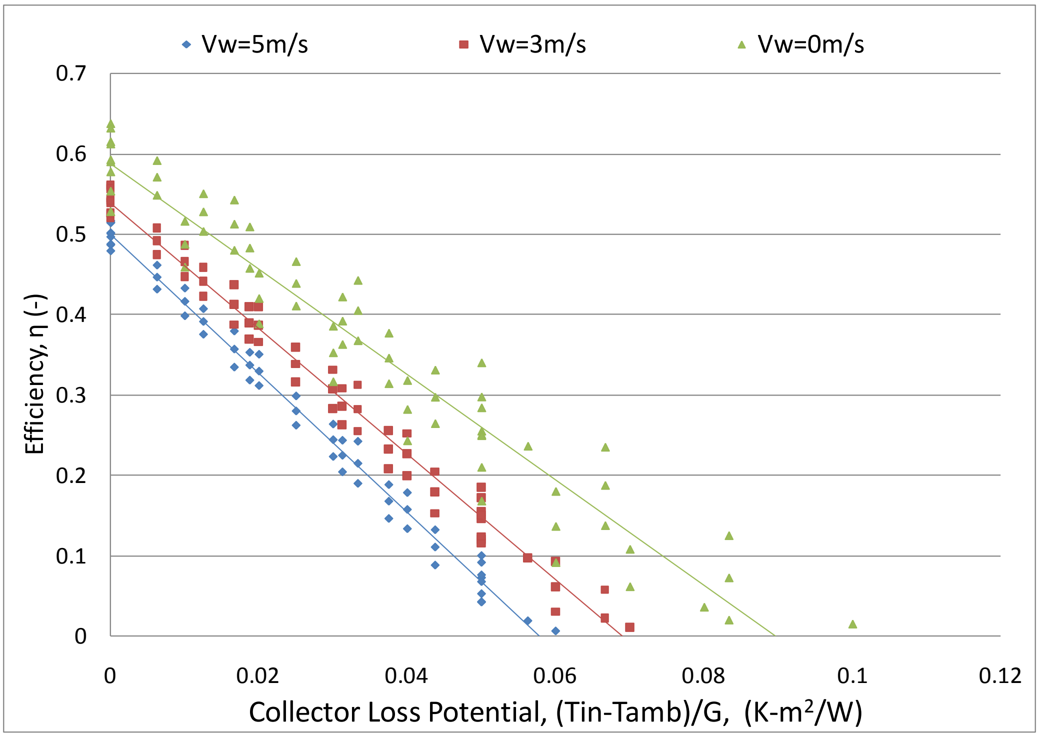

Figure 4.9: Efficiency vs. ΔT/G for $R_{\dot{m}\mathrm{cp}}$= 0.5, $(\dot{m}c_p)_{total}$=15W/m^{2}K and varying G, T$_{amb}$, T$_{win}$, and V$_w$ for uncoupled heating behind collector plate.

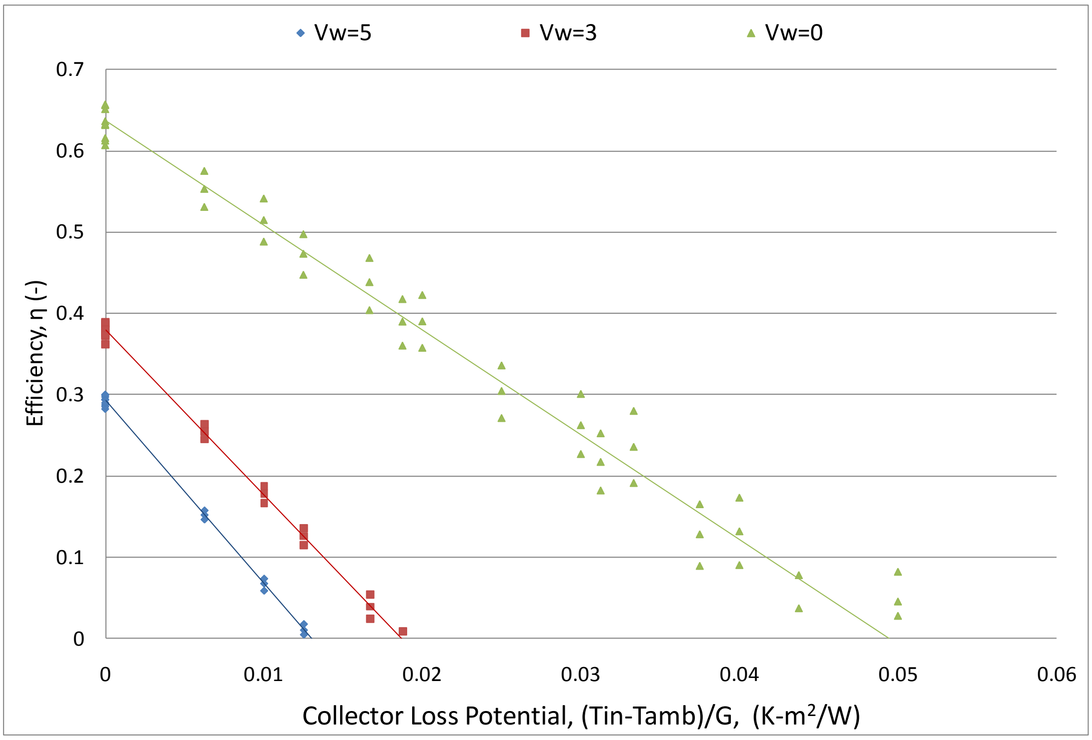

Figure 4.10: Efficiency vs. ΔT/G for $R_{\dot{m}\text{cp}}$= 0.1, $(\dot{m}c_p)_{total}$=15W/m^{2}K and varying G, T_{amb}, T_{win}, and V_w for coupled heating behind collector plate.

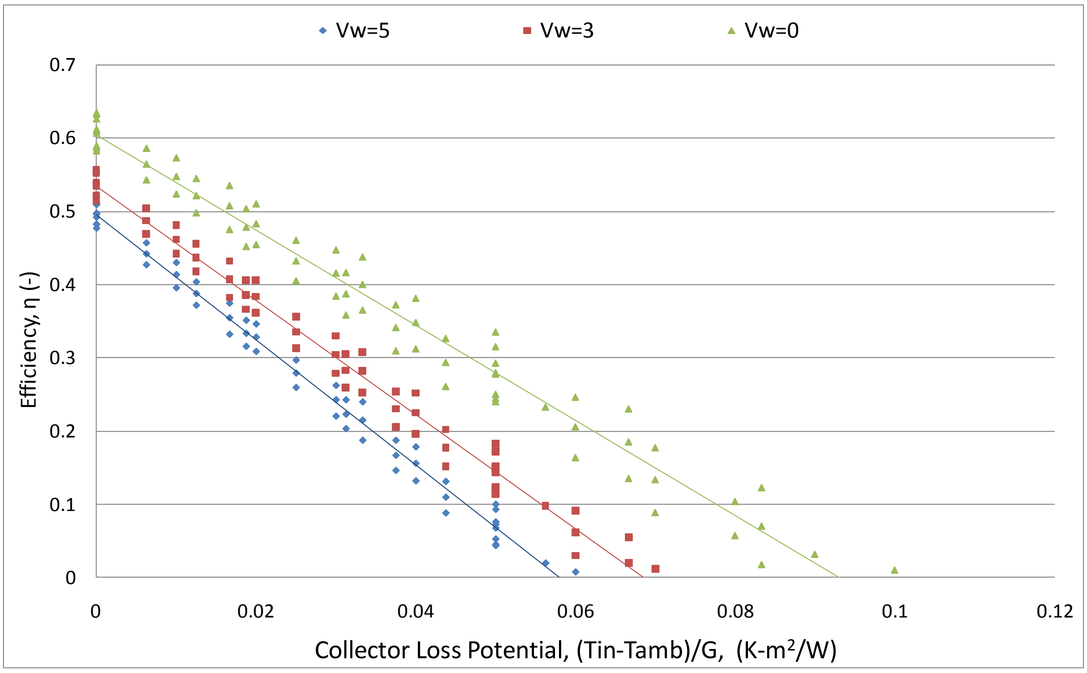

Figure 4.11: Efficiency vs. ΔT/G for $R_{\dot{m}\text{cp}}$= 0.5, $(\dot{m}c_p)_{total}$=15W/m^{2}K and varying G, T_{amb}, T_{win}, and V_w for coupled heating behind collector plate.

Finally the pitch and diameter of the holes was varied to assess the impact on the efficiency of the collector for the coupled model only. First the hole diameter was varied from 0.001 to 0.0055m, keeping the pitch constant at 0.025m. Then the hole diameter was kept constant at 0.00159m while the pitch was varied from 0.01 to 0.055m. This allowed for the collector performance to be simulated for a range of values of:

$$0.25 < \left(\frac{pitch}{D_h}\right)^{-1.21} {Re_d}^{0.43} < 1.039 \tag{53}$$

This range lies within the range of values for which equation (53) is valid. The analysis was performed for total capacitance rates of 30, 40 and 50W/m^{2}K, keeping the air capacitance ratio of 0.5. The results of these analyses are shown in Figure 4.12 and Figure 4.13 respectively.

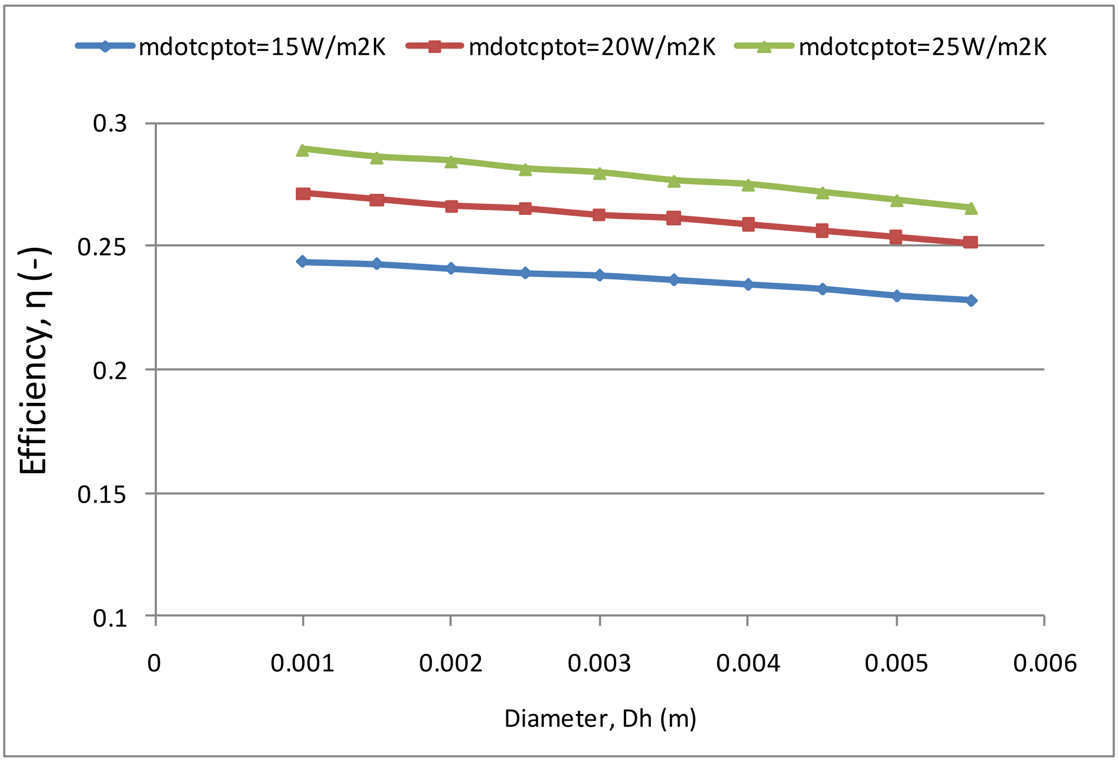

Figure 4.12: Efficiency vs. Hole Diameter for a constant pitch of 0.025m and air capacitance ratio of 0.5.

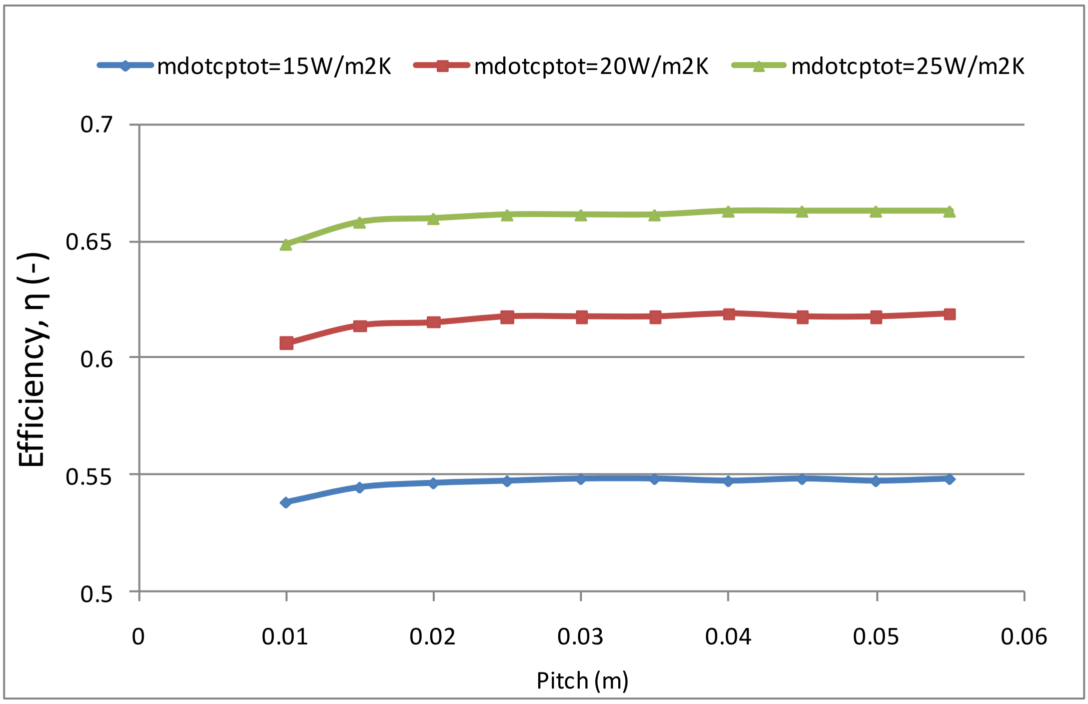

Figure 4.13: Efficiency vs. Pitch for a constant hole diameter of 0.00159m and air capacitance ratio of 0.5.

4.2 Batch 2

The sensitivity analyses performed above are for low flow rate applications. In order to compare the LATSC with a conventional flat plate collector, the model was simulated at a water flow rate of 0.02 kg/s-m^2, which is used for the testing of water heating collectors specified by ASHRAE 93. This amounts to a water thermal capacitance rate of 83.5 W/m^2-K. First the optimum air flow rate was determined for maximum heat transfer to the water. For this, the water thermal capacitance rate was kept constant at 83.5W/m^2-K while the air thermal capacitance rate was varied from 0 to 20 W/m^2-K for wind speeds of 1m/s, 3m/s and 5m/s. The water heating efficiency, air heating efficiency and total efficiency of the collector with varying air flow rates is shown in Figures 4.14-16.The air thermal capacitance rates at which the water heating efficiency was maximum was 2.5W/m^2-K, 5W/m^2-K and 6.5W/m^2-K (i.e R_{mcp} in the range .029~0.072) for wind speeds of 1m/s, 3m/s and 5m/s respectively.

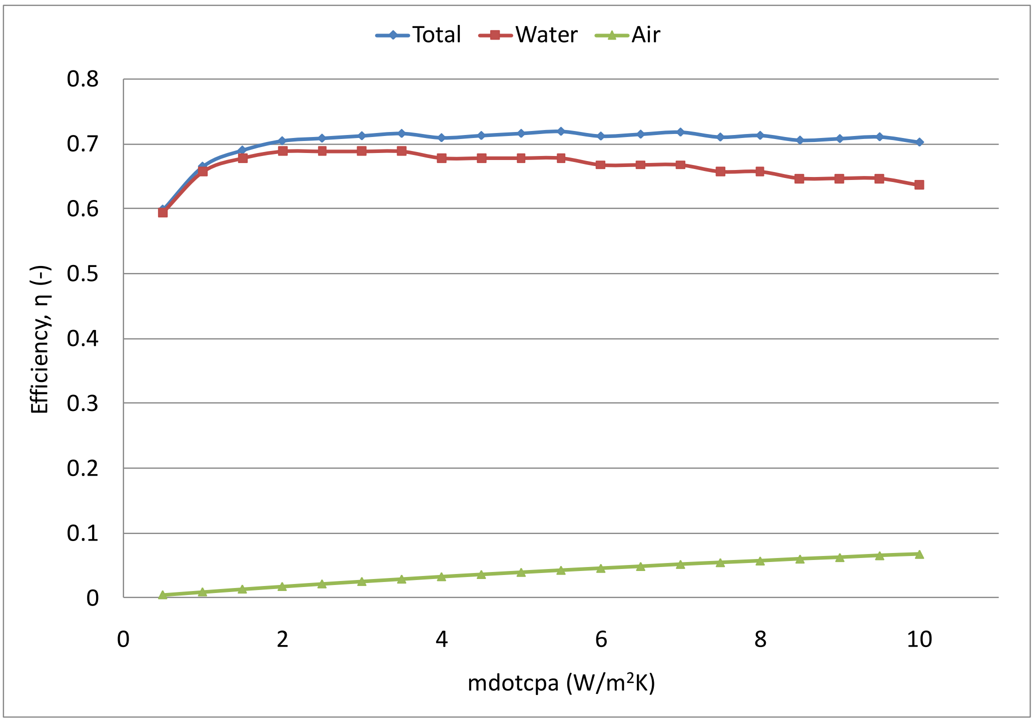

Figure 4. 14: Air, Water and Total thermal efficiencies of the collector with increasing air flow rate at V_w=1m/s.

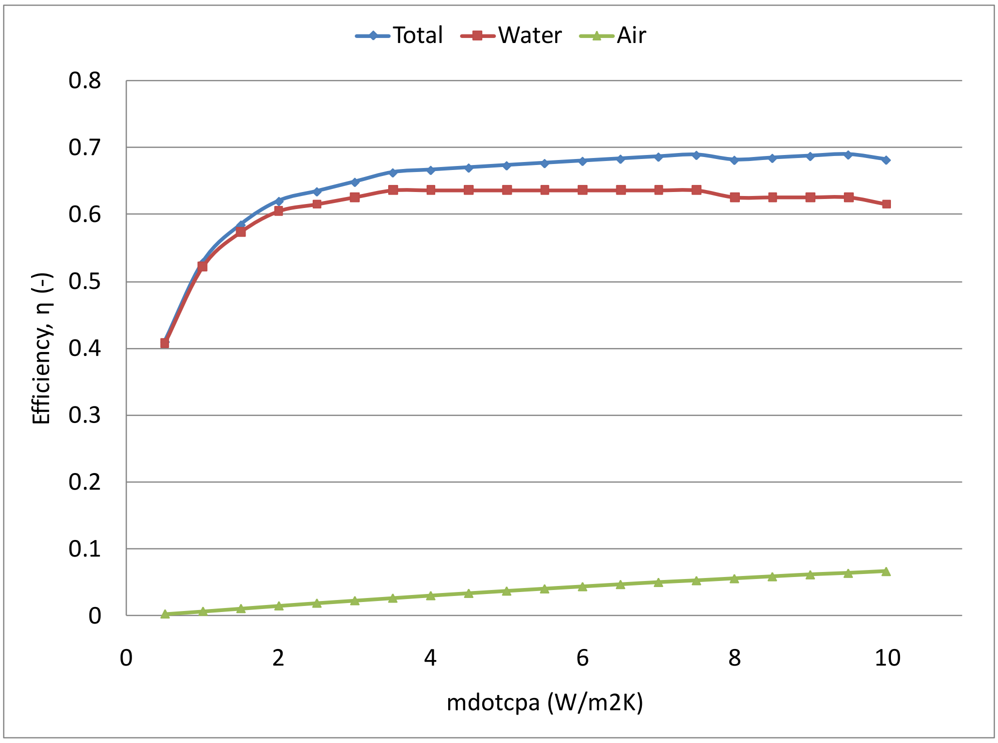

Figure 4.15: Air, Water and Total thermal efficiencies of the collector with increasing air flow rate at V_w=3m/s.

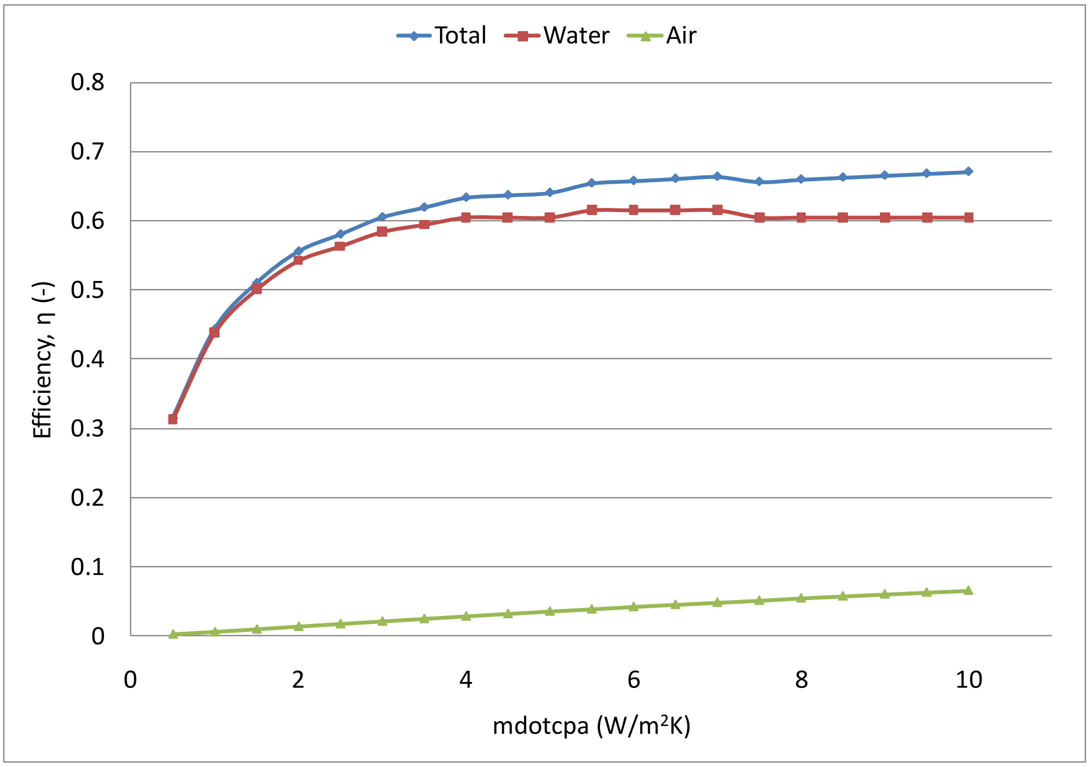

Figure 4.16: Air, Water and Total thermal efficiencies of the collector with increasing air flow rate at V_w=5m/s.

The collector was then simulated for wind speeds of 1m/s, 3m/s and 5m/s with their respective optimum air flow rates, varying the emissivity of the plate as well as the water inlet temperature. The input parameters for the model are those given in Table 4. 1. The values for the inlet water temperature are those given in Table 4.2. Figures 4.17-19 show families of curves for the total efficiency of the collector for varying $(T_{in}-T_{amb})/G$ and plate emissivities. Figure 4.20-22 show the water heating efficiency of the LATSC for varying $(T_{in}-T_{amb})/G$ and plate emissivities.

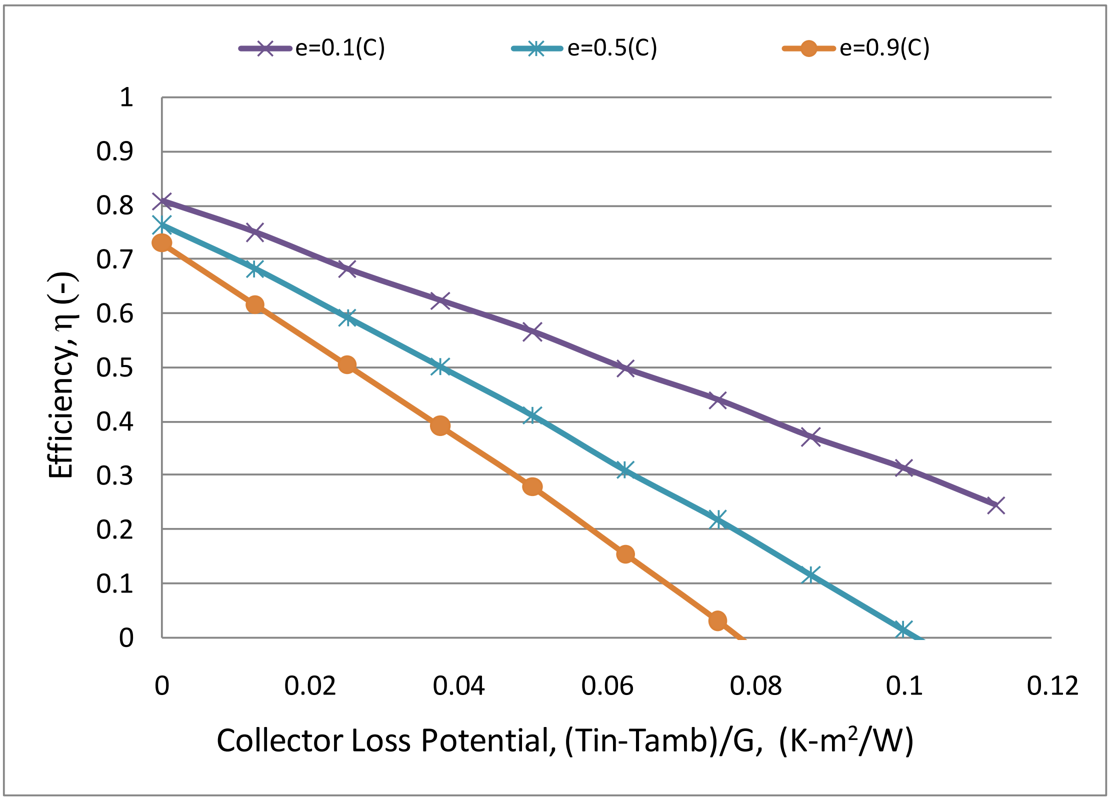

Figure 4.17: Total collector efficiency vs. ΔT/G at V_w=1m/s.

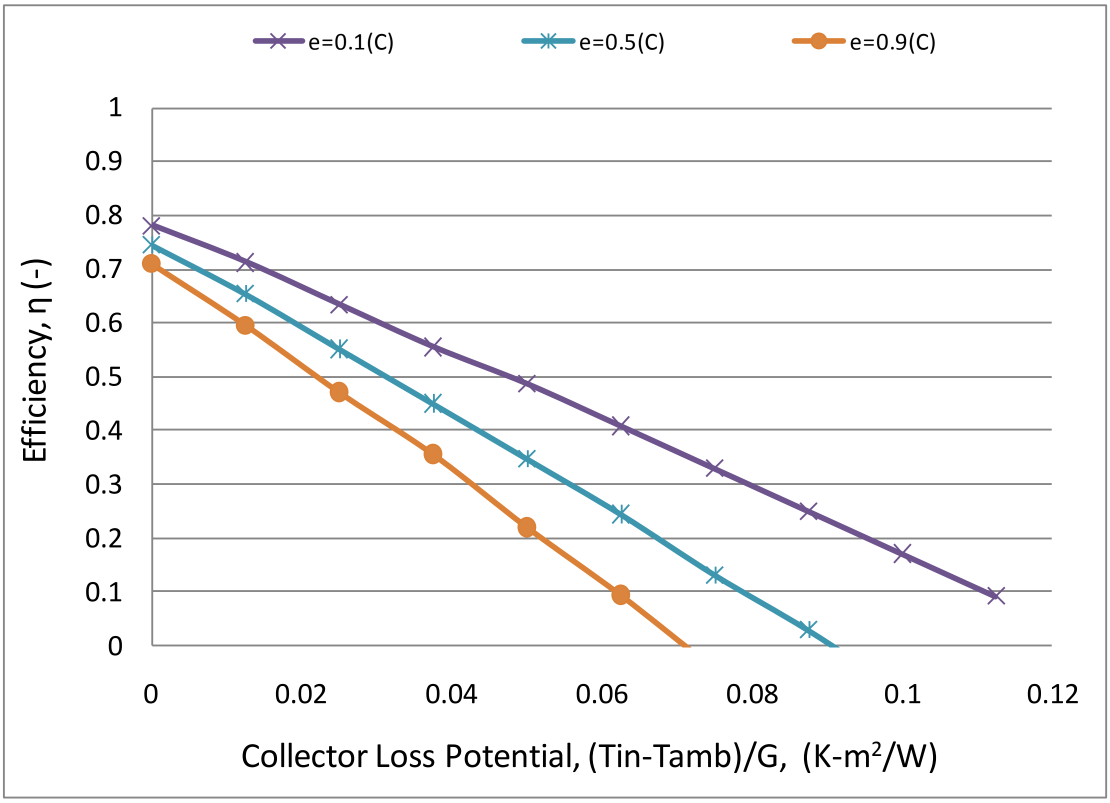

Figure 4.18: Total collector efficiency vs. ΔT/G at V_w=3m/s.

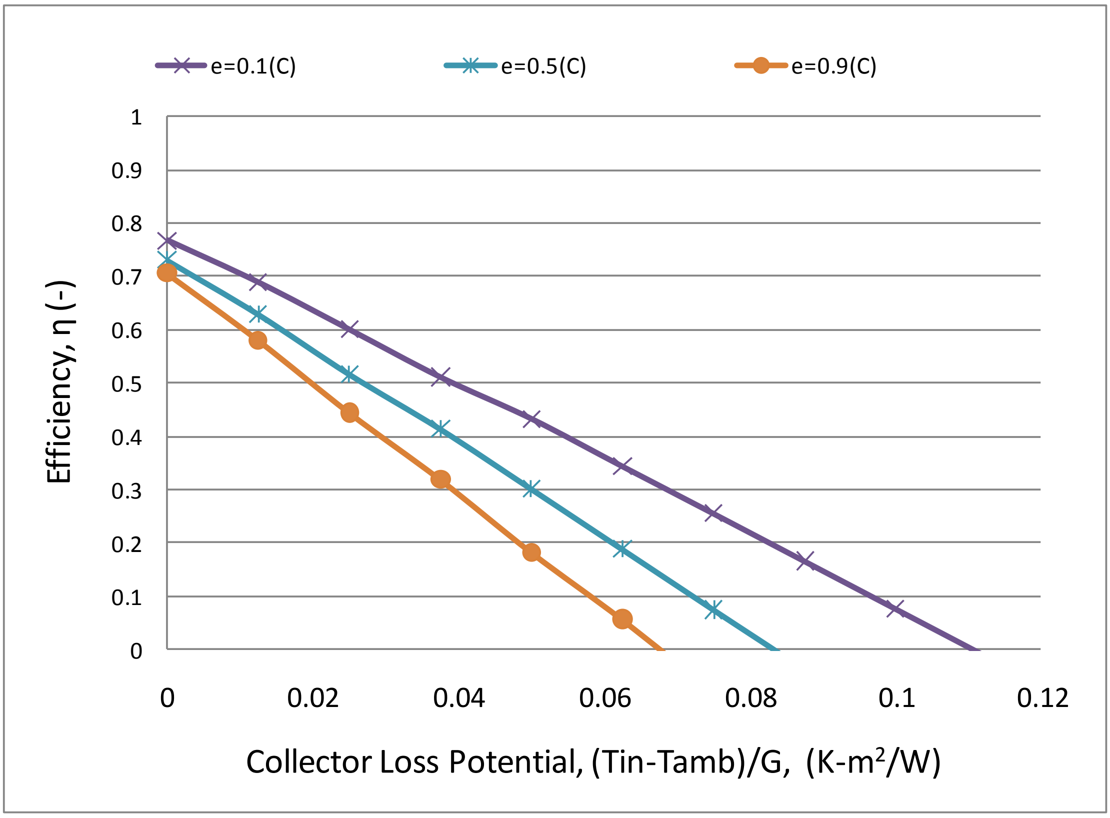

Figure 4.19: Total collector efficiency vs. ΔT/G at V_w=5m/s.

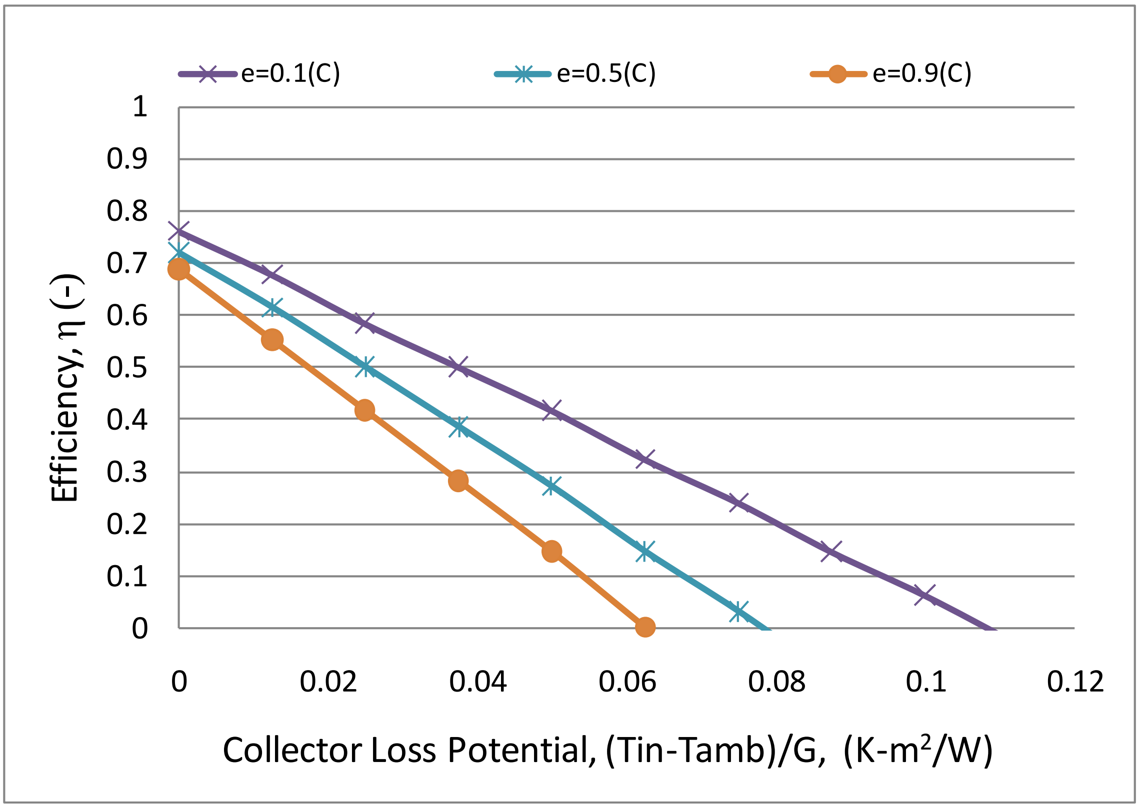

Figure 4.20: Collector water heating efficiency vs. ΔT/G at V_w=1m/s.

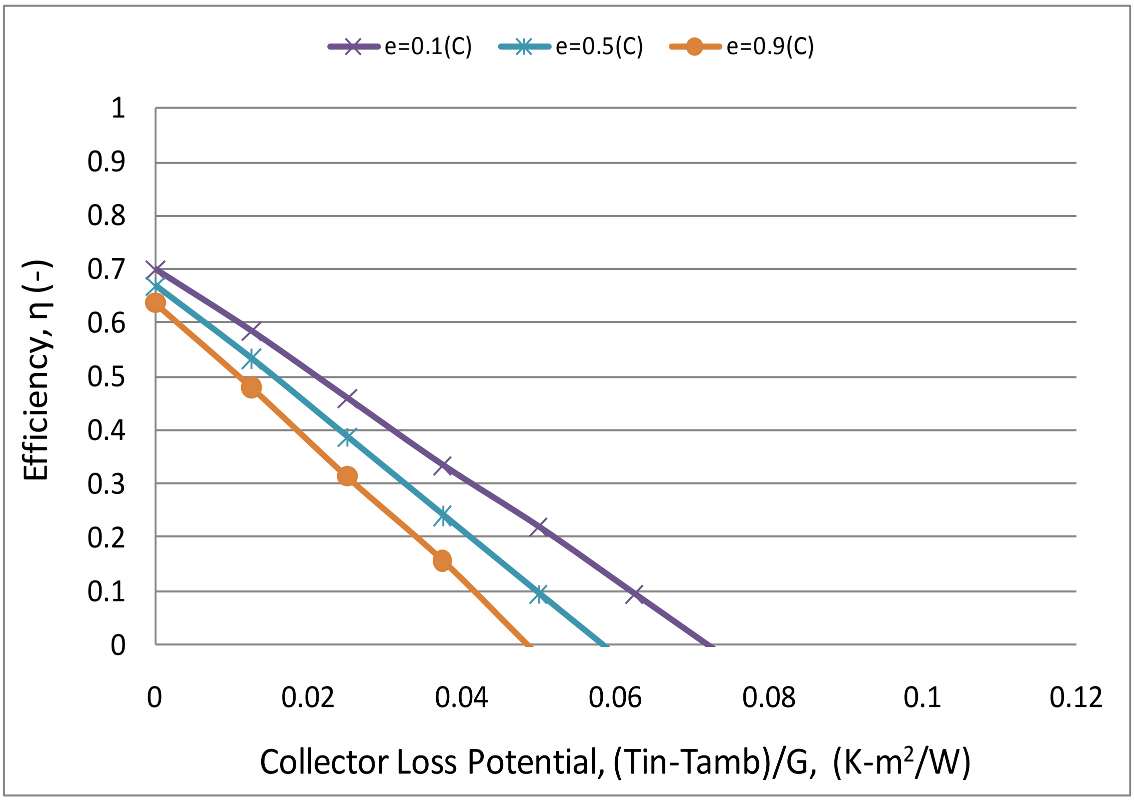

Figure 4.21: Collector water heating efficiency vs. ΔT/G at V_w=3m/s.

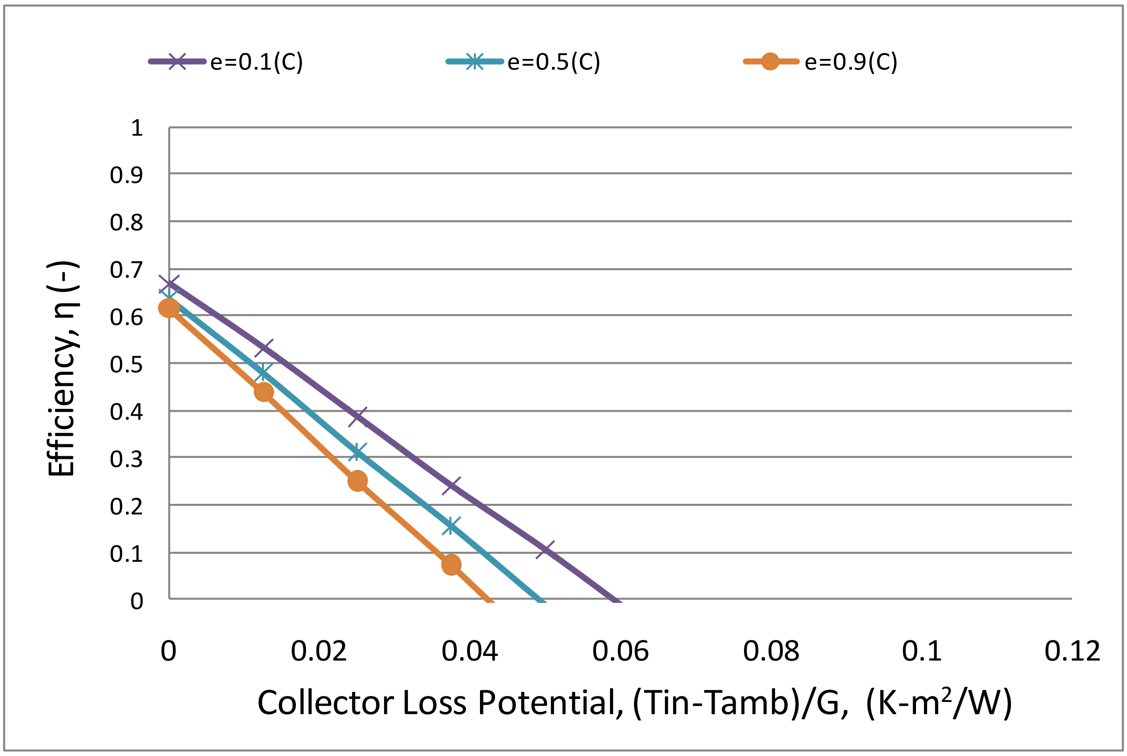

Figure 4.22: Collector water heating efficiency vs. ΔT/G at V_w=5m/s.

Finally a set of performance curves were obtained for wind speeds of 1m/s, 3m/s and 5m/s under varying solar radiation, G, inlet water temperature, T_{in}, and ambient temperature, T_{amb}. The values of solar radiation, inlet water temperature and ambient air temperature used as inputs to the model are given in Table 4.2. The performance curves for wind speeds of 1m/s, 3m/s and 5m/s are shown in Figure 4.23.

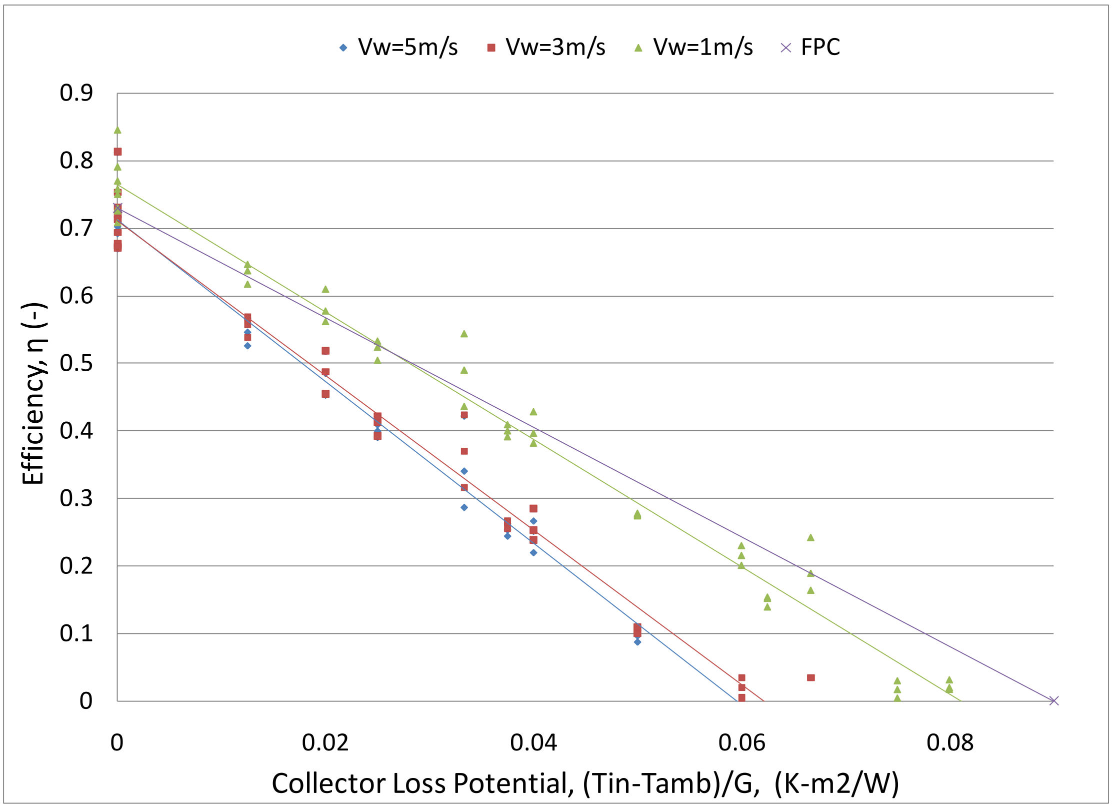

Figure 4.23: Total Collector efficiency vs. ΔT/G with emissivity=0.9.

4.3 Results

The results from the first sensitivity analysis show that the efficiency of the collector is highest when $R_{\dot{m}\mathrm{cp}}$ is between 0.5 and 0.6 for both the uncoupled and coupled air heating model. It also shows the general trend of increasing efficiency with increasing$(\dot{m}c_p)_{total}$. The existence of a maximum efficiency point at an intermediate ratio of air-to-total flow rate may be attributed to the fact that as the $R_{\dot{m}\mathrm{cp}}$ increases, the convective losses due to wind decrease, leading to an increase in the efficiency of the collector. However after a certain increase in $R_{\dot{m}\mathrm{cp}}$, further increase in the ratio has very little effect on the convective losses. Thus as the mass flow rate of water decreases, the plate temperature increases, leading to a rapid increase in the radiative losses and, consequently, a decrease in collector efficiency.

As expected the collector is more efficient overall when heating of air behind the plate is promoted rather than suppressed. However the efficiency difference is not large as seen in Figure 4.1 and Figure 4. 2**Error! Reference source not found.**. This means that if we design to suppress convective coupling behind the plate (e.g by using tiny louvers instead of holes), the collector can be accurately modeled using the uncoupled model. One reason to suppress convection behind the plate is to heat the water preferentially for the desiccant regeneration application.

The second sensitivity analysis shows the trend of decreasing efficiency of the collector for all three $R_{\dot{m}\mathrm{cp}}$ of 0.1, 0.5 and 0.9 as (T_i-T_{amb})/G is increased (Figures 4.5-7). One trend worth noticing is that as the $R_{\dot{m}\mathrm{cp}}$ is increased, the decrease in efficiency with increasing (T_i-T_{amb})/G is less steep. This can be attributed to the increased heat transfer to the air, which enters the collector at ambient temperature, with higher water inlet temperatures. The high flow rate of air through the collector prevents the plate from heating up too much, corresponding to low plate temperatures, which allows the collector to maintain a high efficiency at high inlet temperatures. This mode can be used in applications that can use more hot air than hot water.

The results from the third sensitivity analysis show that there is a general trend of decrease in the efficiency of the collector as ΔT/G is increased. The trend is highlighted by adding a line of best fit to the results obtained from the analysis. Furthermore it may be seen that when $R_{\dot{m}\mathrm{cp}}$ is low (Figure 4.8), the efficiency of the collector is very sensitive to the wind speed. This phenomenon may be explained by the fact that at a low $R_{\dot{m}\mathrm{cp}}$, the convective losses from the collector are weakly suppressed and thus an increase in the wind speed increases the convective losses considerably, hence decreasing the collector efficiency. It may be observed from

Figure 4.9 ($R_{\dot{m}\mathrm{cp}}$=0.5) that the LATSC behaves similar to a glazed collector. Thus the designer must be mindful of local wind conditions when applying the same generalization to lower air capacitance ratios.

From the last sensitivity analysis, it may be seen that there is a general, but small, reduction in the efficiency of the collector with increase in pitch and hole diameter. Thus the efficiency of the collector is mildly sensitive to changes in the pitch and diameter for low porosity absorber plates.

The performance curves obtained for the LATSC in the second batch of sensitivity analysis show that the single glazed collector only slightly outperforms the LATSC under light wind (1m/s) in terms of total thermal efficiency. This can be seen by observing Figure 4.23 which compares the performance of a LATSC under light wind (1m/s) and heavier wind (3m/s & 5m/s) with a plate absorber emissivity of 0.9 (non selective absorber) and a single glazed flat plate collector with a non selective absorber.

The second batch of sensitivity analysis shows the same general trends as those seen in the first batch.

CHAPTER 5

5 Experimental Validation of LATSC

To verify the model developed, an experiment was conducted to test the collector as close by as possible to the theoretical LATSC. A commercially available flat plate collector was procured and tested, followed by modification to a LATSC and subsequent testing of the hybrid collector. Thus a 2 m^2 flat plate, tube-fin type, collector was bought from SoleUAE.

The thermal testing of the collector requires accurate measurement of both the total solar energy incident and the total thermal energy gain of the collector. The solar energy incident can be measured by the use of pyranometers and accurate measurement of the collector absorber area. The thermal energy gain requires the measurement of the inlet and outlet temperatures of air and water as well as their respective flow rates. The total thermal energy gain of the collector is given by:

$$Q_{u,tot} = \left[\dot{m}C_p(T_{out} - T_{in})\ \right]_a + \left[\dot{m}C_p(T_{out} - T_{in})\ \right]_w \tag{54}$$

The specific heat capacity of water and air are calculated in EES using built in property data as a function of temperature and pressure.

The efficiency of the collector can then be calculated by:

$$\eta_c = \frac{Q_{u,tot}}{GA} \tag{55}$$

where G is the solar radiation and A is the collector area. The efficiency of the collector is defined as the ratio of the useful energy output in the heating of air and water to the total incident radiation on the collector surface.

5.1 Apparatus

5.1.1 Frame

A simple structure was constructed from angle iron bars to support the collector and to provide mounting areas for the pyranometers and logger box. In addition, the supporting bars to the rig could be adjusted in order to change the tilt of the collector.

5.1.2 Pyranometers

Two Licor LI-200 pyranometers, one on each side of the collector, were used in order to measure the solar radiation incident on the collector. The Licor pyranometers measure the radiation using a photodiode that measures incident energy of wavelengths in the band gap 400nm-700nm. The pyranometers also provide cosine loss correction and have a maximum error of +/-5%.

5.1.3 Flow meter

The water flow range required for the hybrid collector testing was 0.1-1.2 liters/min (corresponding to $\left(\dot{m}C_p\right)_{tot}$= 50W/m2-K and $R_{\dot{m}\mathrm{cp}}$=0.1-0.5) while the flow rate required for the flat plate collector testing was 2.72 l/min for which an accurate flow meter was required. Few flow meters were found that could accurately measure the flow rate in this range. The one finally procured (FTB 2004) was a low flow turbine wheel flow sensor from Omega Engineering. The flow meter was calibrated within the range 0.6l/min to 1.2 l/min and it was accurate to +/-5%. Another flow meter was calibrated for the flat plate collector testing and it too was accurate to +/-5%(See Appendix C).

An additional flow meter (FPR301) was obtained to measure lower flow rates. The flow rates measurable were from 0.27l/min-5l/min with a full scale error of 1%. The calibration certificate was provided by the manufacturer in which the multiplier varied linearly with flow rate.

5.1.4 Pressure transducer

A highly accurate differential pressure transducer (PX 657-2DI) was procured from Omega Engineering in order to measure the pressure drop across the orifice plates and flow nozzles. The pressure transducer was calibrated by the manufacturer to a full scale accuracy of +/-0.2%. The full scale range of measurement of the transducer was from 0-2 inH_2O.

5.1.5 Thermocouples

T-type 24 gauge, special limits, thermocouple wire with soldered junctions were used to measure the ambient and air side temperatures along the plate and at the exit. T-type grounded thermocouple (1/16” SS sheath) probes were used to measure the water inlet and outlet temperature. The thermocouple probes were installed with a counter-flow orientation with the flow of water in the pipe to enhance heat transfer and ensure a fast and accurate response to changes in temperature. The thermocouples installed in the water tank to monitor the stratification were T-type (24 gauge).

5.1.6 Orifice Plates and Air Flow Nozzles

Orifice plates and air flow nozzles were used to accurately measure the flow rate of air sucked through the collector. The advantages of orifice plates over nozzles are that they are relatively cheaper, and require a minimum Reynolds number of 5000 while air flow nozzles require a minimum Reynolds number of 10000. On the other hand, air flow nozzles allow for lower static pressure loss. As a result orifice plates were used for lower flow rates while the flow nozzles were used for higher flow rates. The orifice plates were manufactured locally adhering to ISO 5167 standards while the flow nozzles, of ASME long-radius type, were procured from Helander Metal Corporation. Two orifice plates were used with inner diameters of 30mm and 40mm while 2 flow nozzles were used with throat diameters of 25.4mm and 38.1mm. A flange assembly was also locally made for housing the orifice plates and nozzles and to provide a leak free connection to the pipe. For the calibration of the orifice plates and air flow nozzles, (see Appendix B).

5.1.7 Air Ducting and piping, flow conditioner

A flexible air duct was used to connect the collector air outlet with the fan. A 0.5m*8.5in*8.5in long square duct followed by a square to circular reducer and a 55mm(ID) PVC pipe were then used to connect the fan outlet to the flange assembly. A flow conditioner, Figure5.1, has also been installed at the start of the upstream pipe in order to promote the transition of the flow to laminar and smooth. The PVC pipe upstream of the flange assembly is 0.55m(10 pipe diameters) long while the pipe downstream is 0.275m(5 pipe diameters) long.

Figure5.1: Flow Conditioner

5.1.8 Fan

A variable speed fan (Series B Duct Blaster fan from Energy Conservatory) was used to provide the pumping power for air suction through the plate.

5.1.9 Water circulating pump

A low speed, low power pump was used for closed cycle circulation of water through the collector. The pump being used was a fixed speed pump and it could not be controlled using the logger. Therefore a manual needle valve was used to control the flow rate of water.

An additional pump was used to mix the water in the tank before tests to ensure a near constant temperature during the test. The flow rate of the pump was 90 l/min and the turnover rate for the 567(150 gal) tank was 6.7 minutes.

5.1.10 Anemometer

An ultra sonic, solid state, 2-axis anemometer (WindSonic^{TM}) from Gill Instruments was used to measure the wind speed. The instrument provides wind speed values with an accuracy of +/- 2%.

5.2 Instrumentation

5.2.1 Data Logger

The data logger used for the experiment was a CR1000 from Campbell Scientific. The data logger provides 8 differential voltage channels, 2 pulse channels as well as control and excitation ports to allow control of instruments. The data logger was programmed using Loggernet CRBasic compiler. The scan time for the data was 1 second while the average scanned data was recorded every 30 seconds. The data logger was powered by a 12V Dc power supply.

Efforts were made to ensure that all the electrically conducting parts of the setup (copper pipes, collector body) were grounded to the data logger ground lug.

5.2.2 Multiplexer

The number of thermocouples installedexceeded the differential channels available on the data logger requiring the use of a thermocouple multiplexer to provide additional channels. For this an AM25T Solid State Thermocouple Multiplexer from Campbell Scientific was used to connect all the thermocouples to the logger. The multiplexer was powered through the 12V power outlet port on the data logger and its isothermal terminal block sensor is accurate to +/-0.1K..

5.2.3 Real time monitoring

Real time monitoring was necessary to ensure that all the sensors were functioning normally during the individual tests and to monitor the air and water flow rates for any fluctuations from the desired flow rate of testing. A long serial cable with two short haul modems was used to transmit the data from the data logger to the workstation indoors. The baud rate of the logger was limited to 9600 due to the long serial cable.

5.3 Testing

5.3.1 Flat Plate Collector Testing

The flat plate collector testing was performed adhering to the ASHRAE 93 standards. A summary of the test conditions and parameters are given in Table 5.1.

Table 5.1: ASHRAE 93 suggested testing parameters

Parameter	Guideline	
Solar radiation	Min: 800W/m^2 ,	Max variation: +/-50W/m^2
Wind Speed	2-4m/s	
Water flow rate	0.02kg/sm^2 ,	Max variation:+/-1%
Inlet temperature	Variation +/- 0.1 K	

The collector was tested for standard performance indicators (i.e efficiency and incident angle modifier). The collector efficiency was measured at different values of $(T_{in}-T_{amb})/G$ which was controlled mainly by adjusting the inlet temperature. ASHRAE 93 recommends testing the collector with at least 4 different equally spaced inlet temperatures. The inlet temperatures that were used in the testing were: 30 ^{o}C, 45 ^{o}C, 60 ^{o}C and 70^{o}C. The inlet and outlet water temperatures, solar radiation, wind speed and water flow rate were recorded for these tests. The efficiency of the collector was calculated by using equations 1 and 2 where the air thermal component is zero. The standard plot for efficiency vs. (T_{in}-T_{amb})/G is shown in Figure5.2.

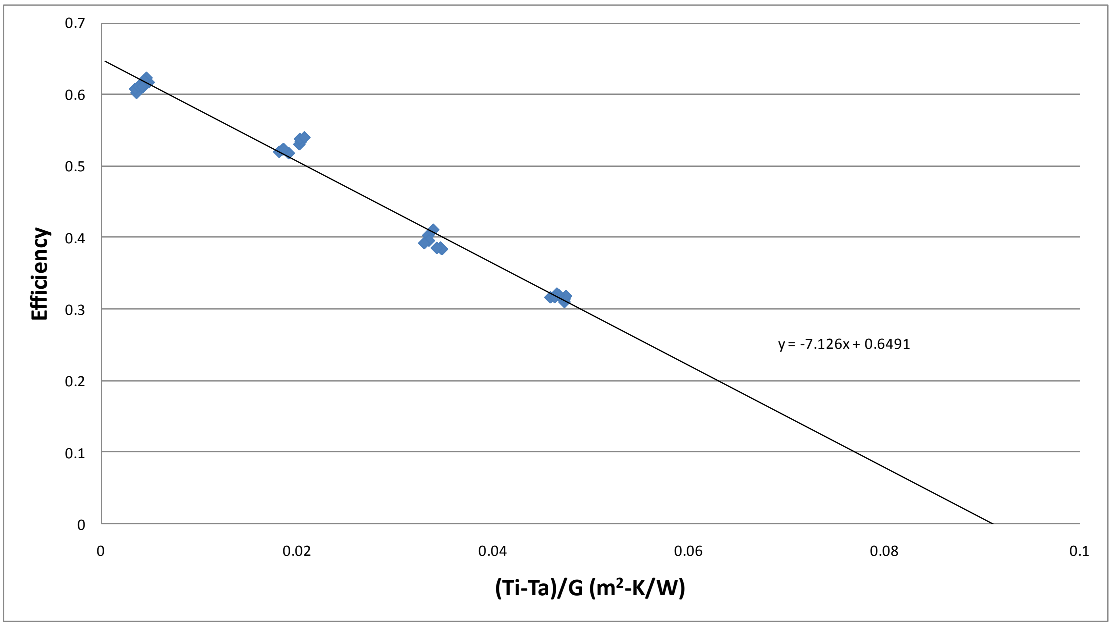

Figure5.2: Collector Efficiency vs Loss Potential (T_i-T_a)/G

The plot above displays the equation of the line of best fit for the test points. This equation is representative of:

$$\eta = F_R(\tau\alpha)_{avg} - F_R U_l \left(\frac{T_{in}-T_{amb}}{G}\right) \tag{56}$$

The glazing of the flat plate collector is made of low iron glass. Using the equation of the line of best fit, the values of F_R and U_l are calculated to be(See Appendix E**):**

F_R=<u>0.791</u>

U_l=<u>9.009 W/m^{2}K</u>

The incident angle modifier(IAM) test was performed on the flat plate collector to determine the effect of the change in the incident angle of the solar radiation on the performance of the collector. The glass cover on the collector has an absorptivity and transmissivity which depends on the incident angle and is the major cause of the degradation in efficiency at higher incident angles. In accordance with ASHRAE 93, the collector was tested at different times of the day when incident angles to the collector were 0, 30 ^{o}, 45^{o} and 60^{o}. Figure() shows the incidence angle modifier vs incidence angle relationship for the flat plate collector.

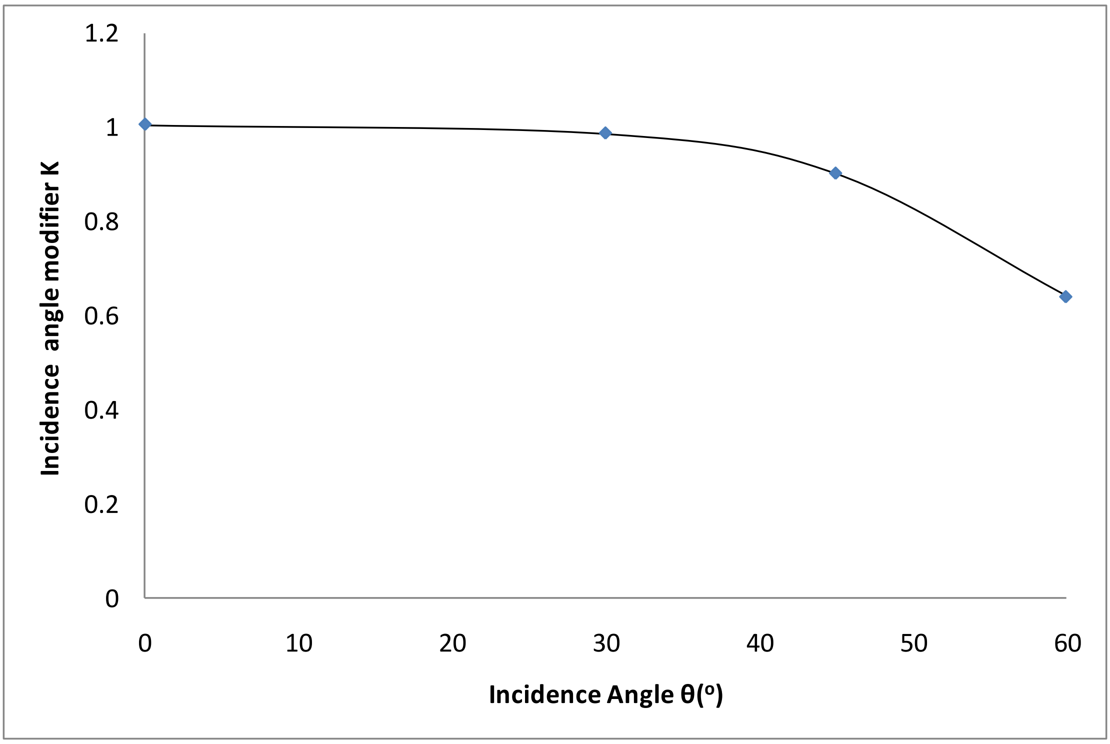

Figure5. 3: Incidence Angle Modifier vs Incidence Angle for Flat Plate Collector

5.3.2 LATSC Testing

Since ASHRAE 93 only has testing guidelines for either air collectors or water collectors, there was no set procedure to follow for testing the LATSC. Nonetheless a procedure was devised whereby the solar radiation and inlet water temperature guidelines were adhered to as in ASHRAE 93 for water collectors, while the water and air flow rates were decided according to the total thermal capacitance and air capacitance ratio. A total thermal capacitance of 25W/m^{2}K was used for the testing of the collector with air capacitance ratios from 0.1-0.5. Higher ratios could not be tested due to limitations of the water flow meter and the air fan. The experimental setup of the LATSC is shown in Figure5.4. The collector was tested at T_{in} close to ambient and also for a higher inlet temperature of about 60°C. The water was heated by a heating element in the tank and due to the large thermal capacity of the water in the tank, the water could not be heated to a higher temperature. Additionally, the collector was tested at different times of the day for the performance of the collector with changes in the incident angle.

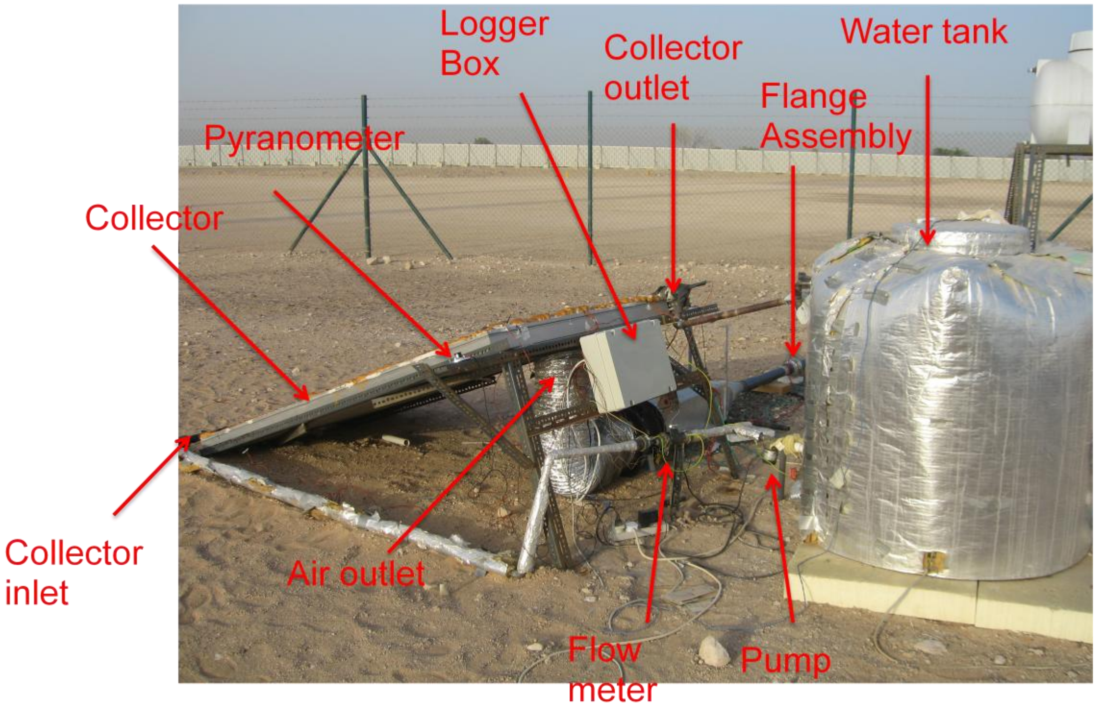

Figure5.4 :LATSC Experimental Setup

Using the ambient conditions and air and water temperatures and flow rate data measured from the experimental setup as input to the LATSC model, expected values for the efficiency of the collector have been obtained and compared with the empirical efficiency of the collector. The model and predicted efficiency of the collector are shown in Figure5.5.

Figure5.5: Predicted vs Experimental Efficiency

A line of best fit was drawn through the points which allow one to compare the modeled efficiency with the experimental efficiency. The data points that were used in the above plot are for wind speeds in the range of 3-4m/s. The LATSC experimental setup consistently has a lower efficiency than predicted by the model which amounts to about 19%. The slope of the line of best fit is slightly higher than unity.

However when additional points were added which were recorded at lower wind speeds (1-2 m/s), the difference between the modeled efficiency and the experimental efficiency decreased. This is shown by the increase in the slope of the line of best fit through the data points. At lower wind speeds, the starting length of the thermal boundary layer is smaller and therefore there is less an effect on the experimental efficiency due to the starting length.

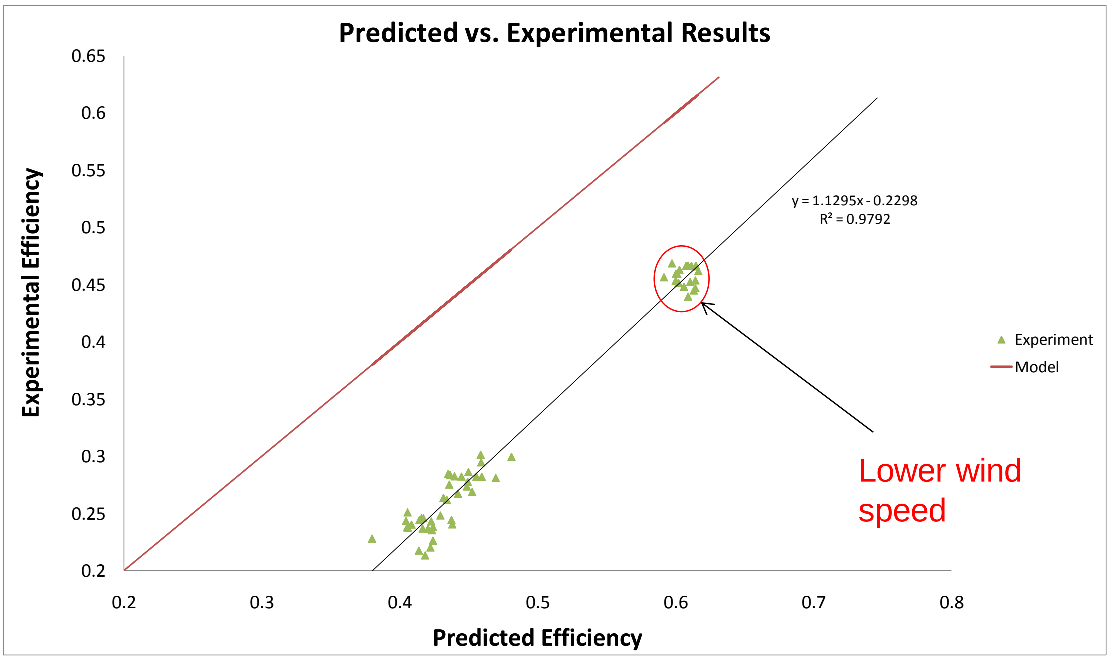

The performance of the LATSC was also measured at different incident angles of direct solar radiation. The testing procedure for the LATSC was identical to that for the flat plate collector. The method of computing the IAM was such that the efficiency of the LATSC was first calculated for the experimental results using equations (54&55). Then the theoretical efficiency of the collector was calculated for solar radiation incident normal to the collector using the numerical model developed in Chapter 3. The difference between the two efficiencies was then subtracted from 1 to give the absolute IAM of the collector for particular incidence angle to the model efficiency.

$$IAM_{abs} = 1 - (\eta_{th,n} - \eta_{exp}) \qquad (57)$$

The relative IAM was then obtained by normalizing the absolute deviation with the maximum absolute IAM. A sample calculation of the incidence angle modifier is shown in Table 5.2.

Note that the performance drop with θ is less for the LATSC than for the flat plate collector because the τα losses of the cover glass are not present.

Table 5.2: Method of Calculation of IAM

Model Efficiency($\eta_{th,n}$)	Experimental Efficiency(η_{exp})	Efficiency Difference($\Delta\eta$)	Absolute IAM= 1-$\Delta\eta$	Relative IAM= (1- $\Delta\eta$)/max(1-$\Delta\eta$)
0.093740962	0.374277	0.280536	0.719464	0.91465
0.093295903	0.396642	0.303346	0.696654	0.885652
0.094637698	0.393612	0.298975	0.701025	0.891209
0.104737912	0.373869	0.269131	0.730869	0.92915
0.118671215	0.369189	0.250518	0.749482	0.952812
0.253054316	0.466454	0.2134	0.7866	1

The IAM vs incidence angle relationship for the LATSC is shown in Figure5.6

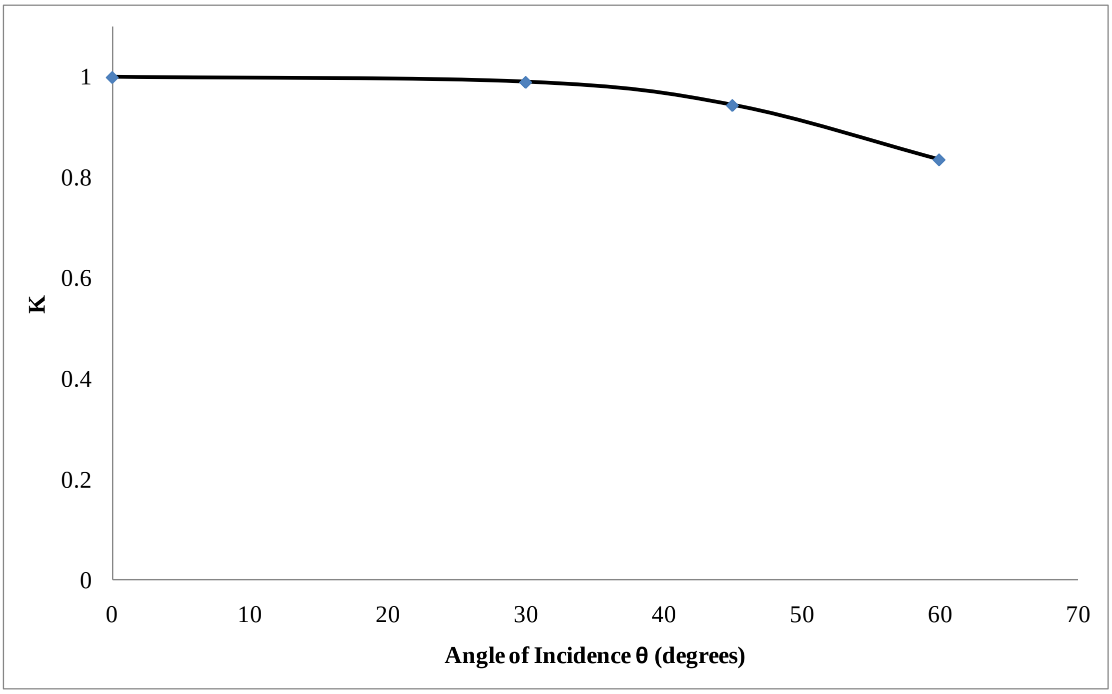

Figure5.6: Incidence Angle Modifier vs Incidence Angle for LATSC

The difference in the model and predicted efficiency is due to both inaccuracies in the measurement of data and the deviation of the actual collector from the assumptions made in the numerical model. The measurement system consists of all the sensors and the data acquisition system. Table 5.3 lists the errors associated with each of the measurement instruments.

Table 5.3: Instrument Uncertainty exclusive of installation error

Measurement Instrument	Make/Model #	Accuracy/ Error (%)
T-type thermocouple	Omega T-type 24 gauge	+/- (0.1^{o}C +0.5%)
Pressure transducer	Omega	+/-0.2% Full scale
Flow meter	Omega FPR 300	+/- 1% Full scale
Pyranometer	Licor LI-200	+/- 5%
Orifice Plates	30mm & 40mm inner diameter	+/- 5 %
Air Flow Nozzles	25.4mm &38.1 mm throat diameter	+/- 3%
2-D Wind Sensor	Gill WindSonic 2-Axis Ultrasonic Anemometer	+/- 2% (at 12m/s)

Table 5.4 lists the assumptions made in developing the numerical model and the actual conditions of the experimental setup.

All of the deviations of the actual model from the assumptions stated in the numerical model lead to adverse effects on the efficiency of the collector. The largest effect is probably that of the starting length of the boundary layer. The starting length is defined as the distance between the leading edge of the plate to the point on the plate where the boundary layer is fully developed. This is because the heat exchange effectiveness for air heating at the front of the collector and through the holes of the collector is only valid for the fully developed region of the thermal boundary layer on the plate surface and when the starting length is significant, the heat exchange effectiveness will be adversely affected.

Table 5.4: Differences between Model Assumptions and Experimental Realities

Model	Actual
Steady State	Transience mainly due to erratic wind speed
Uniform distribution of holes	Slightly non-uniform hole distribution with large gaps in between patches near tubes
Flat plate	Plate has waviness near top due to soldering faults
Negligible starting length for boundary layer	Large starting length depending on the wind speed and air suction velocity. For some cases up to full collector length in starting region.
Uniform parallel flow of air behind absorber plate	Non uniform flow with streamlines crossing due to pressure drop in across plenum
No leakage in collector shell	Finite leakage in setup (see Appendix C)
Uniform absorptivity of collector plate surface across the solar spectrum.	Non uniform deposition of paint on the absorber plate and specular reflectance of absorber plate.

The starting length is given by(C. F. Kutscher, et al., 1993):

$$L_s \approx \frac{V_w \nu_a}{V_s{}^2} \tag{58}$$

The effect of wind speed and suction velocity on the starting length is given in Table 5.5. For this calculation the fluid properties are evaluated at an ambient temperature of 25^{o}C.

Table 5.5: Starting lengths in meters for different wind speeds and suction velocity

	Wind Speed (m/s)		
Suction velocity(m/s)	**1**	**3**	**5**
0.0189 ($\dot{m}_a c_{pa}$=45)	0.0321	0.09363	0.1561
0.006303 ($\dot{m}_a c_{pa}$=15)	0.2809	0.8427	1.404
0.0012606 ($\dot{m}_a c_{pa}$=3)	7.022	21.07	35.11

As can be seen in Table 5.5, the starting lengths vary from 0.0321m (3% of collector width) for low wind speed and high suction velocity to 35.11m (3511% of collector width) for high wind speed and low suction velocity. It is worth observing that the starting length is a stronger function of suction velocity than the wind speed.

Most of the data points that have been obtained have starting lengths that cover almost the whole collector width. Thus the heat exchange effectiveness which has been used to predict the heat transferred to the air in the numerical model is optimistic based on the assumption that the starting length of the collector is negligible. Similarly the wind loss coefficient is also underestimated for large starting lengths as Kutscher's derivation assumes the boundary layer will be fully developed at the end of the plate and therefore the convective loss from the plate will be equal to the net energy transferred to the boundary layer in the starting length. Therefore the large discrepancy seen between the experimental and numerical results can be attributed mainly to the large starting lengths when testing the collector. These errors could be reduced by using a larger collector and/or by testing in light wind conditions.

Another cause for discrepancy in the numerical model and experiment is the waviness of the absorber plate, which leads to much higher wind losses (Keith M. Gawlik & Kutscher, 2002).

CHAPTER 6

6 Liquid Desiccant Regenerator Model

A liquid desiccant regenerator (LDR) model was developed to test the performance of the LATSC for one of its potential applications. For this purpose a simplified yet moderately accurate model was built with the following assumptions:

1. Steady state operation of the LDR
2. Enthalpy of dilution neglected due to a very small amount of water added/reduced from each control volume (W. Kessling, Laevemann, & Kapfhammer, 1998).
3. Laminar, non wavy, fully wetted flow of liquid desiccant over parallel plate
4. Constant properties of air, water and desiccant in a control volume
5. Fully mixed desiccant film(no thermal gradient, no concentration gradient in x-direction)

The aim of the simplified LDR model was to allow for the integration of the LATSC with a LDR and determine an optimum total thermal capacitance rate, $(\dot{m}C_p)_{tot}$ and ratio, $R_{\dot{m}C_p}$ for a given $\dot{m}_d$. This would allow for the merits of the LATSC to be assessed for liquid desiccant regeneration applications leading to a feasibility study to compare the performance of the LATSC with flat plate collectors.

There are three main types of LDRs currently being used in the industry. These are the spray cooled type, packed bed type and falling film type. Details of the advantages and disadvantages of each are mentioned in Chapter 2 (literature review). The three differ mainly in mode of air to desiccant contact. The falling film type model was developed as it has the potential to operate with close approach temperatures and high thermodynamic efficiencies. It also allows for internal heating of the desiccant by hot water and simultaneous regeneration of the desiccant by contact with hot air, providing the opportunity for the use of both heated air and water from the LATSC. The schematic of the LDR model is shown in Figure 6.1.

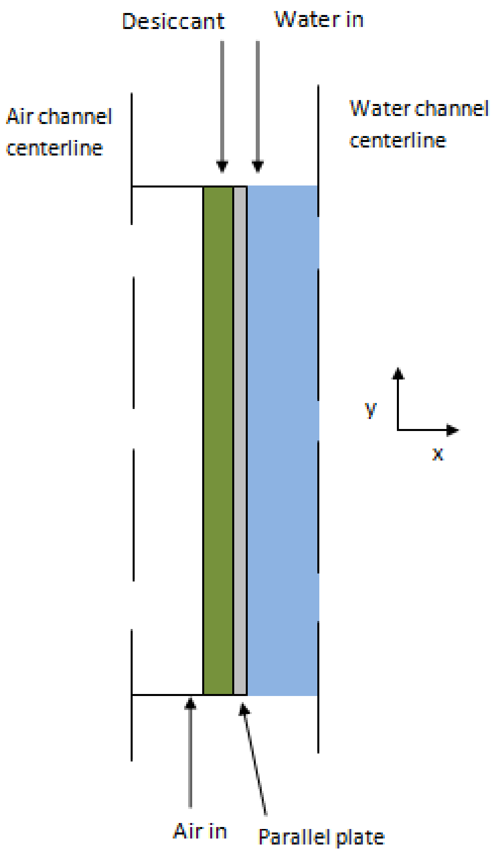

Figure 6.1: Side Cross-sectional View of the LDR

The regenerator consists of many parallel plates which contain internal channels through which the hot water flows from top to bottom. Desiccant is sprayed uniformly at the top of the regenerator plate and it flows down the air side of the plate as a thin film. Air is injected from the bottom and it moves towards the top giving the LDR a counter flow configuration. There exists a plane of symmetry at the center of each air-side and water-side channel about which symmetry of physical properties and chemical composition of the water, air and desiccant are encountered in the negative and positive x-direction. Therefore only one side of the line of symmetry is evaluated while performing the thermal and chemical analysis on the LDR.

A heat and mass balance is first performed on a control volume of the regenerator shown in Figure 6.2.

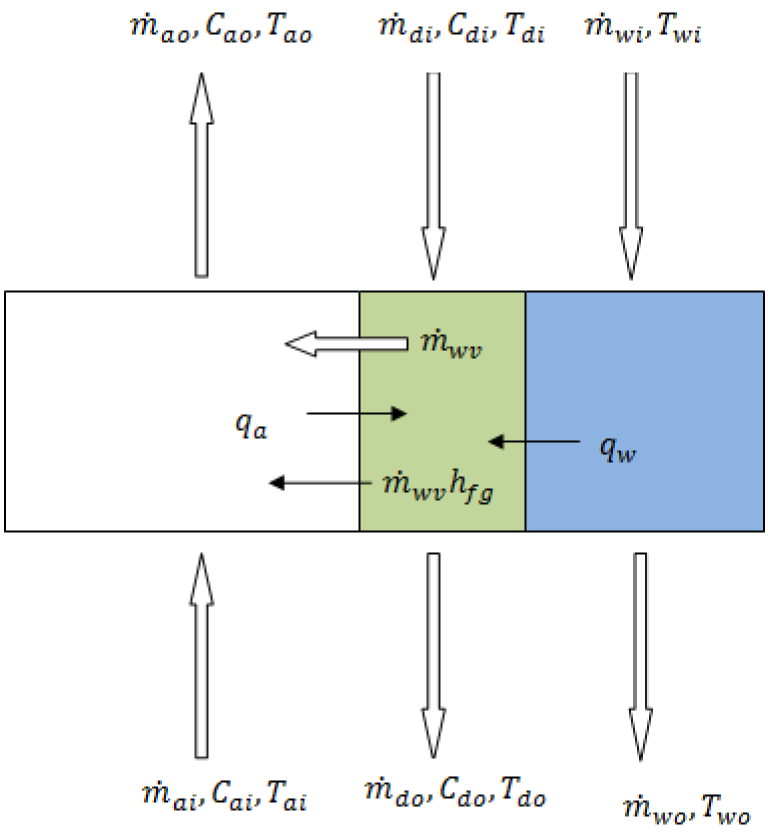

Figure 6.2: Heat and Mass balance on a differential element of the LDR.

The three mass balance equations obtained are:

for the air: $\dot{m}_{ao} = \dot{m}_{ai} + \dot{m}_{wv}$ (59)

for the desiccant: $\dot{m}_{do} = \dot{m}_{di} - \dot{m}_{wv}$ (60)

and for the water: $\dot{m}_{wo} = \dot{m}_{wi}$ (61)

where the mass of air is composed of dry air and moisture:

$$\dot{m}_a = \dot{m}_{da} + \dot{m}_{da}\omega \quad (61)$$

Similarly the desiccant solution contains desiccant salt and water:

$$\dot{m}_d = \dot{m}_{ds} + \dot{m}_{wd} \quad (63)$$

The concentrations of water in air and in the desiccant can also be obtained.

The air humidity is: $C_{ao} = \frac{C_{ai}\dot{m}_{ai} + \dot{m}_{wv}}{\dot{m}_{ao}}$ (64)

and the desiccant concentration is: $C_{do} = \frac{C_{di}\dot{m}_{di} - \dot{m}_{wv}}{\dot{m}_{do}}$ (65)

Next the energy balances are given for the air, water and desiccant elements.

$$\dot{m}_{da,o}c_{pdao}T_{ao} + \left(\dot{m}_{da,i}\omega + \dot{m}_{wv}\right)c_{pwv}T_{ao} = \dot{m}_{dai}\left(c_{pda,i} + \omega c_{pwv}\right)T_{ai} - q_a + \dot{m}_{wv}c_{pwv}T_{di} \qquad (66)$$

Equation (66) says that the airstream enthalpy out of the regenerator equals the airstream enthalpy in, plus the enthalpy of vapor form the desiccant, minus heat transferred to the desiccant stream.

$$\dot{m}_{do}c_{pdo}T_{do} = \dot{m}_{di}c_{pdi}T_{di} + q_a + q_w - \dot{m}_{wv}h_{fg} \qquad (67)$$

Equation (67) says that the change in the desiccant solution enthalpy is proportional to the sum of heat gains from the air and water, minus the enthalpy of evaporation of the moisture rejected to the airstream.

$$\dot{m}_{wo}c_{pwo}T_{wo} = \dot{m}_{wi}c_{pwo}T_{wo} - q_w \qquad (68)$$

Equation (68) says that the change in water temperatures is proportional to the heat transferred to the desiccant stream.

The correlation for heat transfer from air to the desiccant was developed by assuming a laminar, fully developed flow of air between the two parallel plates. The temperature of the plate at each element was assumed constant for which the Nusselt number (Nu_a) is 7.54(Incropera, et al., 2006).

Similarly in the case of the heat transfer from the water to the desiccant it was assumed that the water flow in the channel in the plate was fully developed and laminar while the temperature of the plate at each element was assumed constant. The Nusselt number for the heat transfer from the water to the desiccant (Nu_w) is also 7.54 (Incropera, et al., 2006).

Convection rates at the air-desiccant interface, q_a, and water-desiccant interface, q_w, are given by:

$$q_a = h_a(T_{ai} - T_{di})Wdy \tag{69}$$

where

$$h_a = \frac{Nu_a k_a}{D_{h,a}} \tag{70}$$

and

$$q_w = h_w(T_{wi} - T_{di})Wdy \tag{71}$$

where

$$h_w = \frac{Nu_w k_a}{D_{h,w}} \tag{72}$$

Where the $D_{h,a}$ $D_{h,w}$ are the hydraulic diameters of the channels through which the air and water flow.

The mass transfer coefficient for water vapor transfer to the air stream can be estimated using the Chilton-Colburn analogy:

$$h_m = \frac{h_a}{\rho_a c_{pa}}\left(\frac{\alpha_a}{D_{a,wv}}\right)^{-2/3} \tag{73}$$

The water vapor mass transfer for each element can then be determined:

$$\dot{m}_{wv} = h_m \rho_a (C_{int} - C_{ai}) \tag{74}$$

C_{int} is the equilibrium water vapor concentration at the air-desiccant interface while C_{ai} is the water vapor pressure in the inlet air. The desiccant used for the regenerator analysis is lithium chloride and the properties of the desiccant-water solution are given by Conde (2004). The properties of air and air-water mixtures built in to EES are based on thermodynamic data developed by Hyland & Wexler (1983) and reported in handbooks such as ASHRAE (2009).

6.1 Solving procedure

The counter-flow configuration of the LDR means that the temperatures of all nodes must be solved simultaneously. Therefore the approach used was to split the regeneration process in to two cycles (A&B). In cycle A, the inlet air temperature and concentration for each node were kept constant at the inlet properties of the air while the water and desiccant temperatures and concentrations were solved for each node. These values were then saved, plugged in to the nodes of cycle B, and kept constant while the air temperatures and concentrations were calculated for each node. This procedure was repeated until the water vapor transferred to the air at each node was equal in both cycles. Figure 6.3 presents the flow chart of the solver.

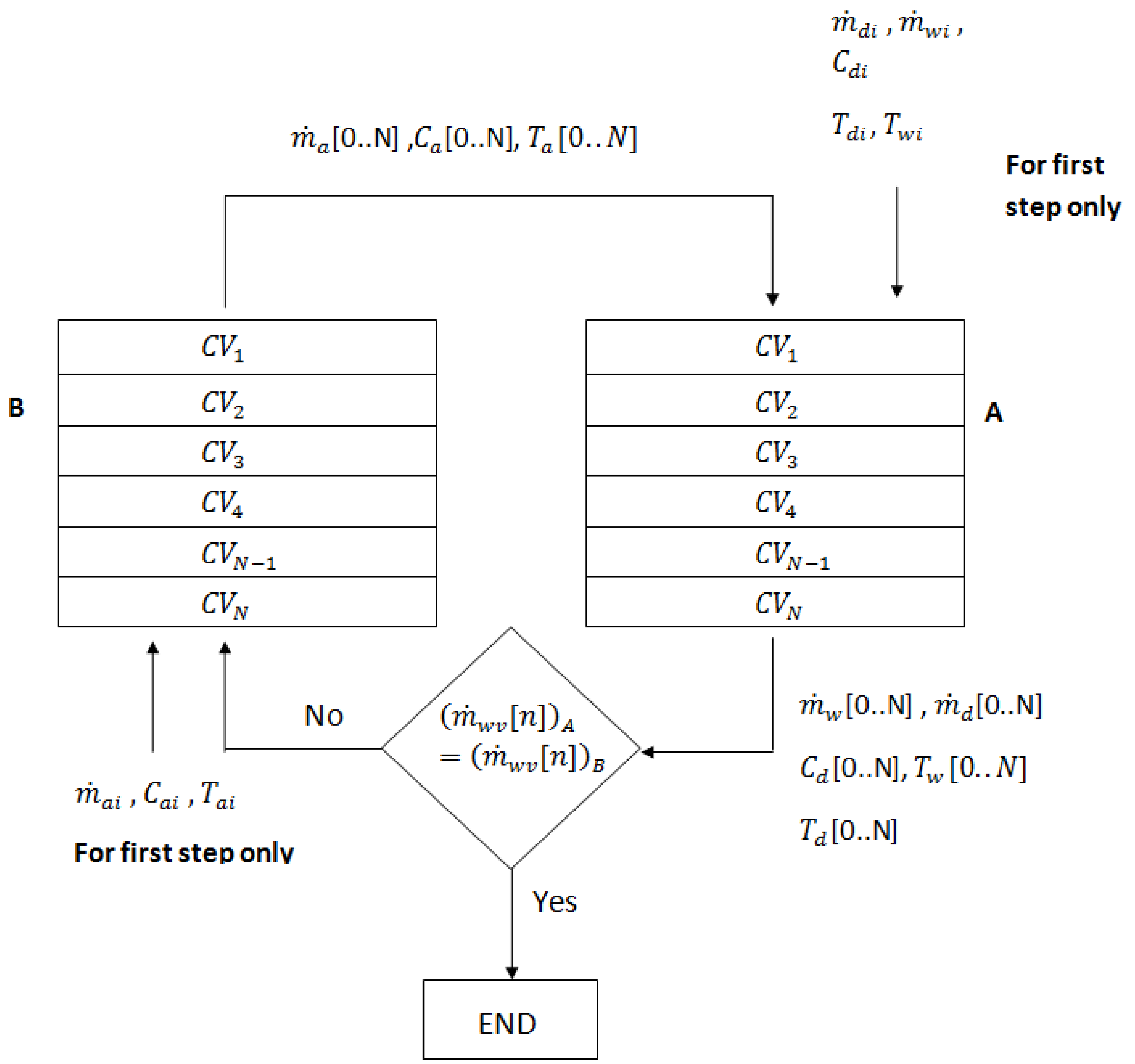

Figure 6.3: Flow chart of solving procedure for LDR

6.2 Combined Model

The model described above was combined with the LATSC model and simulated using Engineering Equation Solver (EES) to obtain the overall system efficiency ($\eta_{overall}$) for varying $(\dot{m}c_p)_{total}$ and $R_{\dot{m}\mathrm{cp}}$. The overall system efficiency is:

$$\eta_{overall} = \eta_c \eta_{reg} \tag{75}$$

where

$$\eta_{reg} = \frac{\dot{m}_{da} h_{fg} (\omega_{ao} - \omega_{ai})}{\dot{m}_a C_{pa} (T_{ao} - T_{ai}) + \dot{m}_w C_{pw} (T_{wo} - T_{wi})} \tag{76}$$

η_c has previously been defined by equation (55). The regeneration efficiency is the ratio of the energy used to evaporate water from the desiccant solution to the total energy provided by the LATSC. The overall system efficiency is the ratio of the energy used to evaporate the water from the desiccant solution to the incident solar radiation on the collector surface. It can also be expressed as the product of the regeneration efficiency and the collector efficiency.

The schematic of the coupled model is illustrated in Figure 6.4.

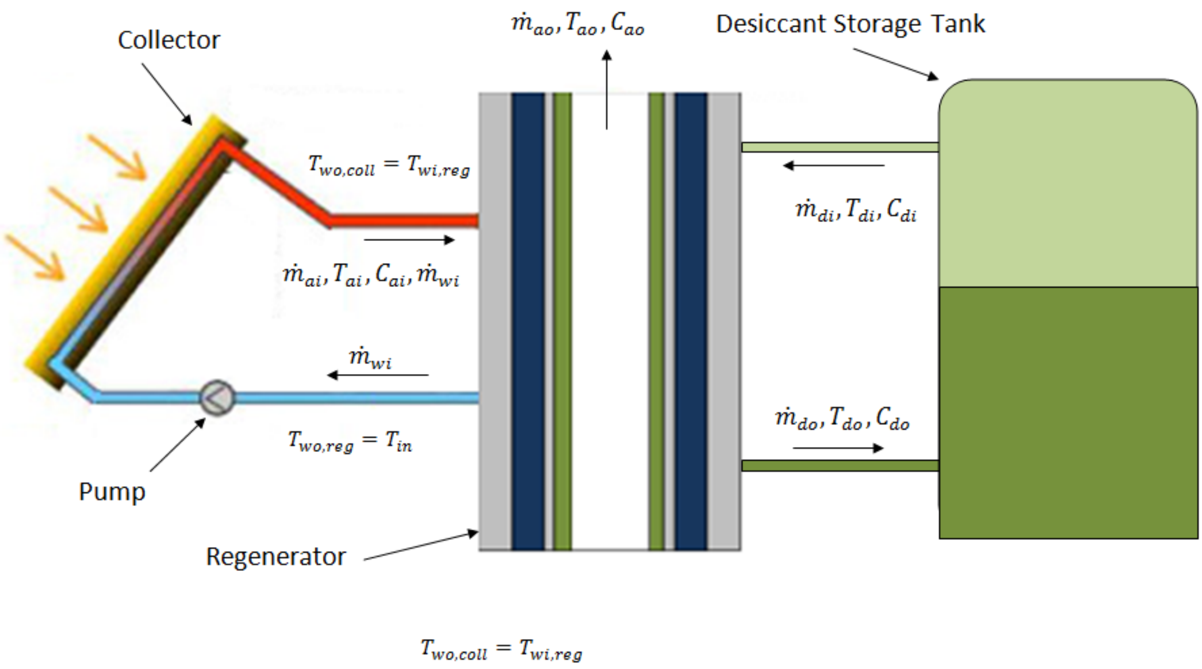

Figure 6.4: Schematic of LATSC coupled with LDR and an ideal stratified storage tank.

There are separate loops for the flow of water, desiccant and air in the coupled system. The water and desiccant salt flow in a closed loop while the air and the moisture in the desiccant flow in an open loop. Assuming steady state operation of the coupled system, the water is initially pumped to the collector at a constant mass flow rate $\dot{m}_w$ and temperature T_{in} where it is heated in the collector to T_{wo}. The water then enters the regenerator at T_{wo} and exits at T_{in} and thus a cycle is completed. Note that the system is operated in such a way that the exiting water from the regenerator is fed directly in to the collector. The air enters the collector at a constant mass flow rate $\dot{m}_a$ and temperature of T_{amb} and exits at a temperature of T_{ao} with no change in mass flow rate. Air then moves in to the regenerator with the same temperature and flow rate as at the collector outlet. The air gains mass in the regenerator due to the evaporation of the water from the desiccant stream in to the air, after which it leaves the regenerator with a mass flow rate of $\dot{m}_{ao}$ and temperature of $T_{ao,reg}$. The desiccant solution is pumped from the top of a stratified tank in to the regenerator with a concentration of C_{di}, temperature T_{di} and mass flow rate $\dot{m}_{di}$. The desiccant solution loses mass in the regenerator as the water evaporates in to the air stream leading to an exiting mass flow rate $\dot{m}_{do}$, temperature T_{do} and concentration C_{do}.

To account for the dependence of the collector and regenerator outlet temperatures on the respective water inlet temperatures, the coupled model can be solved iteratively. The solving procedure for the coupled model is shown in Figure 6.5.

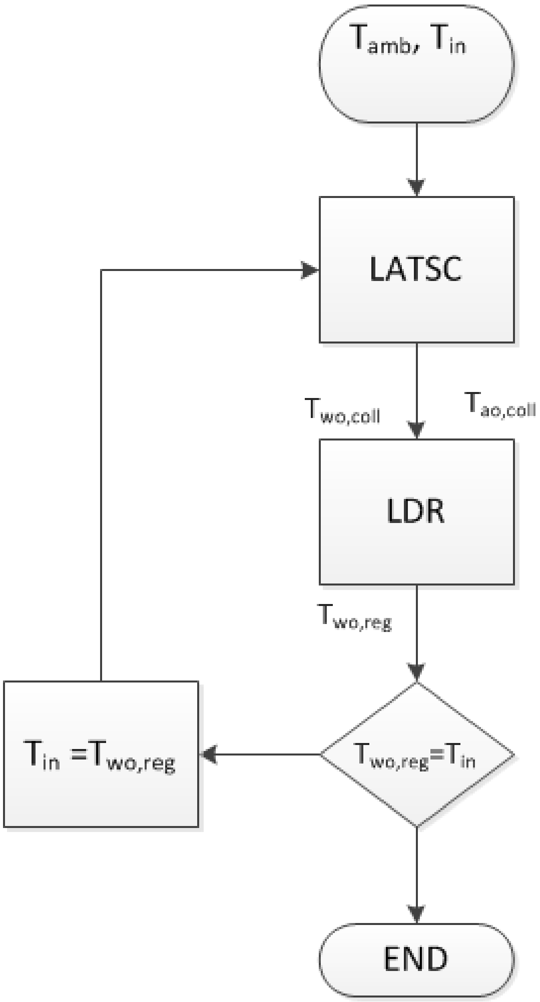

Figure 6.5: Flow chart for the LATSC-LDR coupled model.

The physical dimensions and inlet conditions of the regenerator are summarized in Table 6.1.

Table 6.1: Parameters and Inlet Conditions of the Regenerator

Parameter	Value
Plate height	0.5 m
Plate width	0.5 m
Plate spacing	0.005 m
Desiccant flow rate	0.0013 kg/s
Inlet desiccant concentration	0.2
Control volume height	0.001m
Number of control volumes	500

6.3.1 Results

The $(\dot{m}c_p)_{total}$ of the total system was varied form 5W/m^{2}K to 25W/m^{2}K at five equal intervals. For each $(\dot{m}c_p)_{total}$, $R_{\dot{m}\text{cp}}$ was varied from 0.2 to 0.9 at intervals of 0.1. The properties of the water, air and desiccant were determined at each node using the EES built in property functions. The collector properties that have been kept constant are listed in Table 4. 1. The desiccant mass flow rate was also kept constant at 0.000653 kg/s. Figures 6.6-8 show the variation of the collector, regenerator and overall efficiency with $R_{\dot{m}\text{cp}}$ for different $(\dot{m}c_p)_{total}$ for the coupled system.

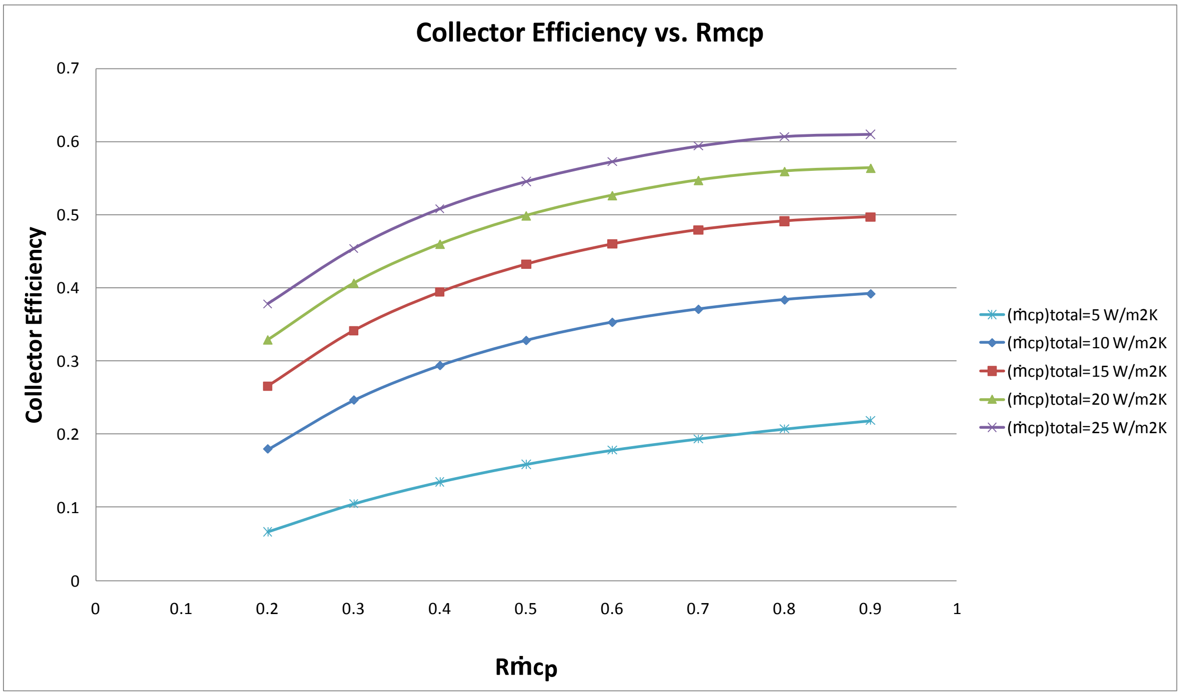

Figure 6. 6: Collector Efficiency vs $R_{\dot{m}\mathrm{cp}}$ for coupled system.

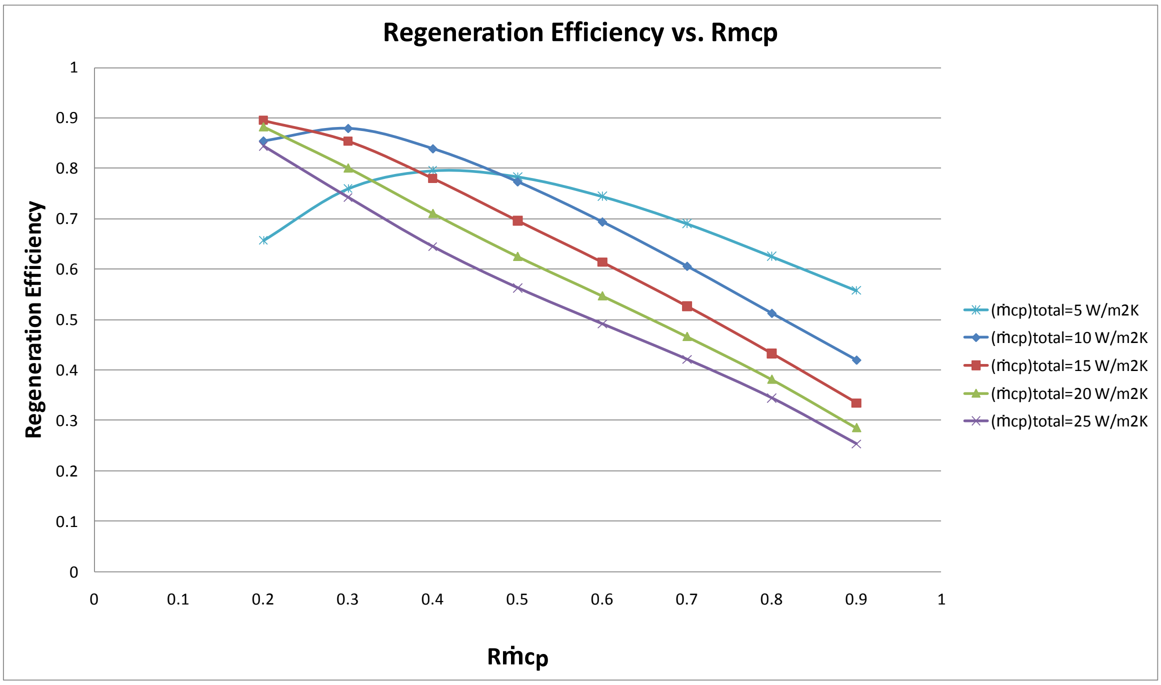

Figure 6. 7: Regeneration Efficiency vs $R_{\dot{m}\mathrm{cp}}$ for coupled system.

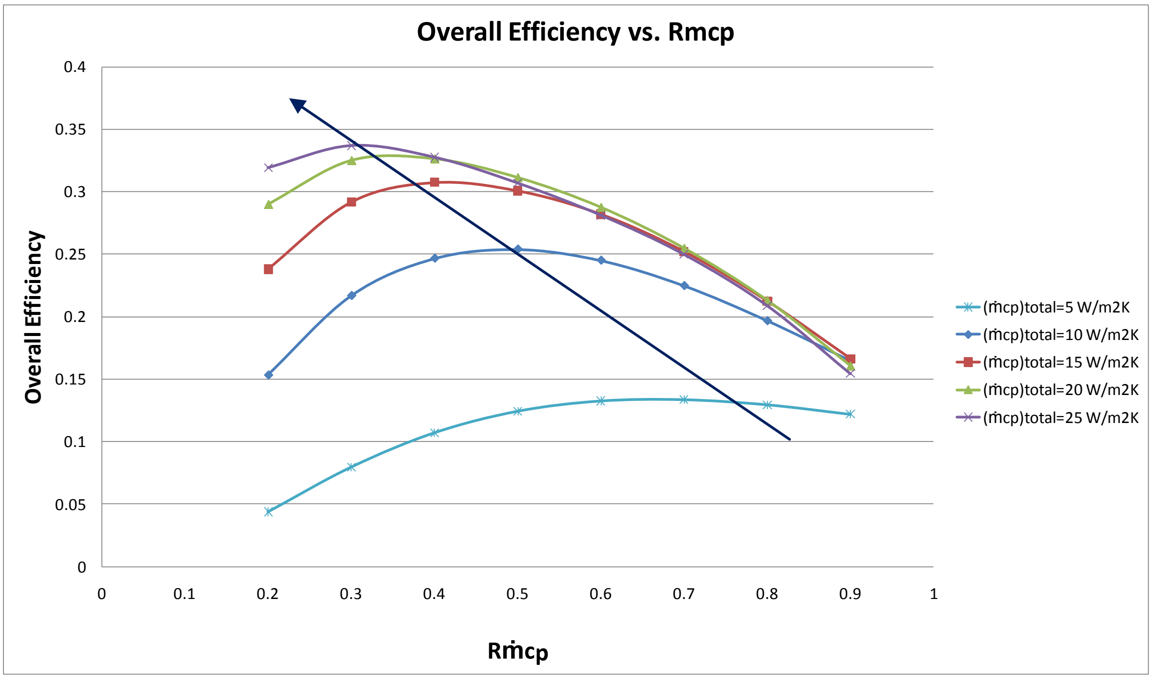

Figure 6. 8: Overall Efficiency vs $R_{\dot{m}\mathrm{cp}}$ for coupled system.

The collector efficiency tends to increase as $R_{\dot{m}cp}$ is increased from 0.2-0.9 at a constant $(\dot{m}c_p)_{total}$. This is due to the large temperature drop for water across the regenerator when $R_{\dot{m}\mathrm{cp}}$ is increased, ($(\dot{m}c_p)_w$ decreases), leading to a lower inlet water temperature supplied to the collector. On the other hand the regenerator efficiency tends to decrease with an increase in $R_{\dot{m}\mathrm{cp}}$. This is because higher water flow rates maintain a constant high temperature in the internally heated regenerator, leading to higher regeneration efficiencies. It should be noted that while the temperature of the inlet water to the regenerator is higher at higher Rmcps, that temperature cannot be sustained for long in the regenerator due to the constant heat transfer to the desiccant for regeneration. The variation of the collector water outlet temperature or regenerator water inlet temperature with $R_{\dot{m}\mathrm{cp}}$ at a different $(\dot{m}c_p)_{total}$ is shown in Figure 6.9.

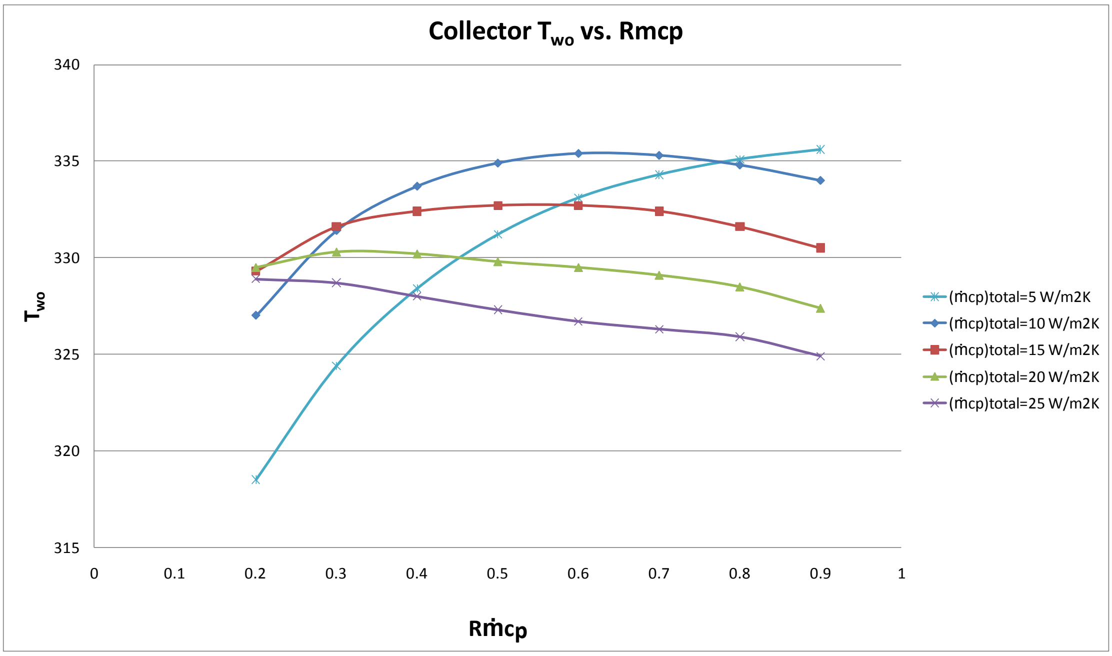

Figure 6.9: Collector water outlet/Regenerator water inlet temperature vs $R_{\dot{m}\mathrm{cp}}$.

The desiccant regeneration rate and efficiency strongly depend on the temperature of the desiccant at the air-desiccant interface. This temperature needs to be maintained by constant heat transfer from the hot water and air to the desiccant. Most of the heat transfer to the desiccant is from the water due to the higher thermal conductivity of water. Thus to increase the regeneration rate, the water that is supplied to the regenerator must have a high temperature and thermal capacitance rate. This can explain the decrease in regeneration efficiency when $R_{\dot{m}\mathrm{cp}}$ is low for the very low $(\dot{m}c_p)_{total}$ of 5W/m^{2}K. It can be observed that even though the thermal capacitance rate of the water increases with a decrease in $R_{\dot{m}\mathrm{cp}}$, the temperature of water supplied decreases rapidly due to convection losses at the front of the collector, leading to a drop in the regeneration efficiency.

The overall efficiency is seen to increase with an increase in $R_{\dot{m}\mathrm{cp}}$ and reach a maximum after which it tends to decrease. The maximum overall efficiency is achieved at different $R_{\dot{m}\mathrm{cp}}$ for different $(\dot{m}c_p)_{total}$. As $(\dot{m}c_p)_{total}$ increases, the $R_{\dot{m}\mathrm{cp}}$ at which the maximum efficiency is observed decreases. This interaction is highlighted by the arrow in Figure 6. 8. The trend observed can be explained by the preference of the regenerator for hot water over hot air and of the collector for an air suction rate just enough to suppress the majority of the convective losses so that the collector operates at a reasonable efficiency.

CHAPTER 7

7 Optimization of Combined LATSC and LDR Model

In the sensitivity analysis shown in Chpater 6, only 2 parameters ($\dot{m}_{cpa}$ and $\dot{m}_{cpw}$) were varied to assess the sensitivity of the system to changes in these parameters. In practical applications, there are many more parameters that can be varied to optimize the system for different weather conditions. In this section the combined LATSC and LDR system is optimized according to typical weather conditions in Abu Dhabi.

Typical weather conditions were determined by assessing the weather data for one year in Abu Dhabi. The weather conditions that affect the performance of the combined collector-regenerator system are solar radiation, ambient temperature, wind speed and humidity. To determine these values for a typical Abu Dhabi day, TMY2(2005)(Remund, Lang, & Kunz, 2003) data for Abu Dhabi were plotted on a histogram for each of the parameters with different equally sized bins depending on the variability of a particular parameter. For example solar radiation varies for most parts of the day between 300W/m^2 to over 1000W/m^2 while wind speed tends to range between 0 and 5 m/s. The range of values of the parameters and the bin sizes for the parameters are shown in Table 7.1:

Table 7.1: Range and bin sizes of weather parameters used in optimization

Parameter	Range	Bin size
Solar Radiation	300-1000W/m^2	100W/m^2
Wind Speed	0-5m/s	1m/s
Humidity	0.01-0.035 kg$_w$/kg$_{da}$	0.005 kg$_w$/kg$_{da}$
Ambient temperature	15-45^{o}C	5^{o}C

The range of values taken for solar radiation to plot the histogram starts with a critical radiation of 300W/m^2. Lower levels of radiation are of no use for the system as there will be very little energy gain by the collector and the regeneration of the desiccant will not be possible. The solar radiation plotted is the incident solar radiation on a tilted surface with slope 24.43^o(latitude of Abu Dhabi) The histograms for solar radiation, wind speed, humidity and ambient temperature are shown in Figures 7.1-7.4.

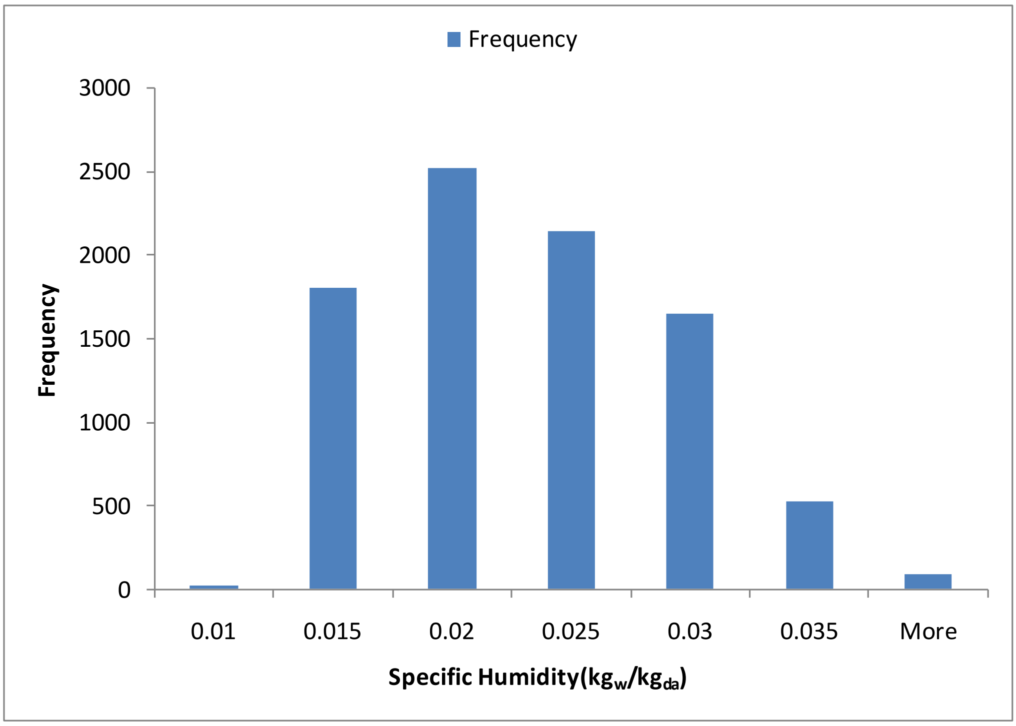

Figure 7. 1: Histogram showing the frequency of occurrence of specific humidity during the year in Abu Dhabi

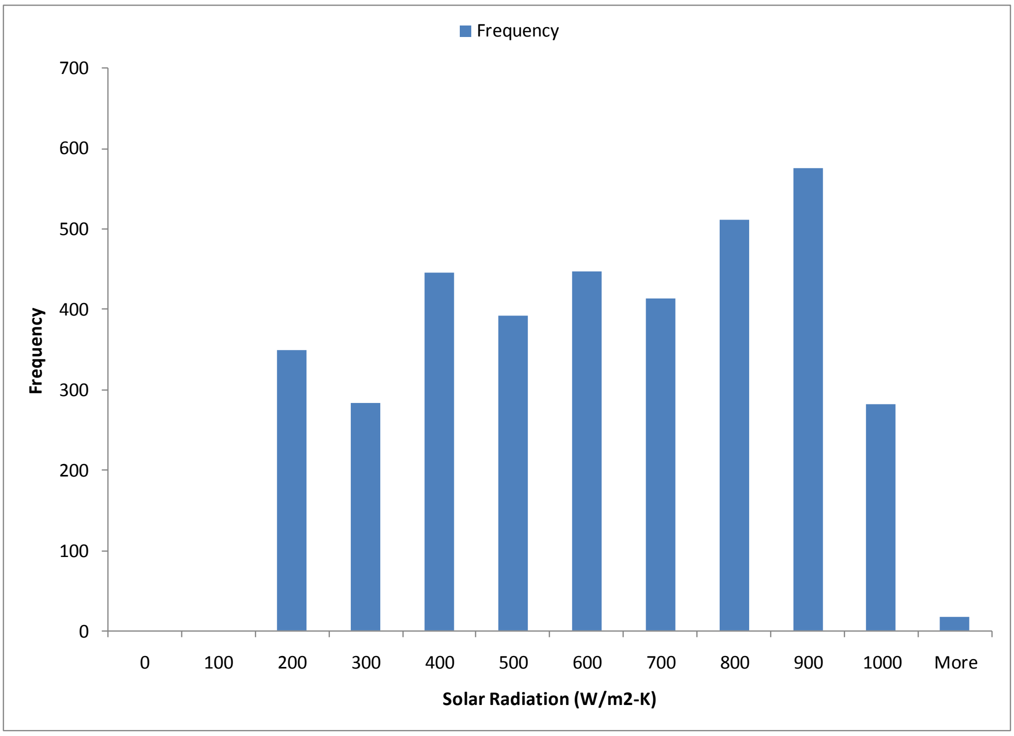

Figure 7. 2: Histogram showing the frequency of occurrence of solar radiation during the year in Abu Dhabi

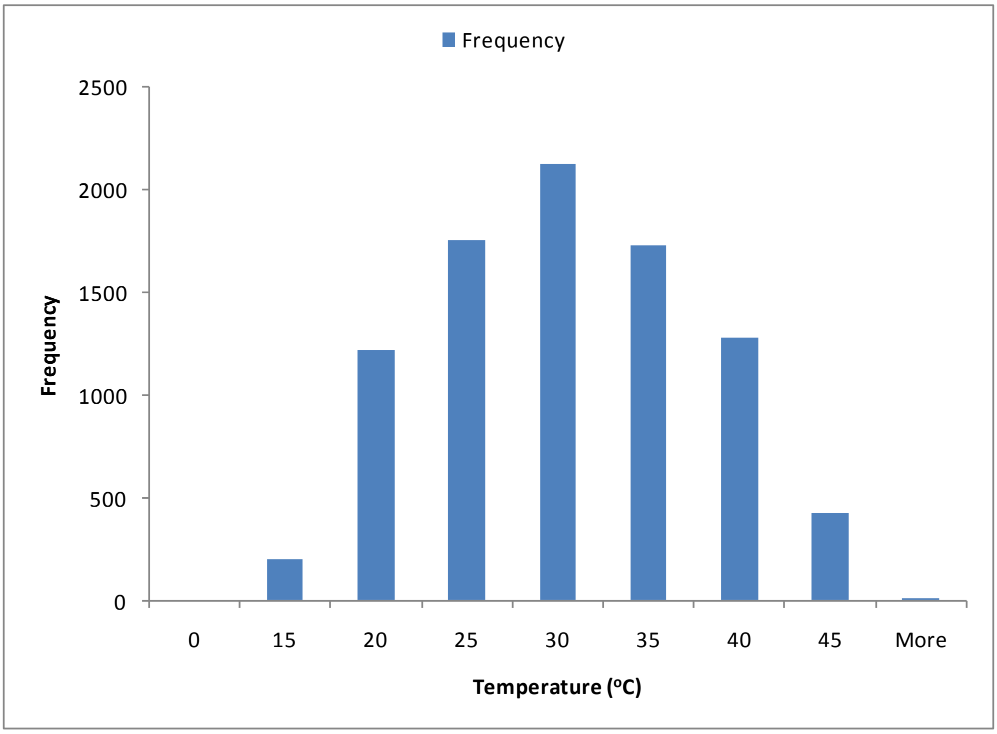

Figure 7. 3: Histogram showing the frequency of occurrence of ambient temperature during the year in Abu Dhabi

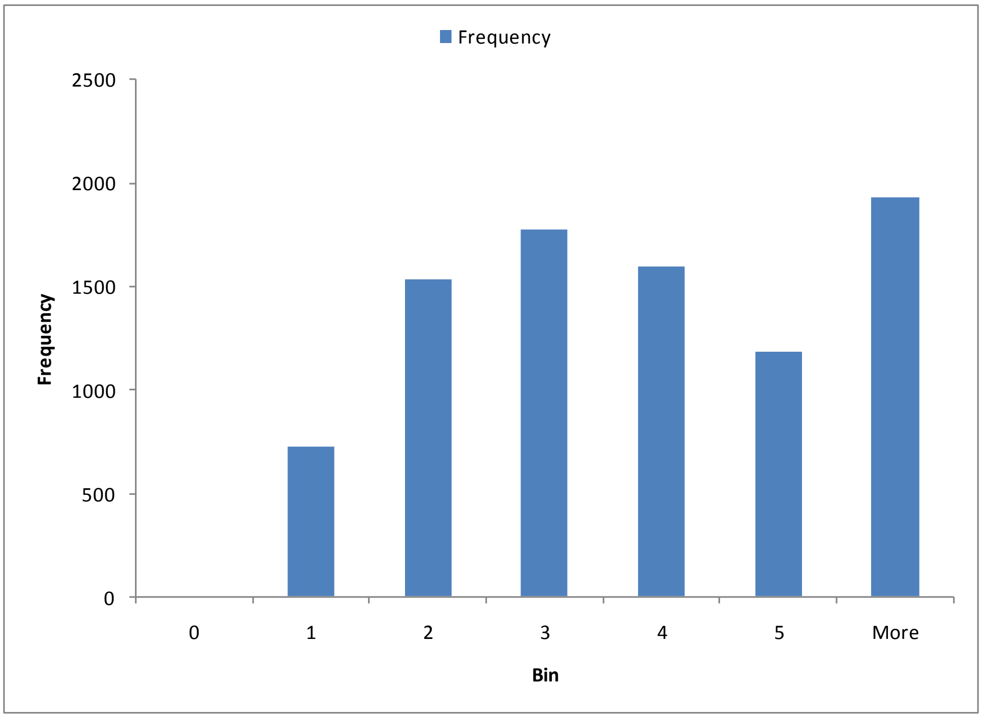

Figure 7. 4: Histogram showing the frequency of occurrence of wind speed during the year in Abu Dhabi

The solar radiation used here is for that incident on a tilted surface with slope=24.43°. It can be seen from Figure 7. 2 that the highest number of occurrences of solar radiation takes place between 800-900W/m^2. Thus the typical solar radiation incident on a collector with slope 24.43° is taken to be 850W/m^2.

Similarly the wind speed occurrence is mostly seen between 3-5m/s. Thus the typical wind speed is taken to be 4m/s. The humidity varies between 0.01-0.035kg$_w$/kg$_{da}$. The maximum occurrence of humidity is at 0.02kg$_w$/k$_{da}$ which is taken as the typical humidity. Lastly the ambient temperature lies between less than 15°C to greater than 45°C and the greatest occurrence of ambient temperature is between 25-30°C. Therefore the typical temperature is taken to be 27.5°C.

This typical Abu Dhabi weather condition is fed in to the LATSC and LDR combined system code. The objective of the optimization is to regenerate the liquid desiccant to a concentration of 0.4 while maximizing the desiccant flow rate. Thus an objective function was defined as:

$$f(objective) = \frac{abs(C_{do}-0.4)}{\dot{m}_{di}} + \frac{1}{\dot{m}_{di}*1000} \qquad (77)$$

The system was optimized by minimizing this objective function. The numerator in the first term is the absolute difference between the outlet desiccant concentration and the desired outlet desiccant concentration. Minimization of this term is vital since the desiccant outlet concentration is required to be 0.4. Thus this term is divided by mdi, which is in the order of 10^{-4}. This ensures that the optimization solver brings the outlet desiccant concentration as close to zero as possible. The second term has the desiccant flow rate in the denominator to ensure that as the desiccant outlet concentration reaches 0.4, the optimizer focuses on maximizing the desiccant flow rate.

The genetic algorithm (GA) in MATLAB was used to optimize the system. The algorithm was provided with the bounds between which the solution was predicted to lie. The GA is useful in finding a global optimum solution. Based on the population specified initially, it selects a pool of random input variables (1st generation) within the bounds specified and solves the LATSC-LDR system to evaluate the objective function. Based on the values of the objective function, the algorithm throws away trial points from the first generation which resulted in large values of the objective function and generates another generation of variables to test as input variables. It repeats this process so that the successive generations converge towards a minimization of the objective function and thus an optimal solution. The flowchart for the working method of the GA is shown in Figure 7. 5.

Results

The optimized air thermal capacitance, water thermal capacitance and desiccant flow rate per unit width of regenerator for a typical Abu Dhabi day is given in Table 7.2:

Table 7.2: Optimized Inlet Conditions per unit collector area

Inlet Condition	Value
Thermal capacitance of water	38.655 W/m^2-K
Thermal capacitance of air	10.979 W/m^2-K
Desiccant mass flow rate per unit regenerator area	0.0003329 kg/s-m
Desiccant mass flow rate per unit collector area	0.00016645 kg/s-m^2

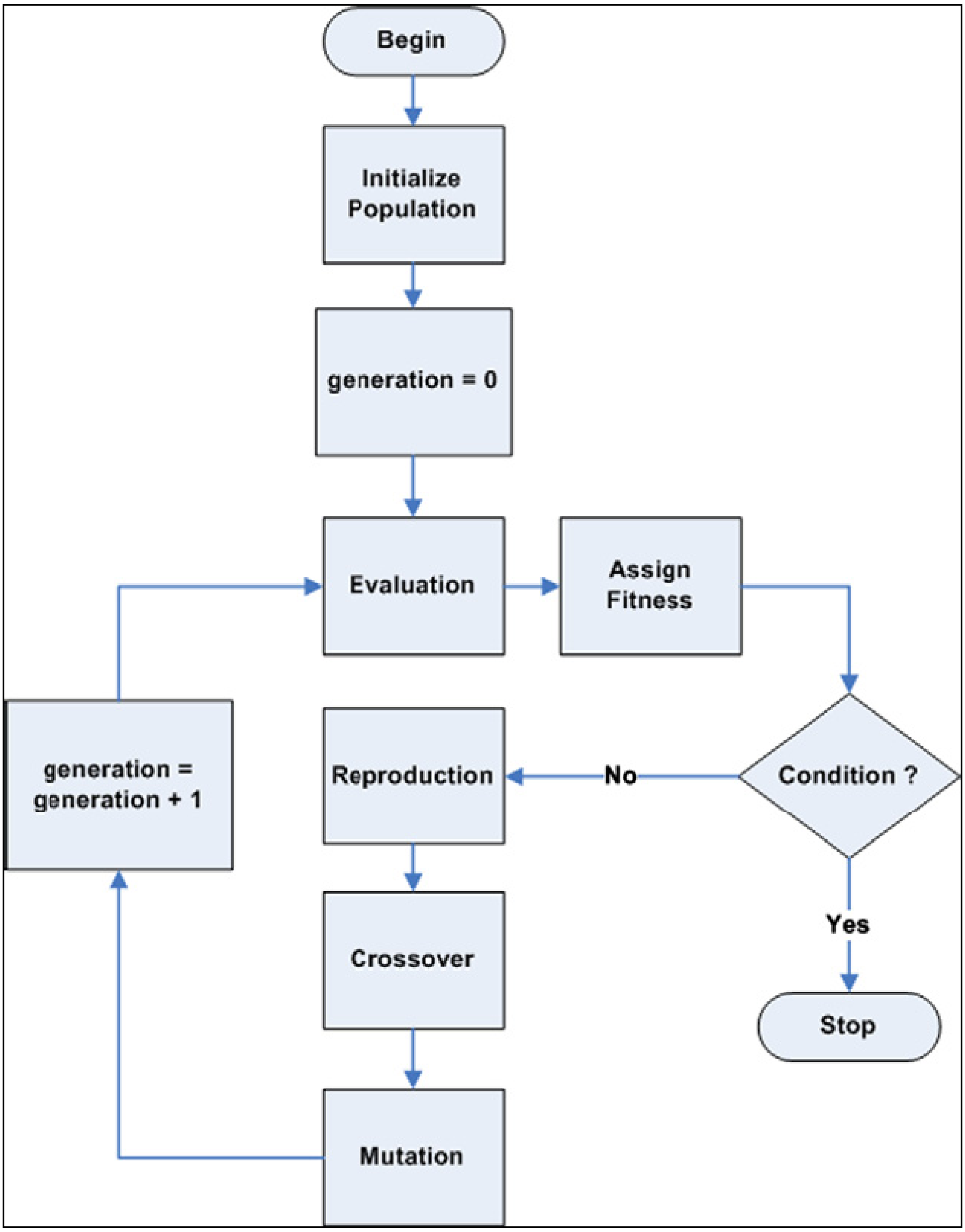

Figure 7. 5: Flowchart showing the working principle of the GA

CHAPTER 8

8 Conclusion

A numerical model of a novel hybrid liquid-air collector has been developed and the outlet water and air temperatures are evaluated by solving a system of ODEs. Two versions of the model are run: one with fully coupled heat transfer to the air behind the collector plate and the other with no heat transfer to the air behind the collector plate. Although the exact heat transfer situation behind the plate depends on plate perforation details, collector performance will always fall between the fully-coupled and uncoupled cases. The latter is shown to reduce to the Hottel-Whillier equation (Appendix A).

Key parameters of the model have been varied to assess the impact on the performance of the collector. Increasing the $(\dot{m}c_p)_{total}$ increases the efficiency of the collector for all values of $R_{\dot{m}cp}$. Moreover, an increase of the $R_{\dot{m}cp}$ from 0.1 to about 0.5 at a constant $(\dot{m}c_p)_{total}$ has been shown to increase the efficiency of the collector while further increase in $R_{\dot{m}cp}$ has led to a decrease in the efficiency because of higher plate temperatures near the outlet ends of the tubes. Furthermore, although an increase of $(T_i-T_{amb})/G$ always decreases the efficiency of the collector the rate of decrease of the efficiency decreases with an increase in $R_{\dot{m}cp}$.

For a low $R_{\dot{m}cp}$ of 0.1, the efficiency of the collector exhibits considerable sensitivity to wind speed, showing that the convective losses are only marginally suppressed at low air flow rates. To heat the cooling water preferentially while still providing enough airflow to suppress convective front losses, it is desirable to conduct the air through the plate and into the airstream behind the plate in such a way that convective coupling is minimized.

Standard performance curves have been generated for ASHRAE 93 standard water flow rate through the collector at the optimum air suction rate. The performance of the LATSC under light wind is observed to be better than a single glazed flat plate collector for water heating. The slope of the performance curves tends to get steeper as wind speed is increased.

A numerical model of a liquid desiccant regenerator(LDR) was developed to test the LATSC with one of its promising applications. Sensitivity analysis was performed on the combined LDR and LATSC model by varying the total thermal capacitance of air and water and the air thermal capacitance ratio. As the $\dot{m}_{tot}$ is increased, the $R_{\dot{m}\mathrm{cp}}$ for the optimum performance of the system decreases. The optimum performance of the system increases as $\dot{m}_{tot}$ is increased. Moreover the regenerator performs better with higher flow rates of water as long as the critical convection suppression is achieved by the air suction.

A prototype of the LATSC was built and experimentally tested at a total thermal capacitance rate of 50w/m^2-k with $R_{\dot{m}\mathrm{cp}}$ ratios from 0.1-0.5. The results show a considerable deviation from the predicted collector model. Multiple reasons have been explained for this discrepancy. The greatest effect is believed to be due to the large starting length compared to the width of the collector and the consequent invalidity of the heat exchange effectiveness of the air heating at the front and in the holes of the absorber plate. A larger collector and better workmanship of the absorber plate is proposed in order to obtain conclusive results in future testing.

The numerical model results provide a promising outlook for the LATSC for liquid desiccant regeneration, domestic water and ventilation heating and low temperature desalination applications. The experimental validation of the model is inconclusive due to the size limitations of the collector. A larger collector size of at least $5m^2$ is suggested for further experimental work on the verification of the numerical model.

Lastly the combined model of the LATSC and a falling film, parallel plate type liquid desiccant regenerator was optimized for a typical Abu Dhabi day. The results show that the optimized inlet air thermal capacitance rate, water thermal capacitance rate and desiccant mass flow rate per unit collector area are 25.89275 W/m^2-K, 61.5425 W/m^2-K and 0.00013771 kg/s-m respectively.

8.1 Further Work

As discussed previously, the collector testing results do not match closely with the numerical model, partly due to inconsistencies in the experimental setup with the assumptions made while developing the numerical model. There are two ways to reduce the difference between the numerical model and experimental model. Firstly the experimental setup needs to be modified considerably so that the assumptions made in the model are valid, after which retesting will be required before any decisive conclusion can be made on the validity of the model. The modifications required in the experimental setup are:

1) Replace the present collector with a collector having an area of at least 5m^2, depending on the suction flow rates and wind speeds to be tested with.
2) Ensure that the new collector has a smooth flat plate and the front of the plate is uniformly painted with a durable black paint with a known absorptivity and emissivity over the solar spectrum.
3) The flat plate should be perforated uniformly (i.e. with no extra gap at the location of the tubes on the plate).
4) Minimize the leakiness of the collector shell.

The second way to reduce the difference between the numerical model and the experimental setup is by modifying the numerical model to account for the heat transfer to the suction air in the starting length of the thermal boundary layer. Moreover the wind loss coefficient depends on the length of the plate in the direction of the wind, and as the collector length is twice the collector width, the direction of the wind will have a significant impact on the wind loss coefficient. Thus a 2-D wind loss model will need to be incorporated in the numerical model.

A combination of both experimental and numerical modifications will have to be applied in order to obtain accurate and repeatable results. The testing procedure can also be performed indoors using a solar simulator to model the sun and a fan to ensure a constant wind speed so that steady state results may be obtained. A wind tunnel test with a heated plate and no solar simulator could alternatively be used to characterize and validate the collector losses.

Furthermore, the LATSC-LDR combined system will have to be compared to the performance of a FPC-LDR system with a air to water heat exchanger to critically assess the advantages of the proposed LATSC.

Next, a LDR will have to be built to test the coupled performance of the collector and regenerator system. Finally a humidification-dehumidification (HDH) desalination system can also be modeled and tested with minor modifications to the LDR model using brine instead of lithium chloride as the regeneration liquid.

APPENDIX A

Linearized Hottel-Whillier Model for LATSC

We observed that the LATSC model with heat transfer to the air behind the absorber plate (coupled case) gives performance not much different from that given by the model with no heat transfer behind the absorber plate (uncoupled case). This observation suggests a simplified model based on the Hottel-Whillier (H-W) equation (Duffie & Beckman, 1980) in which heating of the water is given by:

$$Q_u = A\left(F_R G - U_l\left(T_{fi} - T_{amb}\right)\right) \tag{78}$$

where:

$$F_R = \frac{\dot{m}_w c_{pw}}{A_c U_l F'}\left(1 - \exp\left(-\frac{A_c U_l F'}{\dot{m}_w c_{pw}}\right)\right) \tag{79}$$

F_R is the heat removal factor defined as the ratio of the rate of water heating to the heat rate that would occur if the plate temperature was equal to the fluid inlet temperature.

The H-W formulation requires a constant radiation heat transfer coefficient (h_r) with the sky temperature, T_{sky}, assumed to be equal to ambient temperature T_{amb}. Therefore equations 12 and 13 are changed to:

$$q_{rad,loss} = \epsilon\sigma 4{T_m}^3(T_{pl} - T_{amb}) \tag{80}$$

where

$$T_m = (T_{pl} + T_{amb})/2 \tag{81}$$

The radiation heat transfer coefficient of the plate can then be expressed as:

$$h_r = \epsilon\sigma 4{T_m}^3 \tag{82}$$

While the convective heat transfer coefficients due to wind and suction through the plate can be expressed as:

$$h_{wind} = 0.82\,\frac{V_w \nu_a \rho_a c_{pa}}{V_s L} \tag{83}$$

$$h_{c,air} = \dot{m}_a c_{pa} e_{hx} \tag{84}$$

The total heat loss coefficient from the plate is the sum of the three transfer coefficients for top loss and the back and edge loss coefficients:

$$U_l = h_r + h_{wind} + h_{c,air} + U_{b,tot} + U_e \tag{85}$$

where

$$U_{b,tot} = \frac{q_{back,loss}}{(T_{pl} - T_{amb})} \tag{86}$$

the air heating, which is not part of Q_u, is given by:

$$Q_{c,air} = \dot{m}_a c_{pa} \varepsilon_{hx} (T_{pm} - T_{amb}) \tag{87}$$

where

$$T_{pm} = T_{fi} + \frac{Q_u}{A_c F_R U_l}(1 - F_R) \tag{88}$$

The H-W model and the uncoupled form of the numerical model were simulated using identical inlet and ambient conditions and the linearized loss coefficients based on mean plate temperature (37-39). The results showed that both the air and water outlet temperatures match within the precision of MATLAB’s numerical integrator ODE45.

Given reasonable initial estimates of h_r, h_{wind} and $h_{suction}$, one can expect to obtain an accurate estimate of T_{pl} and overall collector performance in two iterations.

APPENDIX B

Orifice Plate Calibration with Wind Tunnel

The TSI Wind Tunnel was used to calibrate the orifice plates. In order to perform the calibration, the fan was removed from the wind tunnel and replaced with the fan that was used in the setup, followed by a straight piece of square duct (8.5” x 8.5”). The duct was followed by a reducer which reduced the cross sectional area of the flow to 55mm (PVC pipe diameter). A flow straightner was also manufactured in order to condition the flow and was installed 10 diameters of pipe length preceding the orifice plate/nozzle assembly. Figures B.1-B.4 below show the assembly of the Wind Tunnel with the flange assembly holding the orifice plates/nozzles.

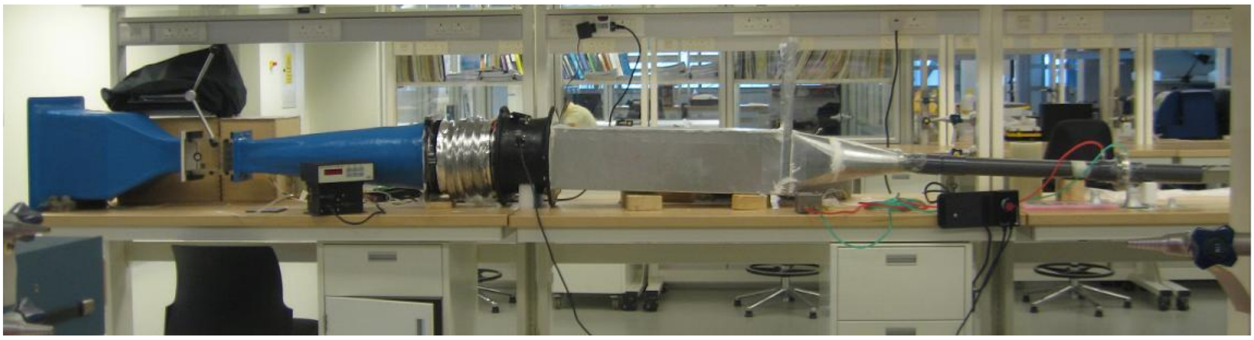

Figure B. 1: Wind Tunnel test assembly.

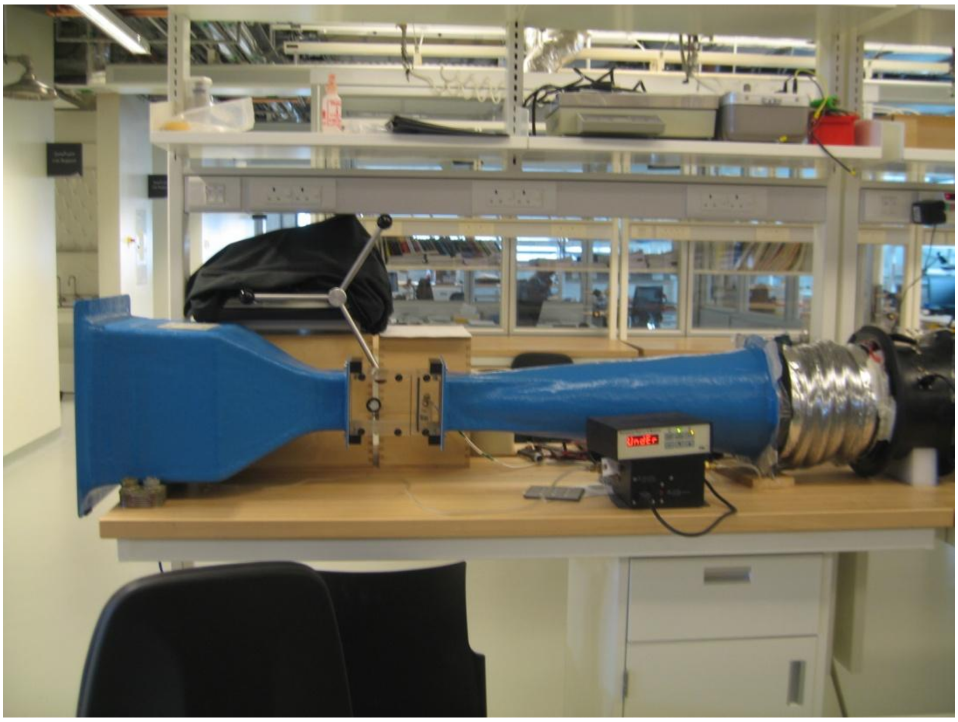

Figure B. 2: Wind Tunnel connected to fan

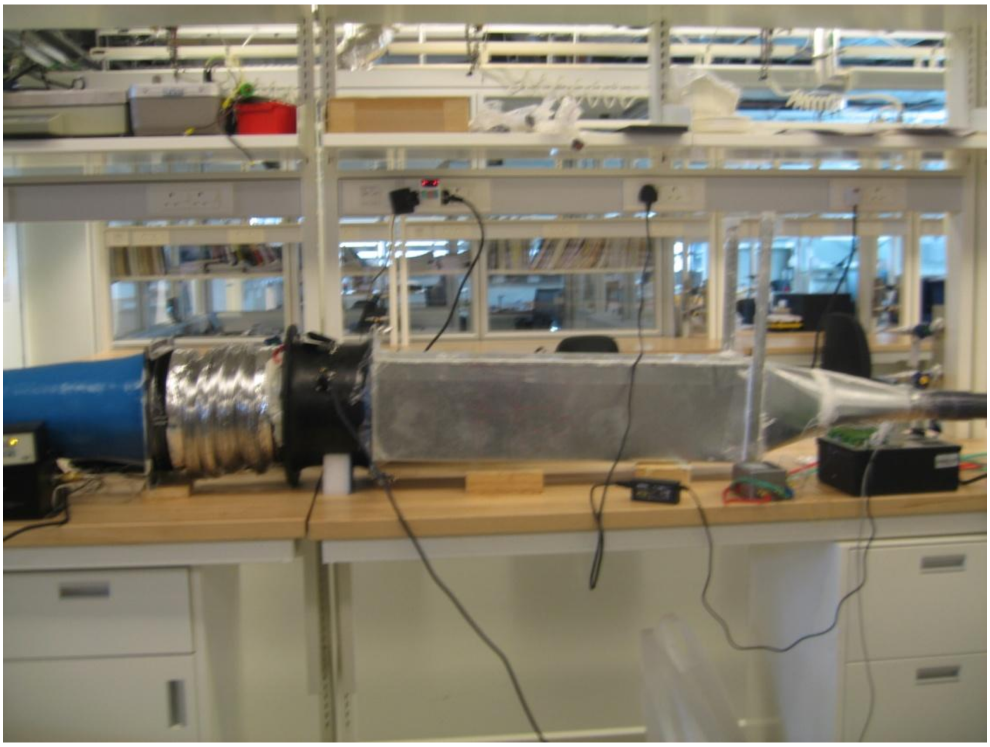

Figure B. 3: Fan connection with duct and reducer

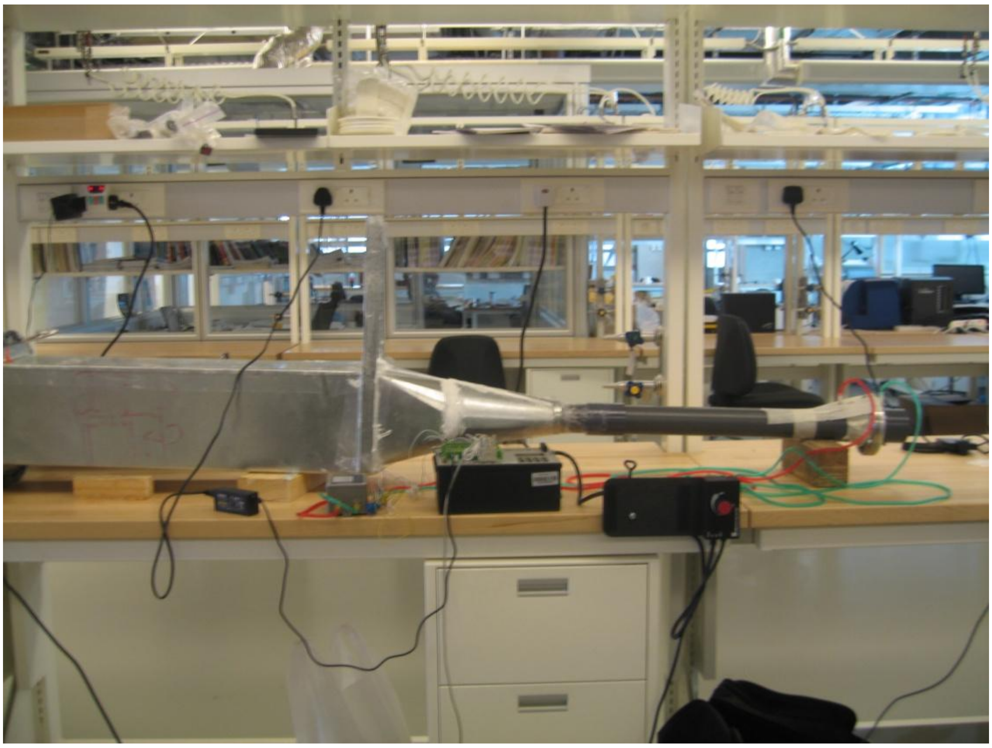

Figure B. 4: Reducer to flange assembly to exit

B.1 Results

The Wind Tunnel allows calibration using 2 nozzle plates. Nozzle plate 1 has nine 0.656” diameter holes while nozzle plate 2 has nine 0.25” diameter holes. The Wind Tunnel has been designed to calibrate velocity probes(e.g. pitot static tubes and thermal anemometers) for velocity measurements however we extended the application to volume flow measurement by using the velocity measurement in the test box and multiplying it by the cross sectional area of the box to obtain the flow rate. This is not exact because the velocity is not perfectly uniform across the cross sectional area. Nevertheless this method allows us to roughly measure the flow rate. The cross sectional area of the wind tunnel test box is 4”x4”. The calibrated velocity ranges and corresponding flow ranges for the nozzle plates are given in Table B. 1 below.

Table B. 1: Velocity and Volumetric Flow rate range of Nozzle Plates.

Nozzle Plate	Velocity (ft/min)	Flow (cfm)
1	250-1500	27.78-166.67
2	30-250	3.33-27.78

The orifice plates were tested for a range of flow rates corresponding to those in Table 1 and the flow rate obtained due to the pressure drop across these devices was compared to the flow rate in the test box. All leaks in the duct connections and pipe work were filled using caulk. The flow readings for the orifice plates were accurate to 4.5% using nozzle plate 2 in the test box with the accuracy increasing with higher flow rates. The percentage difference in flow readings is plotted against the actual flow readings in the test box in Figure B. 5 below.

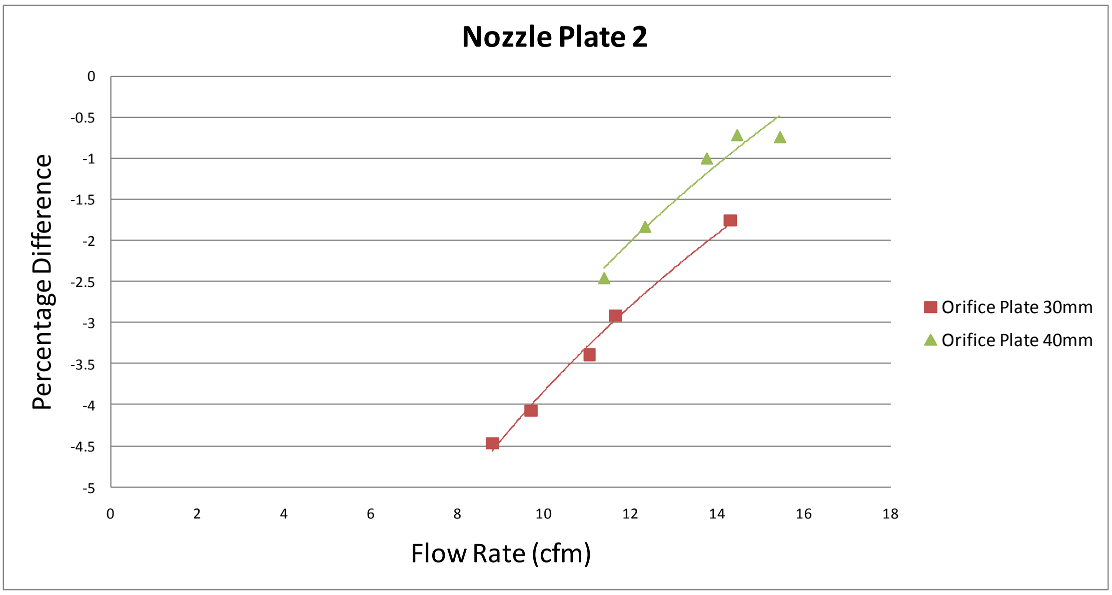

Figure B. 5: Percentage difference in flow readings vs Flow rate (Nozzle Plate 2)

The full range of flow rate up to 27.78 cfm could not be achieved using plate 2 due to the high pressure losses in the assembly and the fan’s inability to provide a higher flow rate with these losses.

APPENDIX C

Water flow meter calibration

The water flow meter was calibrated prior to using it in testing the flat plate collector. The flow range within which the flow meter was tested was 1 -2.5 liters/min. The calibration of the flow meter was performed by running water through an open circuit pipe in which the flow meter was also installed. One end of the pipe was attached to a near constant water supply source(tap), while the other end discharged the water in to a bucket. The bucket lay on top of a mass scale which was used to measure the change in mass of the bucket. The change in mass of the bucket and the discharge water temperature was recorded at equal time intervals[1]. This flow rate was compared to the flow rate measured through the flow meter. The error in the measurement was defined as:

$$error = \frac{\dot{V}_{flow\ meter} - \dot{V}_{measured}}{\dot{V}_{measured}} X 100\% \qquad (89)$$

The error points obtained are shown in Figure C.1 below:

---

[1] In use, the temperature of the water was used to determine the density of the water to calculate the flow rate of the water

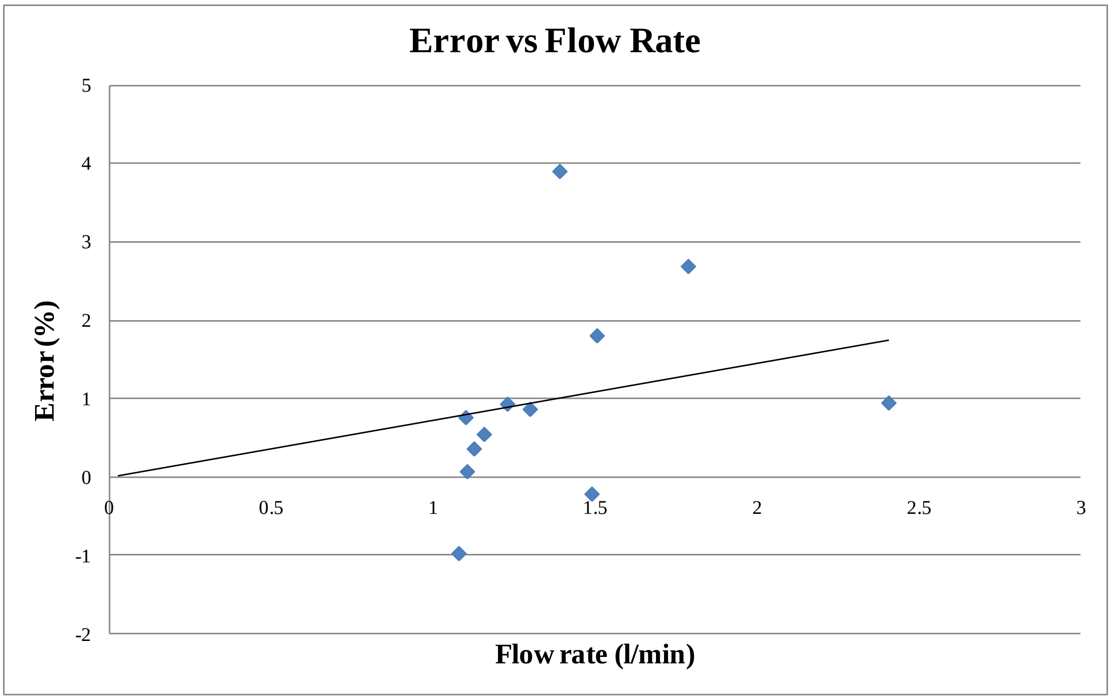

Figure C.1: Deviation of flow meter response from factory constant vs Flow Rate for the water flow meter

APPENDIX D

Collector shell leak test

As the collector was transformed from a single glazed water heating collector to a LATSC, care was needed to ensure that the collector was well sealed. The collector shell was tested for leaks by first covering the absorber plate with a polythene sheet and then using the blower door component testing method to check for leaks in the collector. The collector was pressurized and a smoke stick was used to find leaks in the collector shell and the leaks were patched using silicone caulk. A leak test was then performed by pressurizing the collector and measuring the pressure drop across a small orifice as well as the collector static pressure. The collector static pressure was measured up to 80Pa. The air flow rate through the collector was also measured with the polythene sheet removed at static pressures from 50-80Pa. The leakage rate and leakage percentage was then plotted against the static pressure. The leakage percentage is the percentage ratio of the leakage rate (at a particular fan static pressure) and the flow rate through the collector with the polythene sheet removed (at the same static pressure). Figure D 1**Error! Reference source not found.** below shows the variation of the leakage rate and leakage percentage with static pressure.

The leakage rate at 50Pa static pressure was 0.85cfm while the percentage leakage varied from 2.5-2.62%. The percentage leak rate variation is not statistically significant and can be taken as a constant 2.5%.

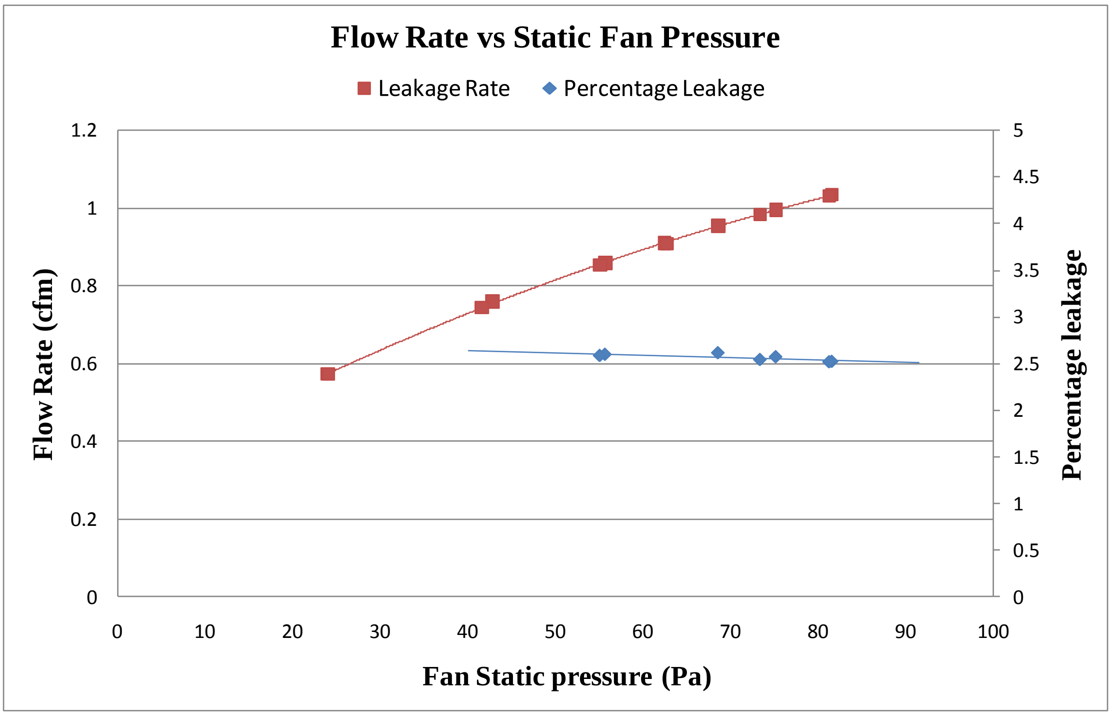

Figure D 1: Leakage Flow Rate and Leakage Percentage vs. Fan Static Pressure

APPENDIX E

Evaluation of $(\tau\alpha)_{avg}$

$$(\tau\alpha)_{avg} = 0.96(\tau\alpha)_b \tag{90}$$

$$(\tau\alpha)_b = 1.01 * \tau * \alpha_n * \alpha/\alpha_n \tag{91}$$

From figure 5.3.1 (Duffie & Beckman, 1980), with KL=0.0125, τ=0.91

$$\alpha_n = 0.93 \tag{92}$$

$$(\tau\alpha)_b = 1.01*0.91*0.93*1=0.85476 \tag{93}$$

$$(\tau\alpha)_{avg} = 0.96 * 0.854763=0.8206 \tag{94}$$

For a typical flat plate collector, the equation on the graph in Figure() should be of the form:

$$\eta = F_R(\tau\alpha)_{avg} - \frac{F_R U_l(T_i - T_a)}{G_T} \tag{95}$$

Thus:

$$F_R(\tau\alpha)_{avg}=0.6491 \tag{96}$$

$$F_R=0.6491/0.8206=\underline{0.791} \tag{97}$$

and $$F_R*U_l=7.126 \tag{98}$$

$$U_l=7.126/0.791=\underline{9.009\ W/m^2K} \tag{99}$$

APPENDIX F

Nomenclature

A_c	Collector area (m^2)
C_a	Concentration of water in air (kg_w/kg_a)
C_b	Bond conductance(W/m-K)
C_d	Concentration of water in desiccant (kg_w/kg_d)
C_{int}	Equilibrium concentration of water at air-desiccant interface (kg_w/kg_d)
c_{pa}	Specific heat of air (kJ/kgK)
c_{pw}	Specific heat of water (kJ/kgK)
D_a	Mass diffusivity (m^2/s)
D_h	Hole diameter (m)
D_p	Hydraulic diameter of plenum (m)
D_t	Tube outer diameter (m)
F	Fin efficiency
F’	Collector efficiency factor
F_R	Collector heat removal factor for water
G	Absorbed solar radiation (W/m^2)
h	Hours from midnight (hours)
h_a	Air heat transfer coefficient (W/m^2K)
h_{fi}	Heat transfer coefficient inside tubes (W/m^2K)

h_{fg}	Latent heat of vaporization of water(kJ/kg)
h_m	Mass transfer coefficient of water vapor (kg/m^{2}s)
h_w	Water heat transfer coefficient (W/m^{2}K)
k	Thermal conductivity (W/mK)
L	Length of collector (m)
L_c	Characteristic length of collector (m)
L_s	Starting length of boundary layer from leading edge (m)
$(\dot{m}c_p)_{total}$	Total thermal capacitance rate of air and water
$\dot{m}$	Mass flow rate (kg/s)
$R_{\dot{m}cp}$	Ratio of $\dot{m}c_{p_{air}}$ to $\dot{m}c_{p_{total}}$
N	Number of tubes
Nu	Nusselt number
NTU	Number of transfer units
P	Perimeter of plenum cross section (m)
Pitch	Spacing of holes on absorber plate (m)
por	Plate porosity
Pr	Prandtl Number
q_{back}	Convection to air at back wall of plenum per unit area(W/m^2)
$q_{back,loss}$	Back convection loss per unit area(W/m^2)
$q_{conv,loss}$	Front convection loss per unit area(W/m^2)
q_{edge}	Edge Loss per unit area of the collector(W/m^2)
$q_{rad,loss}$	Front radiation loss per unit area (W/m^2)
$q_{c,air}$	Heat transferred to suction air per unit area (W/m^2)
Q_u	Useful energy transferred to water (W)
Re	Reynolds Number
s	Distance between tubes in absorber
t	Thickness (m)

$T_a(y)$	Air temperature at distance y from inlet (^oC)
T_{amb}	Ambient temperature (^oC)
T_{fi}	Water inlet temperature (^oC)
$T_m(y)$	Mean of plate and sky temperature (^oC)
$T_{pl}(y)$	Plate temperature (^oC)
T_{sky}	Sky Temperature (^oC)
$T_w(y)$	Water Temperature (^oC)
U	Heat transfer coefficient (W/m^2K)
V_s	Suction face velocity (m/s)
V_w	Wind Speed (m/s)
V_{wa}	Water velocity in tubes (m/s)
W	Width of collector (m)
x	lateral distance from tube(m)
y	distance from inlet end of collector(m)

Greek letters:

ε_{hx}	Heat exchange effectiveness of perforated plate
δ	Plate thickness (m)
ϵ	Emissivity of collector plate
ρ	Density (kg/m^3)
ν	Kinematic viscosity (m^2/s)
σ	Stephan-Boltzmann constant ($W/m^2\text{-}K^4$)
ω	Humidity ratio of air (kg_w/kg_{da})

Subscripts:

a	air
ab	back of absorber plate
bi	back insulation
bp	back plate
br	back of absorber plate radiation
c	collector
d	desiccant
da	dry air
ds	desiccant salt
e	edge of plate
exp	experimental
exit	exit from the perforations
h	pertaining to air flowing through perforations
i	inlet
o	outlet
p	plate
reg	regenerator
t	tubes
th,n	theoretical, with incident radiation normal to absorber plate
tot	air +water combined mass or heat rat
w	water
wb	pertaining to wind at back of collector
wd	water in desiccant
wf	pertaining to wind at front of collector
wv	water vapor

Bibliography

Al-Enezi, G., Ettouney, H., & Fawzy, N. (2006). Low temperature humidification dehumidification desalination process. *Energy Conversion and Management, 47*(4), 470-484.

Ali, A., Vafai, K., & Khaled, A.-R. A. (2003). Comparative study between parallel and counter flow configurations between air and falling film desiccant in the presence of nanoparticle suspensions. *International Journal of Energy Research, 27*, 725-745.

Ali, M. T., Mokhtar, M., Armstrong, P. R., & Cheisa, M. (2011). A Cooling Change-Point Model of Community-Aggregate Electrical Load. *Energy and Buildings, 43*, 28-37.

Arulanandam, S. J., Hollands, K. G. T., & Brundrett, E. (1999). A CFD heat transfer analysis of the transpired solar collector under no-wind conditions. *Solar Energy, 67*(1-3), 93-100.

The Basics of Solar Energy Installations. (2010). Retrieved 30/03/2011

Belusko, M., Saman, W., & Bruno, F. (2008). Performance of jet impingement in unglazed air collectors. *Solar Energy, 82*, 389-398.

Biona, M., Culaba, A., Serafica, E., & Mundo, R. d. (2005). *Performance curve generation of an unglazed transpired collector for solar drying applications*. Paper presented at the World Renewable Energy Regional Conference 2005, Jakarta Indonesia

Bliss, R. W. (1960). The derivation of several "plate efficiency factors" useful in design of flat-plate solar collectors. *Solar Energy, 3*, 55-64.

Burch, J., Christensen, C., Merrigan, T., Hewett, R., & Jorgensen, G. (2005). *Low-cost solar domestic hot water systems for mild climates*. Paper presented at the DOE Solar Energy Technologies Program Review Meeting, Denver, Colorado.

Burch, J., Salasovich, J., & Hillman, T. (2005). *An assessment of unglazed solar domestic water heaters*. Paper presented at the ISES Solar World Congress, Orlando, Florida.

Christensen, C. (1998). *Transpired Collectors (Solar Preheaters for Outdoor Ventilation Air)*.

Conde, M. R. (2004). Properties of aqueous solutions of lithium and calcium chlorides: formulations for use in air conditioning equipment design. *International Journal of Thermal Sciences, 43*(4), 367-382.

Dieckmann, J., Roth, K., & Brodrick, J. (2008). Liquid Desiccant Air Conditioners. *ASHRAE Journal, October 2008*, 90-95.

Duffie, J., & Beckman, W. (1980). *Solar Engineering of Thermal Processes*: John Wiley & Sons Inc.

Dymond, C., & Kutscher, C. (1997). Development of a flow distribution and design model for transpired solar collectors. *Solar Energy, 60*(5), 291-300.

Factor, H. M., & Grossman, G. (1980). A packed bed dehumidifier/regenerator for solar air conditioning with liquid desiccants. *Solar Energy, 24*(6), 541-550.

Fath, H. E. S., & Ghazy, A. (2002). Solar desalination using humidification--dehumidification technology. *Desalination, 142*(2), 119-133.

Gandhidasan, P. (2004). A simplified model for air dehumidification with liquid desiccant. *Solar Energy, 76*(4), 409-416.

Gandhidasan, P. (2005). Quick performance prediction of liquid desiccant regeneration in a packed bed. *Solar Energy, 79*(1), 47-55.

Gawlik, K. M. (1995). *A Numerical and Experimental Investigation of Heat Transfer Issues in Practical Utilization of Unglazed Transpired Solar Collectors.* PhD Thesis, University of Colorado, Boulder.

Gawlik, K. M., & Kutscher, C. F. (2002). Wind Heat Loss From Corrugated, Transpired Solar Collectors. *Journal of Solar Energy Engineering, 124*(3), 256-261.

Gunnewiek, L. H., Brundrett, E., & Hollands, K. G. T. (1996). Flow distribution in unglazed transpired plate solar air heaters of large area. *Solar Energy, 58*(4-6), 227-237.

Hottel, H., & Whillier, A. (1955). Evaluation of flat-plate solar collector performance. *Trans. Conf. Use of Solar Energy, 3(Thermal Processes)*(2).

Hottel, H., & Woertz, B. (1942). Performance of flat-plate solar-heat collectors. *Journal Name: Trans. ASME (Am. Soc. Mech. Eng.); (United States); Journal Volume: 64*, Medium: X; Size: Pages: 91.

Hueffed, A. K., Chamra, L. M., & Mago, P. J. (2009). A Simplified Model of Heat and Mass Transfer Between Air and Falling-Film Desiccant in a Parallel-Plate Dehumidifier. *Journal of Heat Transfer, 131*(5), 052001-052007.

Hyland, & Wexler. (1983). Formulations for the thermodynamic properties of the saturated phases of H2O from 173.15 K to 473.15 K. *ASHRAE Transactions, Part 2A*(Paper 2793 (RP-216)).

Incropera, Witt, D., Bergman, & Lavine. (2006). *Fundamentals of Heat and Mass Transfer*: Wiley.

Jain, S., & Bansal, P. K. (2007). Performance analysis of liquid desiccant dehumidification systems. *International Journal of Refrigeration, 30*, 861-872.

Jain, S., Dhara, P. L., & Kaushi, S. C. (2000). Experimental studies on the dehumidifier and regenerator of a liquid desiccant cooling system. *Applied Thermal Engineering, 20*, 253-267.

Jones, B. M., & Harrison, S. J. (2008). *First results of a solar-thermal liquid desiccant air conditioning concept*. Paper presented at the EUROSUN 2008

Kabeel, A. E. (2007). Solar powered air conditioning system using rotary honeycomb desiccant wheel. *Renewable Energy, 32*, 1842-1857.

. *Key Issues for Renewable Heat in Europe (K4RES-H)*. (2006).

Kinsara, A. A., Elsayedt, M. M., & Al-Rabghi, O. M. (1996). Proposed energy-efficient air-conditioning system using liquid desiccant. *Applied Thermal Engineering, 16*(10), 791-806.

Klein, S. A. (1975). Calculation of flat-plate loss coefficients. *Solar Energy, 17*.

Klein, S. A. (2010). Engineering Equation Solver (Version 8.736): University of Wisconsin-Madison.

Koehl, M. (2001). Durability of solar energy materials. *Renewable Energy 24* (1), 597–607.

Kutscher, C. F. (1992). *An Investigation of Heat transfer for air flow through low porosity perforated plates.* PhD Thesis, University of Colorado Boulder.

Kutscher, C. F. (1994). Heat exchange effectiveness and pressure drop for air flow through perforated plates with and without crosswind. *Journal of Heat Transfer, 116*(2), 391-399.

Kutscher, C. F., Christensen, C. B., & Barker, G. M. (1993). Unglazed transpired solar collectors: heat loss theory. *Journal of Solar Energy Engineering, 115*(3), 182-188.

Leon, M. A., & Kumar, S. (2007). Mathematical modeling and thermal performance analysis of unglazed transpired solar collectors. *Solar Energy, 81*, 62-75.

Lowenstein, A., Slayzak, S., & Kozubal, E. (2006). A zero carryover liquid-desiccant air conditioner for solar applications. *ASME Conference Proceedings, 2006*(47454), 397-407.

Maurer, C. C. (2004). *Field Study And Modeling Of An Unglazed Transpired Solar Collector System.* MS Thesis, North Carolina State University, Raleigh.

Mei, L., & Dai, Y. J. (2008). A technical review on use of liquid-desiccant dehumidification for air-conditioning application. *Renewable and Sustainable Energy Reviews, 12*, 662-689.

Mokhtar, M., Ali, M. T., Bräuniger, S., Afshari, A., Sgouridis, S., Armstrong , P., et al. (2010). Systematic comprehensive techno-economic assessment of solar cooling technologies using location-specific climate data. *Applied Energy*.

Narayan, G. P., Sharqawy, M. H., Summers, E. K., Lienhard, J. H., Zubair, S. M., & Antar, M. A. (2010). The potential of solar-driven humidification-dehumidification desalination for small-scale decentralized water production. *Renewable and Sustainable Energy Reviews, 14*(4), 1187-1201.

Norton, B. (2006). Anatomy of a solar collector. *reFOCUS, May/June 2006,* 32-35.

Pesaran, A. A., & Wipke, K. (1992). *Desiccant Cooling Using Unglazed Transpired Solar Collectors*. Paper presented at the ASES 1992, Cocoa Beach, Florida.

Remund, J., Lang, R., & Kunz, S. (2003). METEONORM (Version 5.1). Bern, Switzerland: Meteotest

Summers, D. N. (1995). *Thermal Simulation and Economic Assessment of Unglazed Transpired Collector Systems.* MS Thesis, University of Wisconsin-Madison, Madison.

Thoruwaa, T. F. N., Johnstoneb, C. M., Grantb, A. D., & Smith, J. E. (2000). Novel, low cost CaCl2 based desiccants for solar crop drying applications. *Renewable Energy, 19*, 513-520.

Van-Decker, G. W. E., Hollands, K. G. T., & Brunger, A. P. (2001). Heat-exchange relations for unglazed transpired solar collectors with circular holes on a square or triangular pitch. *Solar Energy, 71*(1), 33-45.

W. Kessling, Laevemann, E., & Kapfhammer, C. (1998). Energy Storage For Desiccant Cooling Systems Component Development. *Solar Energy, 64*(4-6), 209-221.

Wurtz, E., Maalouf, C., Mora, L., & Allard, F. (2005). *Parametric analysis of a solar dessicant cooling system usingthe simspark environment*. Paper presented at the Ninth International IBPSA Conference.

Xiong, Z. Q., Dai, Y. J., & Wang, R. Z. (2009). Investigation on a two-stage solar liquid-desiccant (LiBr) dehumidification system assisted by CaCl2 solution. *Applied Thermal Engineering, 29*, 1209-1215.

Yin, Y., & Zhang, X. (2010). Comparative study on internally heated and adiabatic regenerators in liquid desiccant air conditioning system. *Building and Environment, 45*(8), 1799-1807.

Yin, Y., Zhang, X., & Chen, Z. (2007). Experimental study on dehumidifier and regenerator of liquid desiccant cooling air conditioning system. *Building and Environment, 42*, 2505-2511.